Efficient entanglement distillation based on emulation

Von der Fakultät für Mathematik und Physik
der Gottfried Wilhelm Leibniz Universität Hannover

zur Erlangung des Grades

„Doktorin der Naturwissenschaften"
(Dr. rer. nat.)

genehmigte Dissertation

von

M.Sc. Daniela Abdelkhalek

2017

Referent: Prof. Dr. Roman Schnabel
                      Universität Hamburg
Korreferent: Prof. Dr. Karsten Danzmann
                      Leibniz Universität Hannover
Tag der Promotion: 28.08.2017

Abstract

Many important quantum information protocols such as quantum key distribution require the distribution of entangled states of light over large distances. Unavoidable effects like optical loss or phase noise, however, reduce or even destroy the entanglement during the transmission of the light modes. To restore parts of the entanglement, iterative distillation protocols are proposed. Unfortunately, these protocols are inefficient in terms of success probability and experimental resources. Appropriate quantum memories could in principle overcome these inefficiencies, but have not been experimentally realized yet.

Emulated entanglement distillation, proposed by Jaromír Fiurášek and Nicolas Cerf, provides a novel attempt to make iterative distillation protocols feasible. The main idea is to shift the entanglement distillation protocol to the postprocessing of the data obtained via an appropriate measurement of the distributed states. This emulation of the distillation protocol significantly increases the success probability and, at the same time, facilitates a compact experimental setup.

The main part of this thesis is dedicated to the experimental demonstration of emulated entanglement distillation of non-Gaussian states that got degaussified, e.g. during the transmission over a noisy channel. To simulate such noisy transmission of entangled states, a two-mode-squeezed state was prepared and then intentionally degaussified under the presence of phase noise. The distillation is performed with eight-port homodyne measurements and subsequent postprocessing of the acquired data. With this setup we are able to realize, for the first time, the full iterative distillation protocol for up to three iteration steps. The data show for each iteration step a significant improvement of entanglement, purity and Gaussianity.

In the second part of this thesis, we discuss modifications to the experimental implementation essential for emulated distillation of Gaussian states and successfully realize them in a test setup. Most importantly, we implement on the one hand stabilization techniques for squeezed-light sources and eight-port homodyne detectors without any bright light field that co-propagates with the signal field. On the other hand, we realize eight-port homodyne detection of the squeezed states over a large frequency range of up to 100 MHz with a flat spectrum.

Keywords: Entanglement distillation, emulation, eight-port homodyne detection

Kurzfassung

Viele wichtige Quanteninformations-Protokolle wie z.B. Quantenschlüsselverteilung benötigen die Verteilung von verschränkten Licht-Zuständen über große Entfernungen. Unvermeidliche Effekte wie optische Verluste oder Phasenrauschen reduzieren die Verschränkung bei der Transmission der Lichtmoden oder zerstören die Verschränkung sogar komplett. Iterative Distillationsprotokolle wurden vorgeschlagen, um Teile der Verschränkung wiederherzustellen. Diese Protokolle sind jedoch ineffizient hinsichtlich ihrer Erfolgswahrscheinlichkeit und der benötigten experimentellen Resourcen. Spezielle Quantenspeicher wären in der Lage diese Ineffizienz zu kompensieren, allerdings sind solche Speicher bislang noch nicht in geeigneter Form experimentell umgesetzt worden.

Die von Jaromír Fiurášek und Nicolas Cerf vorgeschlagene emulierte Verschränkungsdistillation bietet einen neuen Weg, um iterative Distillationsprotokolle praktikabel zu machen. Die Grundidee ist die Verschiebung der Verschränkungsdistillation in die Nachbearbeitung der Daten, welche man durch geeignete Messung der verteilten Zustände erhalten hat. Die Emulation des Distillationsprotokolls erhöht die Erfolgswahrscheinlichkeit deutlich und ermöglicht gleichzeitig einen kompakten experimentellen Aufbau.

Der Hauptteil dieser Arbeit ist der experimentellen Demonstration der emulierten Verschränkungsdistillation von nicht-gaußschen Zuständen gewidmet, welche z.B. bei der Transmission durch einen verrauschten Kanal degaußifiziert wurden. Für die Simulation der verrauschten Transmission von verschränkten Zuständen wird ein zwei-Moden-gequetschter Zustand präpariert und dann absichtlich durch das Aufprägen von Phasenrauschen degaussifiziert. Die Distillation wurde umgesetzt durch *Eight-Port*-Homodynmessungen mit anschließender Nachbearbeitung der aufgenommenen Daten. Mithilfe dieses Aufbaus wurde zum ersten Mal das komplette iterative Distillationsprotokoll für bis zu drei Iterationsschritte durchgeführt. Die bearbeiteten Daten zeigen bei jedem Iterationsschritt eine signifikante Erhöhung der Verschränkung, der Reinheit und der Gaußizität.

Im zweiten Teil dieser Arbeit werden Änderungen in der experimentellen Umsetzung diskutiert, welche für die emulierte Distillation von gaußschen Zuständen notwendig sind, und erfolgreich mithilfe eines Testaufbaus demonstriert. Zentrale Punkte sind hierbei zum einen die Realisierung von Stabilisationstechniken der Quetschlicht-Quelle und des *Eight-Port*-Homodyndetektors, ohne dass ein helles Lichtfeld mit dem Signalfeld propagiert. Zudem wird die Umsetzung der *Eight-Port*-Homodyndetektion der gequetschten Zustände über einen weiten Frequenzbereich bis zu 100 MHz bei einem gleichzeitig flachen Spektrum demonstriert.

Schlüsselworte: Verschränkungsdistillation, Emulation, *Eight-Port*-Homodyndetektion

Contents

List of Figures

Glossary

List of Abbreviations

QKD	Quantum key distribution
E2CD	Elementary two-copy distillation
CV	Continuous variable
DV	Discrete variable
AC	Alternating current
DC	Direct current
dB	Decibel
PPT	Positive partial transpose
EHD	Eight-port homodyne detector
BHD	Balanced homodyne detector
APD	Avalanche photo detector
PIN	Positive doped, Intrinsic, Negative doped (semiconductor doping of photo diodes)
DBS	Dichroic beam splitter
PZT	Piezoelectric transducer
LO	Local oscillator
BS	Beam splitter
LOCC	Local operations and classical communications
HWP	Half-wave plate

List of symbols

$\mathcal{H}$	Hilbert space
$|\psi\rangle$	Quantum state vector
ρ	Density matrix of a quantum state
tr	Trace of an operator
$\otimes$	Tensor product
$\oplus$	Direct sum
$\mathcal{P}$	Purity
$\mathcal{P}_{\mathrm{G}}$	Gaussian purity
$S(\hat{\rho})$	Von Neumann entropy
$\hat{H}$	Hamiltonian
$\hat{M}_i$	Spectral projections of hermitian operator $\hat{M}$
m_i	Eigenvalues of hermitian operator $\hat{M}$
p_{m_i}	Probability for measurement outcome m_i
μ_n	Statistical moment of order n
μ_1	Expectation value/mean value
Var	Variance
σ	standard deviation
Skew	Skewness
Kurt	Kurtosis
ExKurt	Excess kurtosis
$F(\mathcal{H})$	Fock space
$\hat{O}$	Symmetrization operator
$\hat{a}$	Annihilation operator
$\hat{a}^{\dagger}$	Creation operator
$\hat{n}$	Number operator
$\hat{X}$	Amplitude quadrature operator
$\hat{P}$	Phase quadrature operator
X	Eigenvalues of $\hat{X}$
P	Eigenvalues of $\hat{P}$
$\hat{X}(\vartheta)$	Generic quadrature operator
$W(X,P)$	Wigner function
$Q(X,P)$	Q-function
$\mathrm{Cov}(\hat{A},\hat{B})$	Covariance of operators $\hat{A}$ and $\hat{B}$
γ	Covariance matrix
$\boldsymbol{x}$	State vector
$\hat{\boldsymbol{x}}$	Displacement vector
$\hat{D}(\alpha)$	Displacement operator

$\hat{S}(\zeta)$	Squeezing operator
Ω	Symplectic form
$(\mathrm{S}, \mathbf{d})$	Symplectic map
s_i	Symplectic eigenvalue
$\mathbb{1}$	Identity operator
τ	Amplitude transmissivity of beam splitter
ϱ	Amplitude reflectivity of beam splitter
$\bar{n}$	Mean photon number
a	Diagonal elements (variances) of the covariance matrix of a symmetric two-mode-squeezed state
b	Off-diagonal elements (covariances) of the covariance matrix of a symmetric two-mode-squeezed state
ϵ	Optical loss
$\Phi(\theta)$	Phase noise distribution
q	dephasing parameter

CHAPTER 1

Introduction

The existence of entanglement is one of the most fascinating topics in quantum mechanics. Einstein named it 'spooky action at a distance' and saw in it a proof that quantum mechanics is incomplete [1]. The name entanglement was coined by Erwin Schrödinger [2] and means that the system shows correlations stronger then classically possible. With the postulation of Bells inequality [3], a relation was given to check this property in specific scenarios. Subsequent experimental tests such as the seminal work of A. Aspect [4] have shown that quantum mechanics is not incomplete but that the idea of local reality has to be abandoned. Nowadays, entanglement is one of the most studied fields in quantum mechanics. It has application in various quantum information protocols such as quantum metrology or quantum computation [5–12]. Realizations of entanglement on the basis of discrete variables and continuous variables have been presented in various setups.

Entanglement can be used as an important resource, e.g. for *quantum key distribution* (QKD) in quantum cryptography protocols. While also protocols for QKD exist that do not rely on entanglement such as prepare-and-measure schemes like [13, 14], many important QKD protocols require entangled quantum states [8, 15–18]. The general idea is to enable secure communication between two parties, traditionally named Alice and Bob, so they cannot be eavesdropped. The important prerequisite, the secret key, needs to be securely distributed between the parties. The method of QKD provides the technique for such a secure distribution. Distribution of entangled states is thus the first step towards such entanglement based QKD protocols.

As the two parties in such a communication scenario are typically far away from

each other, entanglement distribution over long distances needs to be realized. This can be done airborne, e.g. using satellites [15, 19, 20] or via optical fibers [21,22]. In both cases however, detrimental effects like optical loss due to scattering and absorption, or decoherence effects like phase noise in optical fibers can occur. Unfortunately, entangled states of lights are very susceptible to such effects as they degrade or even fully destroy the nonclassical properties of the light. This significantly limits the distance on which entanglement can be distributed.

To counteract these effects and enable entanglement distribution even over lossy or noisy channels, *distillation protocols* are proposed. These protocols are applied after the entanglement is distributed and can be realized with local operations and classical communication only between the distant parties.

The general idea of entanglement distillation is to restore parts of the original entanglement by distilling a few strongly entangled states from a large amount of weakly entangled states [23–32]. In a simple elementary two copy distillation protocol, two copies of the input state are consumed and with some probability one copy with improved properties is produced [27, 28]. These elementary distillation steps can be iterated to restore even stronger entangled states than possible with a single distillation step [23, 24]. More concretely, this means that the already distilled states serve as input states for an additional iteration of the distillation protocol, resulting in a pyramid structure. An infinite amount of iterations of the distillation protocol is called asymptotic limit and would, in principle, result in the recovery of a strongly entangled state.

However, such a concatenation soon reaches the limits of what can be experimentally realized as each additional iteration doubles the amount of consumed copies of the original state. Furthermore, for each distillation step the two input states need to be available at the same time. As a consequence, this means that *all* elementary two copy distillations of one iteration step have to succeed simultaneously to provide the input states for the next iteration. Even if only one distillation did not succeed, all other distillation results have to be discarded. This significantly decreases the success probability of the protocol and consequently increases its time duration in such a way that a large amount of iterations is typically inefficient and unfeasible. Indeed, up to now, only two iteration steps were experimentally demonstrated [33].

Quantum memories [34] have been proposed to overcome these problems. These can be used to store the successful results of the elementary two copy distillations and to release them when all states are available for the next iteration step. Additionally, different schemes for the realization of entanglement distillation, relying on quantum memories that reduce the necessary experimental setup, were proposed recently, e.g. [35, 36]. However, quantum memories pose their own significant challenges on experimental hardware and suitable quantum memories

are not realized up to date.

This work is dedicated to the experimental realization of a different attempt to overcome the inefficiency of iterative distillation protocols. Based on theoretical findings developed by Jaromír Fiurášek and Nicolas Cerf, a so-called *emulated distillation protocol* is realized. The core idea is to characterize all relevant properties of the decohered states with an eight-port homodyne measurement and shift the distillation protocol to the postprocessing of the acquired data [37,38]. This does not only solve the problem of the enormous experimental effort, but also improves the success rate of the distillation protocol.

The idea of emulation was originally proposed for noiseless amplification [39–41], another rather complex and experimentally demanding protocol. Indeed, a successful experimental realization of the emulation of single-mode noiseless amplification has been reported in [42].

The emulated distillation protocol presented and realized in this thesis is based on the iterative distillation protocol as described above. As the distillation takes place in the postprocessing, the presented scheme allows us to create and measure copies needed as input states for one iteration one after an other in time, without the requirement to have all these states physically available at the same time. Moreover, the protocol circumvents the need for storing quantum states in memories. Thus, the number of iteration steps that can be realized is solely limited by the time duration of the measurement needed to require the necessary amount of data. As well the emulation enables insights in the dynamics of iterative protocols that are not accessible by a physical implementation as one can directly compare and investigate the distillation effect of different iteration steps.

Crucially, such an emulation is completely indistinguishable from a full physical implementation with even ideal quantum memories to anyone outside Alice and Bob's labs. The downside of the emulation technique is that, as the distilled states are already detected, they are not physically available for further downstream experiments. In the aforementioned QKD protocols, however, the states are eventually measured anyway, such that emulated distillation is especially interesting for QKD experiments where subsequent distillation can improve the possible key rate.

In this thesis we realized the emulated distillation protocol with *two-mode-squeezed states*, a specific form of entangled states in the *continuous variable* (CV) regime. Generally, two-mode-squeezed states are Gaussian states, a class of CV states, that is well characterizable in terms of entanglement. However, e.g. phase noise alters in such a way that they are not Gaussian anymore. We will refer to these states as dephased two-mode-squeezed states. This distinction is impor-

tant, as the so-called *no-go theorem* predicts, that the distillation of Gaussian states with Gaussian methods is not possible [43–45]. Here, Gaussian operations correspond to those operations which preserve the Gaussian character of a state. Importantly, most operations that are usually performed in the laboratory are of exactly this type.

The no-go theorem thus poses a significant restriction to the possibility of distillation in the CV regime as it forces us to leave the Gaussian regime in order to realize distillation. This restriction is therefore dividing the possible distillation protocols of CV states in two subgroups: Distillation of non-Gaussian states, possible with Gaussian methods only, and distillation of Gaussian states which requires a non-Gaussian operation to be included in the distillation process.

Since typical detrimental effects like phase noise degaussify the entangled state, as stated before, there is a huge need for protocols of the first type. The main part of the thesis is therefore dedicated to the experimental realization of emulated distillation of phase diffused states. In accordance with the no-go theorem only Gaussian methods are needed for this realization and the successful performance of the emulated distillation is shown and investigated within this thesis.

The proposal of emulated iterative distillation and some of the experimental results of this experiment are published in [46].

The second part of this thesis concerns optical losses, which are unavoidable in experiments. This effect preserves the Gaussianity of an entangled state but still decreases its entanglement. To counteract this problem, the distillation of such states has been progressed in the last years. Protocols ranging from photon subtraction to the above mentioned noiseless amplification have been proposed and experimentally realized, e.g. [30–32,39–41,47,48]. All these protocols include a non-Gaussian operation, in most cases realized by including an avalanche photo detector into the experimental setup. Such detectors are able to detect single photons and can thus realize non-Gaussian operations like photon subtraction. However, the implementation of single photon detectors requires special experimental techniques as these devices are extremely sensitive to already small light powers. Typical methods, generally used for state preparation and detection in the presence of bright light fields, are thus not possible for such a setup. The second part of the thesis is therefore dedicated to investigate necessary changes for the experimental setup of emulated distillation against optical losses. Different techniques which are already established in other fields of research are combined to provide a state preparation and detection scheme that is possible to be combined with single photon detectors.

This thesis is structured as follows. Chapter 2 covers the theoretical basics that are needed to understand the content of this thesis. Experimental techniques and methods used for the realization of the experiments are presented in Chapter 3. Specific experimental details are as well given in the respective chapters. The concepts of general entanglement distillation and emulated entanglement distillation are explained in Chapter 4. Chapter 5 presents the experimental realization of the emulated distillation protocol performed on phase diffused states which includes a detailed description of the experimental setup as well as a discussion of the results. In Chapter 6, changes to the previously presented experimental setup are discussed which allow for distillation against optical loss. Based on this considerations, we provide an experimental realization of a test setup for a stabilized squeezed light measurement with an eight-port homodyne detector without the need of a bright light field that co-propagates with the signal field. Chapter 7 contains the conclusion and outlook of this thesis.

CHAPTER 2

Theoretical framework

Several properties of a light field that are experimentally detectable can only be explained on the basis of a quantum mechanical description of the physical system. In this chapter we recall the standard theoretical description of the light field needed for typical quantum optics experiments. For this, the formalisms of quantum mechanics demand us to specify three basic parts: the *preparation*, the *dynamics* and the *measurement* of the light field. Specifying the *preparation* is synonymous to determining the initial quantum mechanical state of the quantum system. This can be thought of as the description of the properties of the light field right after its generation within the laser. The preparation thus describes the quantum mechanical source, that is e.g. the laser, itself.

Knowing the *dynamics* of the quantum state allows us to infer the properties of the light field at later instances of time, e.g. if the light field traversed freely in space or if the light field was changed by optical components such as, say, beam splitting devices.

While the quantum state of the light field describes all its physical properties, one does in general not access to the quantum state directly. This is why measurements have to be performed. Depending on the type of the measurement, this gives access to different properties of the quantum state. Roughly speaking, measurements provide the link to the abstract theoretical description of a light field and allow us to specify the quantum state of the system.

The main contribution of this thesis, i.e. the experimental realization of emulated entanglement distillation, essentially relies on quantum theory. As a con-

sequence, it is essential to be familiar with the quantum mechanical description of all experimental and theoretical constituents within this work to understand the content of this thesis. The purpose of this chapter is therefore to set the theoretical basis for our discussions and results in the following chapters, in which techniques and methods of (emulated) entanglement distillation are presented in detail.

2.1 Quantum mechanics in a nutshell

In this section we briefly review the abstract quantum mechanical formalism and thereby give more precise meanings to the notions of preparation, dynamics and measurement just introduced.

The abstract theoretical framework presented here applies to any quantum system, not only light fields. We provide the connection to the special case of light fields in the next section.

2.1.1 The preparation of a quantum system

The theory of quantum mechanics is centered around the concept of *quantum states*, which encode all measurable quantities of a specific quantum system [49]. If we generate a light field in the laboratory, then what we do from a theoretical perspective is to *prepare* a quantum system in a specific quantum state.

The space of all such states is mathematically described by a Hilbert space $\mathcal{H}$, which for the purposes of this thesis can be thought of as a complex vector space. It should be noted that the exact mathematical definition of a Hilbert space is much more involved than this, especially in the case of infinite-dimensional quantum systems. In this thesis however, we do not specifically use such definitions, but rather provide an intuitive picture of the quantum mechanical framework needed to understand the content and results of this thesis.
Interpreting the quantum space as a complex vector space means that quantum states, i.e. the elements of the Hilbert space, are just complex vectors. We will typically employ the Dirac notation and denote such states by the "ket" symbol, i.e. we write for example $|\psi\rangle$ to denote a specific state of the quantum system.

The state of a quantum system is not necessarily completely specified by a vector $|\psi\rangle$ in Hilbert space, but can also be in a statistical mixture of two or more states $|\psi_i\rangle \in \mathcal{H}$. This is mathematically phrased using the density operator formalism: If we are given a probability distribution $\{P_i\}$, i.e. $P_i \geq 0$ for all i and $\sum_i P_i = 1$, where P_i denotes the probability with which the quantum system is in state $|\psi_i\rangle$,

the density matrix $\hat{\rho}$ of the quantum system is defined as [49]

$$\hat{\rho} = \sum_i P_i |\psi_i\rangle\langle\psi_i| \,. \tag{2.1}$$

Here we employ the standard notation that $|\psi_i\rangle\langle\psi_i| = |\psi_i\rangle \otimes \langle\psi_i|$ where $\langle\psi_i|$ is the conjugate transpose of the vector $|\psi_i\rangle$. The quantity $|\psi_i\rangle\langle\psi_i|$ (and thus the density matrix $\hat{\rho}$) therefore corresponds to a (in general infinite-dimensional) matrix. The density matrix has always unit trace. To see this, note that $\mathrm{tr}[|\psi_i\rangle\langle\psi_i|] = 1$ irrespective of the vector $|\psi_i\rangle$ and therefore

$$\mathrm{tr}[\hat{\rho}] = \sum_i P_i \,\mathrm{tr}[|\psi_i\rangle\langle\psi_i|] = \sum_i P_i = 1 \,, \tag{2.2}$$

since $\{P_i\}$ is a probability distribution.

If $P_i = 1$ for some fixed i, all other probabilities must be zero. In this case the density matrix is simply given as $\hat{\rho} = |\psi_i\rangle\langle\psi_i|$ which means that the state of the quantum state is completely specified by the vector $|\psi_i\rangle$. A quantum state is called *pure* if the density matrix $\hat{\rho}$ can be written in such a form, i.e. if it can be written as $\hat{\rho} = |\psi_i\rangle\langle\psi_i|$ for some vector $|\psi_i\rangle \in \mathcal{H}$. A quantum state which is not pure is called *mixed*.

Determining whether or not a quantum state is mixed is interesting as it allows to infer whether an initially pure state was affected by detrimental effects. Such effects will in general change the state from pure to mixed and thereby also change the quantum properties of the initial state. There are several ways to decide whether a quantum state is pure or mixed: The first is of course to employ the definition above and check whether the state can be written as $\hat{\rho} = |\psi\rangle\langle\psi|$ for some vector $|\psi\rangle \in \mathcal{H}$. This strategy however will generally require us to test an infinite number of possible vectors $|\psi\rangle$. Instead, the following two more feasible methods are typically employed to quantify the mixedness of a quantum state: The first method is to compute the so-called purity $\mathcal{P}$ of a quantum state $\hat{\rho}$ defined via [49]

$$\mathcal{P} = \mathrm{tr}[\hat{\rho}^2] \,. \tag{2.3}$$

This quantity can take values in $[1/d\,, 1]$ with d being the dimension of the Hilbert space $\mathcal{H}$. It attains the maximal value 1 if and only if $\hat{\rho}$ is a pure state and attains the minimal value $1/d$ for the completely mixed state $\hat{\rho}$.

The second method is to determine the *von Neumann entropy* S of a quantum state $\hat{\rho}$ defined via

$$S(\hat{\rho}) = -\mathrm{tr}[\hat{\rho}\ln\hat{\rho}] \,,$$

which vanishes if and only if $\hat{\rho}$ is pure.

All these strategies to decide require us to have a description of the quantum state on the basis of the density matrix $\hat{\rho}$. Indeed the density matrix formalism encompasses the most general quantum states possible in quantum theory. In many situations however reconstructing the density matrix from measurement outcomes is quite difficult, e.g. if the density matrix is infinite-dimensional this can only be achieved to finite accuracy. Fortunately, the most important quantum states in this thesis, namely *Gaussian quantum states*, can be completely specified by a finite so-called covariance matrix, although the corresponding density matrix is infinite-dimensional. We will introduce both, these states and the covariance matrix, later in this chapter. The reason why we mention these states here is that for such states the purity $\mathcal{P}$ from Eq. (2.3) can be expressed in simpler terms *without* the density matrix $\hat{\rho}$ as we present in Section 4.2.1.

2.1.2 The dynamics of a quantum system

The density matrix formalism from the previous section can be used to completely specify the state of a quantum system immediately after its preparation. In typical situations however the quantum system will change in time: For example, in a quantum optical experiment a light field will traverse several optical components such as beam splitting devices or optical amplifiers. In this section we recall the theoretical description of these dynamics of a quantum system.

The most general description of the dynamics of a quantum system is given by a so-called *quantum channel* [49]. The intuition behind this concept is the following: Since the state of a quantum system is specified by a density matrix, the most general dynamics is simply a mapping between density matrices. This just means that any dynamics of a quantum system simply takes the density matrix $\hat{\rho}$ of an initial state of a quantum system and maps it to the density matrix $\hat{\rho}'$ of the final state of the quantum system. The mapping cannot be completely arbitrary to achieve this task: Since it has to map between density matrices, it must for example be trace-preserving since density matrices always have unit trace, c.f. Section 2.1.1. Moreover, the mapping must be linear and completely positive — both notions not so important for the content of this thesis and whose definition can be found in [49].

A mapping which satisfies all these properties, i.e. it is trace-preserving, linear and completely positive, is called a *quantum channel*. While we will detail two examples of quantum channels which are important to describe the dynamics of light fields, namely phase shifts and beam splitting devices, in Section 2.2.7, let us here provide the example of the following simple, well-known quantum channel: Even in the case where the quantum system is isolated, for example a light field propagating freely in space, the quantum state of that system will change with

time. This free time evolution is governed by the Schrödinger equation

$$\hat{\rho}(t) = \mathrm{e}^{i\hbar\hat{H}/t}\hat{\rho}\mathrm{e}^{-i\hbar\hat{H}/t}\,,$$

where $\hat{\rho}$ is the density matrix describing the initial state of the quantum system, $\hat{\rho}(t)$ is the state after free evolution for time t and $\hat{H}$ is the so-called *Hamiltonian* of the quantum system. One can show that this mapping between initial and final quantum state satisfies all of the above three properties, which means that free time evolution just corresponds to applying a specific quantum channel.

2.1.3 Measuring a quantum system

Consider a quantum mechanical system in state $\hat{\rho}$. This can either be the state right after preparing the quantum system or after the quantum system underwent some dynamics. In order to determine the properties of this quantum state, we need to employ measurements. For example, in a quantum optical experiment these measurements are typically realized by specific photo detectors.

Theoretically, quantum mechanical measurements can be described by *Hermitian* operators on the Hilbert space. Any such operator $\hat{M}$ therefore satisfies $\hat{M} = \hat{M}^{\dagger}$ and has a spectral decomposition, which means that we can always write [49]

$$\hat{M} = \sum_i m_i \hat{M}_i \tag{2.4}$$

where $m_i \in \mathbb{R}$ are the eigenvalues and $\hat{M}_i$ are the spectral projections of $\hat{M}$. The eigenvalues m_i correspond to the possible measurement outcomes. The probability p_{m_i} to obtain this outcome m_i if the quantum system is in state $\hat{\rho}$ is then given by

$$p_{m_i} = \mathrm{tr}[\hat{\rho}\hat{M}_i]. \tag{2.5}$$

The set $\{p_{m_i}\}_i$ of probabilities for each outcome m_i is called a *probability distribution*. Directly after the measurement, the post-measurement state $\hat{\rho}_{m_i}$ is given as

$$\hat{\rho}_{m_i} = \frac{1}{p_{m_i}}\hat{M}_i\hat{\rho}\hat{M}_i\,. \tag{2.6}$$

Since this prescription is rather abstract, let us give some intuition how all these quantities relate to experimental quantities: For this we consider a light field generated in a laser, which traverses some optical components before being detected by a photo detector. We already know that the initial generation of the light field in the laser corresponds to a preparation, i.e. a specific density matrix. We also know that free time evolution and the optical components induce

a certain dynamics on this density matrix which is theoretically described by a quantum channel. The density matrix $\hat{\rho}$ appearing in Eq. (2.5) is the description of the state *immediately before* the measurement happens, i.e. before the light field is being detected. In contrast, the Hermitian operator $\hat{M}$ (and therefore also the spectral projections $\hat{M}_i$ in Eq. (2.5)) corresponds to the abstract description of the photo detector. Both descriptions together, that is the state of the light field immediately before the measurement as well as the description of the measurement device, then determine the outcome probabilities p_{m_i} of the measurement.

This is in principle everything we need for a quantum mechanical description: Preparation, dynamics and measurement of a quantum system basically describe all quantum mechanical protocols and experiments. The notions presented so far are still very abstract but can be filled with much more content for the quantum system of a light field as we will see in Section 2.2. However, things can also be fairly complicated when dealing with such systems: For example, measurements then typically have a continuous spectrum of measurement outcomes m_i. The probability distribution $\{p_{m_i}\}$ then corresponds to a list containing infinitely many entries, which is neither experimentally accessible nor a feasible description. Instead of trying to deal with these infinitely many entries of the probability distribution, one typically concentrates on certain characteristic properties of the distribution. These properties are called *statistical moments* and allow us to qualitatively characterize the probability distribution without listing all its entries. Since these statistical moments are important for the remainder of this thesis, we dedicate the following section to their definition and properties.

Statistical moments

Consider a random variable M with probability distribution $\{p_{m_i}\}_i$ where p_{m_i} denotes the probability that the random variable M outputs the value m_i. The *statistical moment μ_n of order $n \in \mathbb{N}$* of M is defined as

$$\mu_n = \sum_i p_{m_i} m_i^n \ . \tag{2.7}$$

These moments characterize the "shape" of the probability distribution p_{m_i}. The first moment μ_1 is typically known as the *expectation value*, whereas the second moment μ_2 is related to what is known as the *variance* of the distribution. We will provide the exact definitions below.

Note that the definition in Eq. (2.7) is purely classical; no quantum mechanical notions are involved. However, the transition to quantum mechanics is simple: The combination of quantum state $\hat{\rho}$ and hermitian operator $\hat{M}$ can be understood as a random variable which also yields as an output the value m_i, i.e.

an eigenvalue of $\hat{M}$, with probability p_{m_i}. It is in this sense that we also refer to the n-th statistical moment of the operator $\hat{M}$ which also depends on the state $\hat{\rho}$.

Let us now provide more details for the most important statistical moments: the moments of order $n = 1,...,4$. The first statistical moment μ_1 of $\hat{M}$ is according to Eq. (2.7) defined as

$$\mu_1 = \sum_i p_{m_i} m_i = \sum_i \text{tr}[\hat{\rho}\hat{M}_i] m_i = \text{tr}[\hat{\rho}\hat{M}] \equiv \langle \hat{M} \rangle \ , \qquad (2.8)$$

where we used Eq. (2.5) and the spectral decomposition Eq. (2.4) of $\hat{M}$. This quantity $\langle \hat{M} \rangle$ is called the *expectation value* (or *mean value*) of $\hat{M}$. The mean value indicates around which value the probability distribution is centered.

The second statistical moment μ_2 of an operator $\hat{M}$ is given by

$$\mu_2 = \sum_i p_{m_i} m_i^2 \ .$$

It is related to what is called the *variance* of $\hat{M}$ which is defined as

$$\text{Var}(\hat{M}) = \sum_i p_{m_i} (m_i - \langle \hat{M} \rangle)^2 \ .$$

The variance of $\hat{M}$ therefore corresponds to a shifted version of μ_2, where the mean value $\langle \hat{M} \rangle$ is subtracted from each measurement outcome m_i. Conversely, the second μ_2 can be understood as the variance of an operator $\hat{M}$ with mean value $\langle \hat{M} \rangle = 0$. This construction where only the difference between outcome m_i and mean value $\langle \hat{M} \rangle$ is accounted for is commonly referred to as the *central statistical moments*. Consequently, the variance corresponds to the central statistical moment of order 2.

Intuitively, both the second moment μ_2 as well as the variance $\text{Var}(\hat{M})$ characterize the "width" of a probability distributions and indicate how much the values m_i spread around the mean value $\langle \hat{M} \rangle$. Hence, these notions can be used to quantify our level of "uncertainty" about the random variable (in the classical case) or the quantum state $\hat{\rho}$ (in the quantum case): For example, if the variance $\text{Var}(\hat{M})$ of $\hat{M}$ is zero, then we know that the measurement of the corresponding quantum state $\hat{\rho}$ always outputs the same measurement outcome $m_i = \langle \hat{M} \rangle$ deterministically — there is no "uncertainty" about which measurement outcome will be obtained next. It is this concept of uncertainty which is treated in the famous uncertainty relations, which indeed are typically phrased using variances and which we will discuss in Section 2.1.4. As a consequence the concept of variances is

essential to understand the effect of some nonclassical operations on light fields, such as squeezing (see Section 2.2.4).

It is common to also use an equivalent definition of the variance obtained via

$$
\begin{aligned}
\mathrm{Var}(\hat{M}) &= \sum_i p_{m_i}(m_i - \langle \hat{M} \rangle)^2 \\
&= \langle (\hat{M} - \langle \hat{M} \rangle)^2 \rangle \\
&= \langle \hat{M}^2 - \hat{M}\langle \hat{M} \rangle - \hat{M}\langle \hat{M} \rangle + \langle \hat{M} \rangle \langle \hat{M} \rangle \rangle \\
&= \langle \hat{M}^2 \rangle - \langle \hat{M} \rangle \langle \hat{M} \rangle - \langle \hat{M} \rangle \langle \hat{M} \rangle + \langle \hat{M} \rangle \langle \hat{M} \rangle \\
&= \langle \hat{M}^2 \rangle - \langle \hat{M} \rangle^2 \ .
\end{aligned}
$$

Moreover, the *standard deviation* $\sigma_{\hat{M}}$ of an operator $\hat{M}$ is defined as the square root of the variance $\mathrm{Var}(\hat{M})$, i.e.

$$
\sigma_{\hat{M}} = \sqrt{\mathrm{Var}(\hat{M})} \ .
$$

Similarly to the second statistical moment μ_2 and the more prominent variance, the third statistical moment μ_3 is less known than a quantity very much related to it: the so-called *skewness*. The skewness $\mathrm{Skew}(\hat{M})$ of an operator $\hat{M}$ is defined as

$$
\mathrm{Skew}(\hat{M}) = \frac{\langle (\hat{M} - \langle \hat{M} \rangle)^3 \rangle}{(\sigma_{\hat{M}})^3} \ . \tag{2.9}
$$

It therefore corresponds to the third central moment $\langle (\hat{M} - \langle \hat{M} \rangle)^3 \rangle$ of $\hat{M}$ divided by the third power of the standard deviation $\sigma_{\hat{M}}$. This normalization, i.e. the division by the corresponding power of the standard deviation, is known as "standardization". The skewness is hence the standardized statistical moment of order 3.

The skewness is a marker for the "lopsidedness" of the distribution. For a symmetric distribution it is zero. Whereas a symmetric distribution is a sufficient criterion for vanishing skewness, it is not necessary. A positive skewness indicates a stronger "tail" on the right side of the distribution while a negative skewness indicates a stronger "tail" on the left side.

The last statistical moment which is important for the content of this thesis is the fourth standardized moment, the so-called *kurtosis*. The kurtosis is a measure for the 'tailedness' of a distribution and is defined by

$$
\mathrm{Kurt}(\hat{M}) = \frac{\langle (\hat{M} - \langle \hat{M} \rangle)^4 \rangle}{(\sigma_{\hat{M}})^4} \ .
$$

Note again the similarity between this quantity and the statistical moment μ_4. Due to the fact that the kurtosis is a moment of fourth power, it can only have positive values. A normal distribution has a kurtosis of exactly 3. To obtain a measure which becomes zero for a normal distribution one typically defines the so-called *excess kurtosis* ExKurt of an operator $\hat{M}$ via

$$\text{ExKurt}(\hat{M}) = \frac{\langle (\hat{M} - \langle \hat{M} \rangle)^4 \rangle}{(\sigma_{\hat{M}})^4} - 3 \;. \tag{2.10}$$

2.1.4 Uncertainty relation

In quantum mechanics it is not possible to measure two observables simultaneously and precisely if the operators do not commute. Mathematically this can be expressed using the variances introduced above to quantify the "precision" of the measurements. More concretely, one can show that for any two hermitian operators $\hat{A}$ and $\hat{B}$ (i.e. for any two measurements) the following inequality holds [50,51]:

$$\text{Var}(\hat{A})\text{Var}(\hat{B}) \geq \frac{1}{4} |\langle [\hat{A}, \hat{B}] \rangle|^2 \;, \tag{2.11}$$

where $[\hat{A}, \hat{B}] = \hat{A}\hat{B} - \hat{B}\hat{A}$ is the commutator of $\hat{A}$ and $\hat{B}$. If the two operators do not commute, i.e. $[\hat{A}, \hat{B}] \neq 0$, then the product of the variances $\text{Var}(\hat{A})$ and $\text{Var}(\hat{B})$ is lower bounded by a positive quantity. This implies that for such operators, it is impossible to find a state $\hat{\rho}$ such that both variances vanish. There will hence always be some amount of uncertainty in the two measurements. The inequality Eq. (2.11) is therefore known as an *uncertainty relation.*

Uncertainty relations lie at the heart of quantum mechanics as they express a fundamental difference between quantum and classical physics. We did however not introduce these relations for this reason, but rather as an easy-to-check criterion for the "physicality" of a quantum state. What we mean by this is the following: For any fixed two operators $\hat{A}$ and $\hat{B}$, Eq. (2.11) is satisfied for *all* quantum states. If we however obtain variances $\text{Var}(\hat{A})$ and $\text{Var}(\hat{B})$ whose product is below the threshold given in Eq. (2.11), then this implies that the corresponding description of the state was unphysical. We will see in Section 2.3.2 how this notion of "physicality" will help in witnessing a purely-quantum feature known as entanglement.

2.2 Quantum mechanics for light fields

In the previous section, we explained the quantum mechanical approach to describe *general* physical systems. Now, we focus on the quantum mechanical de-

scription of a light field which belongs to a special class of physical systems, namely so-called bosonic systems.

2.2.1 The Fock space

The physical system of a light field typically consists of a varying amount of identical bosonic particles (the photons). The appropriate Hilbert space of a light field, known as *Fock space*, was first introduced by V. A. Fock in 1932 and is constructed as follows: Denote by $\mathcal{H}$ the Hilbert space of a single particle. The elements of this space are the (pure) quantum states $|\psi\rangle$ that the single particle can be prepared in.

The corresponding two particle Hilbert space is then given as $\mathcal{H} \otimes \mathcal{H}$, where $\otimes$ is the tensor product. In this thesis we only deal with bosonic particles which means that the particles are indistinguishable from each other. A state of two bosonic particles should thus be symmetric with respect to swapping of the particles, such as e.g. the state $|\psi\rangle \otimes |\psi\rangle$, where $|\psi\rangle \in \mathcal{H}$. The two particle Hilbert space $\mathcal{H} \otimes \mathcal{H}$ however also contains states which are *not* symmetric in this sense such as e.g. $|\psi_1\rangle \otimes |\psi_2\rangle$ with $|\psi_1\rangle \neq |\psi_2\rangle$. In order to "get rid" of these dissymmetric states, a symmetrization operator O is typically employed such that the corresponding space $O(\mathcal{H} \otimes \mathcal{H})$ only contains the symmetric two particle states. Employing the exact same procedure also yields the bosonic three particle Hilbert space $O(\mathcal{H} \otimes \mathcal{H} \otimes \mathcal{H})$, the bosonic four particle Hilbert space $O(\mathcal{H} \otimes \mathcal{H} \otimes \mathcal{H} \otimes \mathcal{H})$ and so on and so forth. Since we do not know the exact number of particles emitted by the laser, the Hilbert space $F(\mathcal{H})$ of the complete light field is given by the direct sum of all possible bosonic n-particle Hilbert spaces, where $n \in \mathcal{N}$ is the number of particles, i.e.

$$F(\mathcal{H}) = \bigoplus_{n=0}^{\infty} O(\mathcal{H}^{\otimes n}) = \mathbb{C} \oplus \mathcal{H} \oplus (O(\mathcal{H} \otimes \mathcal{H})) \oplus (O(\mathcal{H} \otimes \mathcal{H} \otimes \mathcal{H})) \oplus \ldots \quad .$$

Note that both the single particle Hilbert space $\mathcal{H}$ as well as the one-dimensional "zero particle" Hilbert space $\mathbb{C}$ only contain symmetric states and hence do not need to be symmetrized by the operator O.

The space $F(\mathcal{H})$ is called the *Fock space* and is infinite-dimensional. This makes a mathematically rigorous treatment typically rather involved. In this thesis we will not deal with the mathematical intricacies of such a treatment and rather provide a conceptual quantum mechanical picture which grants the intuition to understand the content of this thesis.

A convenient basis of the Fock space is the so-called *Fock basis* (also called the number state basis) denoted by $\{|n\rangle\}_{n=0}^{\infty}$. The fact that $\{|n\rangle\}$ is a basis of Fock space simply means that any vector $|\phi\rangle \in F(\mathcal{H})$ can be written as a superposition

of the basis vectors, i.e. $|\phi\rangle = \sum_n \alpha_n |n\rangle$ with α_n some complex coefficients. Physically, an element $|n\rangle$ of the Fock basis can be understood as the state of a light field which contains exactly n identical particles.

Consecutive basis elements are linked by the so-called *creation* operator $\hat{a}^\dagger$ and the *annihilation* operator $\hat{a}$ through [52]

$$\hat{a}^\dagger |n\rangle = \sqrt{n+1} |n+1\rangle \quad (\text{for } n \geq 0) \,. \tag{2.12}$$

and

$$\hat{a} |n\rangle = \sqrt{n} |n-1\rangle \quad (\text{for } n \geq 1) \,. \tag{2.13}$$

In addition to that the annihilation operator $\hat{a}$ acts trivially on the so-called *vacuum state* $|0\rangle$, i.e. $\hat{a}|0\rangle = 0$.

The effect of these two operators on the Fock states explains their name as they create or annihilate a photon and thereby raise or lower the photon number in the respective state. The annihilation and creation operators obey the commutation relation

$$[\hat{a}, \hat{a}^\dagger] = 1 \,.$$

Note that $\hat{a}$ and $\hat{a}^\dagger$ are both not hermitian, hence they do not correspond to measurements (see Section 2.1.3). It is however possible to construct hermitian operators from $\hat{a}$ and $\hat{a}^\dagger$. One possibility to consider the product $\hat{n} = \hat{a}^\dagger \hat{a}$, which indeed is hermitian and satisfies

$$\hat{n} |n\rangle = n |n\rangle$$

for any Fock state $|n\rangle$. This means that the operator $\hat{n}$ measures the number n of photons in a Fock state $|n\rangle$, which is why this operator is typically referred to as the *number operator*.

The so-called quadrature operators which we introduce in the next section correspond to another possibility to obtain hermitian operators from $\hat{a}$ and $\hat{a}^\dagger$.

2.2.2 The Wigner function

There are many equivalent ways to specify the state of a quantum mechanical system, one being the density matrix formalism introduced in Section 2.1.1. Another specification of the quantum state is provided by the *Wigner function*, named after E.P. Wigner. The definition of this function is based on so-called *quadrature operators* $\hat{X}$ and $\hat{P}$. These operators are defined as [7]

$$\hat{X} = \hat{a} + \hat{a}^\dagger \,,$$
$$\hat{P} = \mathrm{i}(\hat{a}^\dagger - \hat{a}) \,.$$

The operator $\hat{X}$ is typically called the *amplitude quadrature*, whereas $\hat{P}$ is called the *phase quadrature*.

The quadrature operators $\hat{X}$ and $\hat{P}$ originate from the position and momentum operators $\hat{x} = \sqrt{\frac{\hbar}{2\omega}}(\hat{a} + \hat{a}^\dagger)$ and $\hat{p} = i\sqrt{\frac{\hbar\omega}{2}}(\hat{a}^\dagger - \hat{a})$ which satisfy the commutation relation $[\hat{x},\hat{p}] = i\hbar$ [53]. The quadrature operators are obtained by a normalization of $\hat{x}$ and $\hat{p}$ to dimensionless variables. This normalization will result in a variance of the vacuum noise of unity [7] which is used throughout this thesis. In the literature there exists no general consensus about the normalization and one can also find normalizations corresponding to a vacuum noise variance of 1/2 or 1/4.

In contrast to the annihilation and creation operator $\hat{a}$ and $\hat{a}^\dagger$ (see Eqs. (2.12) and (2.13)), the quadrature operators are hermitian. Hence, they correspond to specific measurements of the light field: The hermiticity of the quadrature operators implies that they have a spectral decomposition, i.e. they can be written as [7]

$$\hat{X} = \sum_{X=-\infty}^{+\infty} X|X\rangle\langle X|$$

with eigenvalues X and eigenvectors $|X\rangle$ for the amplitude quadrature $\hat{X}$, and analogously for the phase quadrature $\hat{P}$ (with eigenvalues P and eigenvectors $|P\rangle$).

The probability to obtain measurement outcome X if we measure $\hat{X}$ on the state $\hat{\rho}$ is therefore given as

$$p_X = \text{tr}[\hat{\rho}|X\rangle\langle X|] \equiv \text{prd}(X) \tag{2.14}$$

and analogously we obtain the probability $\text{prd}(P)$ to obtain outcome X for the measurement of the phase quadrature $\hat{P}$.

Later on, it will be convenient to also introduce the *generic quadrature operator* $\hat{X}(\vartheta)$ defined as

$$\hat{X}(\vartheta) = \hat{a}e^{-i\vartheta} + \hat{a}^\dagger e^{i\vartheta} = \hat{X}\cos\vartheta + \hat{P}\sin\vartheta \,, \tag{2.15}$$

where $\vartheta \in [0,2\pi]$. Clearly, the generic quadrature operator $\hat{X}(\vartheta)$ includes the amplitude and phase quadrature $\hat{X}$ and $\hat{P}$, respectively, for specific values of ϑ. More concretely, we have $\hat{X}(0) = \hat{X}$ and $\hat{X}(\pi/2) = \hat{P}$.

The *Wigner function* $W(X,P)$ of a quantum system in state $\hat{\rho}$ is then defined as

$$W(X,P) = \frac{1}{4\pi}\int_{-\infty}^{\infty} dx e^{iPx/2}\left\langle X - \frac{x}{2}\right|\hat{\rho}\left|X + \frac{x}{2}\right\rangle \,. \tag{2.16}$$

Just as the density matrix $\hat{\rho}$, this function contains all information about the state of the quantum system. An advantage of this description is that it allows us to

visualize the quantum state: Consider the two-dimensional plane (X,P) spanned by the eigenvalues of the quadrature operators $\hat{X}$ and $\hat{P}$. This plane is also referred to as the *phase space*. By construction, the Wigner function $W(X,P)$ is just a real-valued function on this plane. The quantum state corresponding to the Wigner function $W(X,P)$ can therefore be visualized by a three-dimensional plot — in contrast to the rather unpractical density matrix ρ, which is infinite-dimensional. We will provide such visualizations of some prominent quantum states, which are important for this thesis, in the Section 2.2.4.

The Wigner function $W(X,P)$ of a quantum system is normalized, i.e. [54]

$$\int\int W(X,P)dXdP = 1 \,.$$

Moreover, it can be used to directly compute the probability distributions $\mathrm{prd}(X)$ and $\mathrm{prd}(P)$ of the quadrature measurements of the light field via

$$\mathrm{prd}(X) = \int_{-\infty}^{\infty} W(X,P)dP \,, \tag{2.17}$$

$$\mathrm{prd}(P) = \int_{-\infty}^{\infty} W(X,P)dX \,.$$

The Wigner function provides as well a handy tool for calculations such as the overlap formula [54]

$$\mathrm{tr}[\hat{A}_1\hat{A}_2] = 2\pi \int\int W_1(X,P)W_2(X,P)dXdP$$

where the Wigner functions W_1 and W_2 are given in form of Eq. (2.16) but with the operators $\hat{A}_1$ and $\hat{A}_2$ replacing the density matrix ρ. This equation can be used e.g. to calculate the purity $\mathcal{P}$ of the state, Eq. (2.3), by the Wigner function via

$$\mathcal{P} = \mathrm{tr}[\hat{\rho}^2] = 2\pi \int\int W(X,P)^2 dXdP \,, \tag{2.18}$$

or for a representation of the mean value μ_1, Eq. (2.8), given by

$$\mu_1 = \mathrm{tr}[\hat{\rho}\hat{A}] = 2\pi \int\int W(X,P)W_A(X,P)dXdP \,. \tag{2.19}$$

2.2.3 Covariance matrix

Another useful representation of a quantum state is given by the *covariance matrix*. Although it does for most states not capture all its properties (in contrast to the density matrix or the Wigner function), the covariance matrix is handy to employ

the "physicality" criterion on the basis of the uncertainty relation as we explain in this section. Moreover, for a special class of states, the *Gaussian states* (see Section 2.2.4), the specification of the covariance matrix is sufficient to describe the state completely.

The covariance matrix is based on the definition of the so-called covariance, which is a correlation measure for two random variables (which follow some joint probability distribution): For two operators $\hat{A}$ and $\hat{B}$, the *covariance* $\mathrm{Cov}(\hat{A},\hat{B})$ is defined as

$$\mathrm{Cov}(\hat{A},\hat{B}) := \frac{1}{2}\big(\langle\hat{A}\hat{B}\rangle + \langle\hat{B}\hat{A}\rangle\big) - \langle\hat{A}\rangle\langle\hat{B}\rangle \ .$$

From the definition it is clear that the covariance is symmetric in its arguments. Moreover, if $\hat{A} = \hat{B}$, the covariance of $\hat{A}$ and $\hat{B}$ simply reduces to the variance, i.e. $\mathrm{Cov}(\hat{A},\hat{B}) = \mathrm{Var}(\hat{A}) = \mathrm{Var}(\hat{B})$. Based on this definition the *covariance matrix* γ for the two operators $\hat{A}$ and $\hat{B}$ is defined as

$$\gamma = \begin{pmatrix} \mathrm{Var}(\hat{A}) & \mathrm{Cov}(\hat{A},\hat{B}) \\ \mathrm{Cov}(\hat{A},\hat{B}) & \mathrm{Var}(\hat{B}) \end{pmatrix} \ . \tag{2.20}$$

The covariance matrix is real ($\gamma = \gamma^*$), symmetric ($\gamma_{i,j} = \gamma_{j,i}$) and positive semi-definite ($\gamma \geq 0$). The inequality $\gamma \geq 0$ means that all eigenvalues of the matrix γ must be non-negative, i.e. $\min\{\mathrm{eig}(\gamma)\} \geq 0$.

The uncertainty relation from Section 2.1.4 takes a very specific form if the operators $\hat{A}$ and $\hat{B}$ are chosen to be the amplitude quadrature $\hat{X}$ and the phase quadrature $\hat{P}$, respectively: Since $[\hat{X},\hat{P}] = 2\mathrm{i}$, the uncertainty relation reads [52]

$$\mathrm{Var}(\hat{X})\mathrm{Var}(\hat{P}) \geq \frac{1}{4}|\langle[\hat{X},\hat{P}]\rangle|^2 = 1 \ . \tag{2.21}$$

This uncertainty relation can be rewritten with the help of the covariance matrix. Indeed, defining

$$J = \begin{pmatrix} 0 & 1 \\ -1 & 0 \end{pmatrix}$$

one can show that the uncertainty relation in Eq. (2.21) is equivalent to the inequality

$$\gamma + \mathrm{i}J \geq 0 \ . \tag{2.22}$$

We will use this inequality to distinguish between so-called entangled and separable quantum states (see Section 2.3.2).

More generally, one can formulate such uncertainty relations for any two orthogonal quadrature operators: If $\hat{X}(\vartheta)$ denotes the generic quadrature operator

from Eq. (2.15), we can first compute

$$[\hat{X}(\vartheta), \hat{X}(\vartheta + \frac{\pi}{2})] = [\hat{X}, \hat{P}] = 2\mathrm{i}$$

to find the uncertainty relation

$$\mathrm{Var}(\hat{X}(\vartheta))\mathrm{Var}(\hat{X}(\vartheta + \frac{\pi}{2})) \geq 1 \tag{2.23}$$

in complete analogy to Eq. (2.21).

2.2.4 Gaussian quantum states

Let us now introduce a special class of quantum states, called *Gaussian states*, which includes e.g. the vacuum state, coherent states and thermal states and all of them play an essential role for the remainder of this thesis. The defining property of a Gaussian state is that its Wigner function corresponds to a Gaussian function. More concretely, a Gaussian function is a function $f : \mathbb{R} \to \mathbb{R}$ of the form

$$f(x) = \frac{1}{\sqrt{2\pi V}} \exp\left(-\frac{1}{2}\frac{(x - \bar{x})^2}{V}\right), \tag{2.24}$$

where $\bar{x} \in \mathbb{R}$ and $V \in \mathbb{R}$. One can show that $\bar{x}$ corresponds to the mean value of the function f, whereas V is the variance of f. Gaussian distributions as in Eq. (2.24) are hence completely described by the first and the second moment.

The Wigner function of a Gaussian state is then given by [7]

$$W(\boldsymbol{x}) = \frac{1}{2\pi\sqrt{\det\gamma}} \exp\left\{-\frac{1}{2}(\boldsymbol{x} - \bar{\boldsymbol{x}})\gamma^{-1}(\boldsymbol{x} - \bar{\boldsymbol{x}})^T\right\}, \tag{2.25}$$

where γ is the covariance matrix from Eq. (2.20) and where we introduce the following notation: We call

$$\boldsymbol{x} = (\hat{X}, \hat{P})^T \tag{2.26}$$

the *state vector* and

$$\bar{\boldsymbol{x}} = (\langle\hat{X}\rangle, \langle\hat{P}\rangle)^T$$

the *displacement vector*. The fact that the Wigner function of a Gaussian state is Gaussian implies that such states are completely specified by the first two moments. Let us now present some important classes of Gaussian states which were frequently used in this thesis.

Vacuum state

The vacuum state is a state that contains no photons. Although the expectation value is zero for any generic quadrature (see Eq. (2.15)) [7]

$$\langle 0|\hat{X}(\vartheta)|0\rangle = 0 \ , \bar{\boldsymbol{x}} = \begin{pmatrix} 0 \\ 0 \end{pmatrix} \ , \tag{2.27}$$

the variance is non-zero

$$\text{Var}(\hat{X}(\vartheta)) = 1 \ , \gamma = \begin{pmatrix} 1 & 0 \\ 0 & 1 \end{pmatrix} \ . \tag{2.28}$$

The variance is the same in all quadratures and equal to 1. Hence, the vacuum state minimizes the uncertainty relation in Eq. (2.21). Intuitively, one may think that the vacuum state therefore possesses the smallest amount of noise possible, which even exists without the presence of photons. However, we will see shortly that it is possible to go below this amount of noise, also known as "shot noise", at least in one quadrature as long as the noise in the orthogonal quadrature increases as required by the uncertainty relation Eq. (2.21).

The Wigner function $W_0(X,P)$ of a vacuum state is given by [54]

$$W_0(X,P) = \frac{1}{2\pi} \exp\left(-\frac{X^2}{2} - \frac{P^2}{2}\right) \tag{2.29}$$

and a visualization for the Wigner function of a vacuum state is shown in figure 2.1.

It is common to quantify the amount of noise of all other states *relative to the noise of the vacuum state*. The variance is then written in units of so-called decibel via

$$\text{Var}_{\text{dB}}(X) = 10\log_{10}\left(\frac{V_X}{V_{\text{vac}}}\right) \ .$$

The vacuum variance thus corresponds to $0\,\text{dB}$, states with a higher variance yield positive dB values while states with smaller variances are given by negative values.

Thermal state

A *thermal state* with average photon number $\bar{n} \in \mathbb{R}$ is defined as a state with density matrix [55]

$$\hat{\rho}^{th}(\bar{n}) = \sum_{n=0}^{\infty} \frac{\bar{n}^n}{(\bar{n}+1)^{n+1}} |n\rangle\langle n| \ .$$

(a) vacuum state

(b) thermal state

Figure 2.1: Wigner representation of a vacuum state (a) and a thermal state (b). The probability distributions of the amplitude quadrature $\hat{X}$ and of the phase quadrature $\hat{P}$ are given by the black graphs. (a) The vacuum state yields a Gaussian distribution with a variance of 1 for both quadratures. (b) The probability distributions of the thermal state have equal but larger variances than the probability distributions of a vacuum state. For comparison the probability distributions of a vacuum state are marked by the red curves.

The Wigner function of such a state can be shown to be given by

$$W_{\mathrm{th}}(X,P) = \frac{1}{2\pi(2\bar{n}+1)} \exp\left(-\frac{X^2}{2(2\bar{n}+1)} - \frac{P^2}{2(2\bar{n}+1)} \right) \, ,$$

as depicted in Figure 2.1. Hence, any thermal state is Gaussian and its first and second moment are given by [7]

$$\bar{\boldsymbol{x}} = \begin{pmatrix} 0 \\ 0 \end{pmatrix} \quad , \quad \gamma = \begin{pmatrix} 2\bar{n}+1 & 0 \\ 0 & 2\bar{n}+1 \end{pmatrix} \, . \tag{2.30}$$

From this it is clear that the variances in both amplitude and phase quadrature are the same, but also larger than 1 if $\bar{n} \neq 0$. A thermal state with $\bar{n} = 0$ simply corresponds to the vacuum state $|0\rangle$ in Section 2.2.4. Thermal states do not minimize the uncertainty relation Eq. (2.21). The shape of the Wigner function looks very similar to that of a vacuum state, but is, roughly speaking, symmetrically broadened with the average number $\bar{n}$ of photons.

Coherent state

Coherent states are another group of Gaussian states and are typically used to describe the light prepared by a laser. These states are therefore essential for the content of this thesis.

A state $|\alpha\rangle$ is called a *coherent state* [56] if it is an eigenstate of the annihilation operator $\hat{a}$, i.e.

$$\hat{a}|\alpha\rangle = \alpha|\alpha\rangle \ , \qquad \alpha \in \mathbb{C} \ .$$

Any coherent state can be created by applying the so-called *displacement operator* $\hat{D}(\alpha)$ defined by

$$\hat{D}(\alpha) := \exp(\alpha\hat{a}^\dagger - \alpha^*\hat{a}) \tag{2.31}$$

on a vacuum state $|0\rangle$, i.e. $|\alpha\rangle = \hat{D}(\alpha)|0\rangle$. The number α is called the *complex amplitude* of the corresponding coherent state $|\alpha\rangle$ and can be expressed as $\alpha = (X_\alpha + \mathrm{i}P_\alpha)/2$ with $X_\alpha = \langle\alpha|\hat{X}|\alpha\rangle$ and $P_\alpha = \langle\alpha|\hat{P}|\alpha\rangle$.

The displacement vector and covariance matrix of the coherent states are given by [7]

$$\bar{\boldsymbol{x}} = \begin{pmatrix} X_\alpha \\ P_\alpha \end{pmatrix} \quad , \quad \gamma = \begin{pmatrix} 1 & 0 \\ 0 & 1 \end{pmatrix} \ . \tag{2.32}$$

The mean value of the numbers of photons in a coherent state is given by

$$\langle\alpha|\hat{n}|\alpha\rangle = \langle\alpha|\hat{a}^\dagger\hat{a}|\alpha\rangle = \alpha^*\alpha = |\alpha|^2 \ .$$

The Wigner function of a coherent state $|\alpha\rangle$ is again Gaussian as it is given by [54]

$$W_\alpha(X,P) = \frac{1}{2\pi} \exp\left(-\frac{(X - X_\alpha)^2}{2} - \frac{(P - P_\alpha)^2}{2} \right) \ , \tag{2.33}$$

which can be seen as a displacement of the vacuum Wigner function by $|\alpha|$. The Wigner representation of a coherent state is visualized in Fig. 2.2.

Squeezed state

All Gaussian states presented so far possess the same variance in all quadratures. This is however not a necessarily the case. So-called *squeezed states* can have different variances in orthogonal quadratures. Moreover, for certain quadratures $\hat{X}(\vartheta)$ the variance $\mathrm{Var}(\hat{X}(\vartheta))$ can even be below the shot noise value of 1. The variance in the orthogonal quadrature $\hat{X}(\vartheta + \pi)$ is then necessarily increased so that the uncertainty relation Eq. (2.23) is still satisfied. Squeezed states have a Gaussian Wigner function, however the variance of the marginal distributions depends on the considered quadrature. These properties also explain the name of these states: The Wigner function appears to be squeezed when compared to the

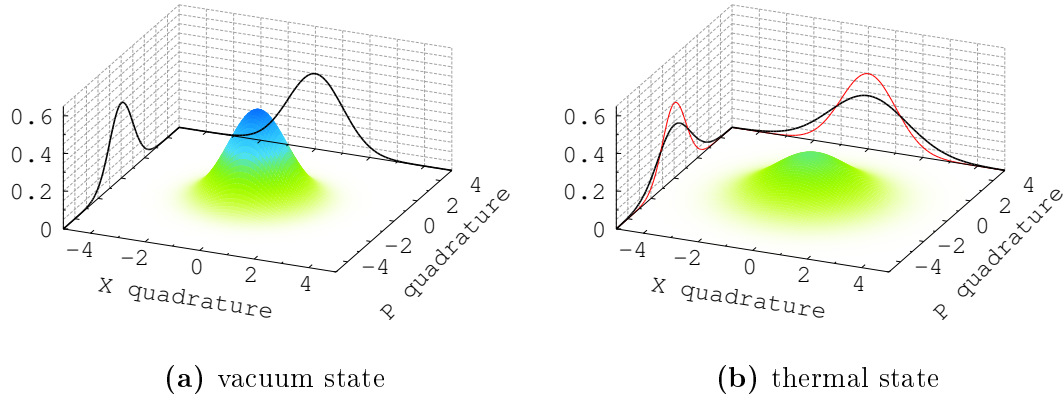**(a)** Coherent state   **(b)** Squeezed state
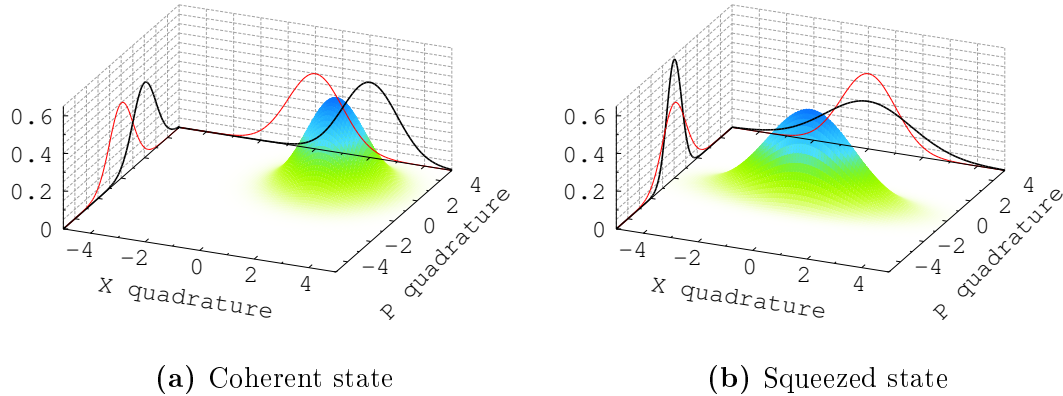
Figure 2.2: Wigner representation of a coherent state (a) and a squeezed state (b). The probability distributions of the amplitude quadrature $\hat{X}$ and of the phase quadrature $\hat{P}$ are given by the black graphs. (a): The Wigner representation of a coherent state with $\bar{\boldsymbol{x}} = (2,2)^T$. The variances of the probability distributions are identical to those of the vacuum state (red graphs). (b): The Wigner representation of a phase squeezed vacuum state with $V_{\text{sq}} = 0.4$. The probability distribution of the phase quadrature has smaller variance in comparison to the probability distribution of a vacuum state. As well is the probability distribution of the amplitude quadrature broadened in comparison to those of a vacuum state.

symmetric Wigner function of, say, a vacuum state, as is shown in figure 2.2.

Mathematically, a squeezed state is defined via the so-called *squeezing operator* [55]

$$\hat{S}(\zeta) = \exp\left(\frac{1}{2}(\zeta\hat{a}^{\dagger 2} - \zeta^*\hat{a}^2)\right) . \tag{2.34}$$

Acting with this operator on a vacuum state $|0\rangle$, generates so-called squeezed vacuum $\hat{S}(\zeta)|0\rangle$. Similarly, the generation of a squeezed coherent state or a squeezed thermal state is possible. The parameter ζ in the squeezing operator is a complex number and can therefore always be written as

$$\zeta = re^{-\mathrm{i}\phi} \ , \ r \in \mathbb{R}^+ \ . \tag{2.35}$$

Here, r is called the *squeezing parameter* which determines the "strength" of the squeezing and ϕ is the angle that defines which quadrature is squeezed. For $\phi = 0$ we get a state with reduced variance in the amplitude quadrature, a so-called *amplitude squeezed state*. The phase quadrature, whose variance is larger than the shot noise limit of 1, is then said to be *anti-squeezed*. Analogously, choosing

$\phi = \pi/2$ results in a *phase* squeezed state. In the following we denote the variance of the squeezed quadrature by V_{sq} and the variance of the anti-squeezed quadrature by V_{anti}.

The first two moments for an amplitude squeezed vacuum state are given by

$$\bar{\boldsymbol{x}} = \begin{pmatrix} 0 \\ 0 \end{pmatrix} \quad , \quad \gamma = \begin{pmatrix} e^{-2r} & 0 \\ 0 & e^{2r} \end{pmatrix} = \begin{pmatrix} V_{\text{sq}} & 0 \\ 0 & V_{\text{anti}} \end{pmatrix} \; . \tag{2.36}$$

The Wigner function of this squeezed state is then given by

$$W_r(X,P) = \frac{1}{2\pi \sqrt{V_{\text{sq}} V_{\text{anti}}}} \exp\left(-\frac{X^2}{2V_{\text{sq}}} - \frac{P^2}{2V_{\text{anti}}} \right) \; . \tag{2.37}$$

2.2.5 The Q-function

Let us introduce another phase space representation of quantum states, the so-called *Q-function*. This phase space representation is important since it corresponds to what is typically directly measured in the laboratory by a so-called eight-port homodyne detector (see Section 3.2.3). We did not introduce this representation directly after the other representations, i.e. the density matrix formalism (see Section 2.1.1), the Wigner function (see Section 2.2.2), and the covariance matrix (see Section 2.2.3), because the definition of the Q-function requires the notion of vacuum and coherent states which we just introduced in the previous section.

Given a quantum state with Wigner function $W(X,P)$, the *Q-function* $Q(X,P)$ is defined via the convolution of the Wigner function $W(X,P)$ with the vacuum distribution $W_0(X,P)$ from Eq. (2.29) [54], i.e.

$$Q(X,P) = \int \int W(X',P') W_0(X - X', P - P') dX' dP'$$

$$= \frac{1}{2\pi} \int \int W(X',P') \exp\left(-\frac{(X - X')^2}{2} - \frac{(P - P')^2}{2} \right) dX' dP' \; .$$

By comparison with the Wigner function $W_\alpha(X,P)$ of a coherent state $|\alpha\rangle$ (see Eq. (2.33)), the Q-function of a state with density matrix $\hat{\rho}$ can be rewritten as

$$Q(X,P) = \int \int W(X',P') W_\alpha(X',P') dX' dP'$$

$$= \frac{1}{2\pi} \text{tr}[\hat{\rho}|\alpha\rangle\langle\alpha|]$$

$$= \frac{1}{2\pi} \langle\alpha|\hat{\rho}|\alpha\rangle \; .$$

Here we employed the overlap formula Eq. (2.19) in the second step and denote as usual with X and P the real and imaginary part of α, respectively. Roughly speaking, the Q-function therefore corresponds to a "projection" of the state $\hat{\rho}$ onto the coherent state $|\alpha\rangle$.

2.2.6 Extension from single-mode to multi-mode states

All of the notions presented so far apply for the case where we consider only a single mode, i.e. a single bosonic system. However, consider the situation where several light fields (e.g. with different intensity and/or frequency) are superposed on a beam splitter. Our current formulation is only capable of describing one of these light fields. Fortunately, the extension of our current description to multi-mode fields is straightforward: As usual for quantum mechanics, the Hilbert space of two bosonic systems is given by the tensor product of the individual Hilbert spaces of the single bosonic systems. This means that the state space of the two light fields is simply given by $F(\mathcal{H}) \otimes F(\mathcal{H})$.

In the following we will denote different physical systems by either capital letters such as A, B, ..., or by natural numbers.

Quantum states of a two mode field with modes A and B are described by density matrices on the space $F(\mathcal{H}) \otimes F(\mathcal{H})$. The covariance matrix γ of the two mode field is then simply given by

$$\gamma = \begin{pmatrix} \mathrm{Var}(\hat{X}_A) & \mathrm{Cov}(\hat{X}_A,\hat{P}_A) & \mathrm{Cov}(\hat{X}_A,\hat{X}_B) & \mathrm{Cov}(\hat{X}_A,\hat{P}_B) \\ \mathrm{Cov}(\hat{X}_A,\hat{P}_A) & \mathrm{Var}(\hat{P}_A) & \mathrm{Cov}(\hat{P}_A,\hat{X}_B) & \mathrm{Cov}(\hat{P}_A,\hat{P}_B) \\ \mathrm{Cov}(\hat{X}_A,\hat{X}_B) & \mathrm{Cov}(\hat{P}_A,\hat{X}_B) & \mathrm{Var}(\hat{X}_B) & \mathrm{Cov}(\hat{X}_B,\hat{P}_B) \\ \mathrm{Cov}(\hat{X}_A,\hat{P}_B) & \mathrm{Cov}(\hat{P}_A,\hat{P}_B) & \mathrm{Cov}(\hat{X}_B,\hat{P}_B) & \mathrm{Var}(\hat{P}_B) \end{pmatrix} , \quad (2.38)$$

which is the straightforward extension of the covariance matrix for one mode as given in Eq. (2.20). Indeed, the 2×2 matrices in the upper left and bottom right directly correspond to the single mode covariance matrices of mode A and B, respectively.

We already mentioned that the covariance quantifies correlations between two random variables like for example the measurements of amplitude and phase quadrature on a single mode. For multi-mode systems the covariance matrix also captures correlations between quadrature measurements of *different* modes via the 2×2 matrices in the upper right and bottom left of γ. For example, the quantity $\mathrm{Cov}(\hat{X}_A,\hat{P}_B)$ quantifies the correlations between an $\hat{X}$ measurement on mode A and a $\hat{P}$ measurement on mode B.

By construction, measurements on *different* modes commute with one another, i.e. for example $[\hat{X}_A,\hat{P}_B] = 0$. Employing the state vector notation from Eq. (2.26)

this can be more generally expressed via [7]

$$[\boldsymbol{x}_i, \boldsymbol{x}_j] = 2\mathrm{i}\Omega_{ij}\,, \qquad i,j = 1,...,2N\,, \tag{2.39}$$

where N is the total number of modes such that e.g. $\boldsymbol{x}_1 = \hat{X}_A$, $\boldsymbol{x}_2 = \hat{P}_A$ and so on and so forth. The quantity Ω in Eq. (2.39) is the so-called *symplectic form* and is defined via [7]

$$\Omega = \bigoplus_{i=1}^{N} J\,, \quad J = \begin{pmatrix} 0 & 1 \\ -1 & 0 \end{pmatrix}\,.$$

Using this notation the extension of the uncertainty relation from Eq. (2.22) for a single mode to N modes is given by [7]

$$\gamma + \mathrm{i}\Omega \geq 0\,. \tag{2.40}$$

2.2.7 Gaussian channels

We have seen that several important states, which are typically prepared in a quantum optics experiment, belong to the class of Gaussian states. As discussed in Section 2.1.2, such states are typically affected by optical components before being detected. We also argued in Section 2.1.2 why such components are most generally modeled by so-called quantum channels. Here, we consider a specific subclass of such channels. A channel in this subclass has the defining property that it always outputs a Gaussian state if the input state was Gaussian as well. Such a channel therefore preserves the Gaussianity of the quantum state and is hence called a *Gaussian channel* [7]. A specific type of Gaussian channels which are of particular importance are the so-called *Gaussian unitaries*. These are Gaussian channels which transform a density matrix $\hat{\rho}$ unitarily, i.e. the state after the channel is given as $\hat{\rho}' = U\hat{\rho}U^{\dagger}$ for some unitary U.

One can show that a Gaussian unitary acts on the level of covariance matrices as a so-called *symplectic transformation*. A symplectic transformation S is a transformation that leaves the commutation relation Eq. (2.39) invariant, i.e. $S\Omega S^T = \Omega$. A Gaussian unitary then transforms a Gaussian state, described by the displacement vector $\bar{\boldsymbol{x}}$ and the covariance matrix γ, into a Gaussian state with displacement vector

$$\bar{\boldsymbol{x}}' = S\bar{\boldsymbol{x}} + \boldsymbol{d}$$

and covariance matrix

$$\gamma' = S\gamma S^T\,.$$

Here, $\boldsymbol{d}$ is a vector of length $2N$ just as the displacement vector $\bar{\boldsymbol{x}}$.

We have already seen two operations that correspond to Gaussian unitaries, namely the displacement operator $\hat{D}$ from Eq. (2.31) and the squeezing operator

$\hat{S}$ from Eq. (2.34). For the displacement operator $\hat{D}$, for example, we find the following quantities S and d: We know from Section 2.2.4 that the displacement operator can be used to create a coherent state $|\alpha\rangle$ from a vacuum state $|0\rangle$, i.e. $|\alpha\rangle = \hat{D}(\alpha)|0\rangle$, therefore it transforms Gaussian states into Gaussian states. By comparing the displacement vector $\bar{\boldsymbol{x}}$ from Eq. (2.27) and the covariance matrix γ from Eq. (2.28) for the vacuum state $|0\rangle$ with the corresponding quantities from Eq. (2.32) for a coherent state $|\alpha\rangle$ we obtain

$$\boldsymbol{d} = \begin{pmatrix} X_\alpha \\ P_\alpha \end{pmatrix} \ , \quad S = \begin{pmatrix} 1 & 0 \\ 0 & 1 \end{pmatrix} \ .$$

We will exemplify other important Gaussian unitaries together with the corresponding symplectic transformation S in the following. Before coming to that however, let us quickly state another relevant property of symplectic transformations.

According to Williamson's theorem [57] there exists, for every covariance matrix γ, a specific symplectic transformation S_γ which diagonalizes the covariance matrix, i.e.

$$S_\gamma \gamma S_\gamma^T = \bigoplus_{i=1}^{N} s_i \mathbb{1}_2 \ , \tag{2.41}$$

where $\mathbb{1}_2$ denotes the 2x2 identity matrix and s_i are the so-called *symplectic eigenvalues* of γ. The diagonalized matrix $S_\gamma \gamma S_\gamma^T$ is called the Williamson form of the covariance matrix γ [7].

As symplectic transformations transform between covariance matrices, the Williamson form Eq. (2.41) is also a covariance matrix. Moreover, if we compare its form with Eq. (2.30), we see that $S_\gamma \gamma S_\gamma^T$ corresponds to the covariance matrix of a multi mode system where each system is in a thermal state with mean photon number $\bar{n} = \frac{s_i - 1}{2}$. This observation leads to the following physical interpretation of Williamson's theorem: Think of a light field in an actual quantum optical experiment. Suppose the Gaussian state of the light field at some instance of time is described by the covariance matrix γ in Eq. (2.41). Then S_γ can be interpreted as the collection of all effects that acted on the light field in the past. The intuition is that the physical system of the light field was initially in a thermal state described by the Williamson form of γ, before it was manipulated by the optical devices in the laboratory. For example, the laser can be thought of as a device which applied some symplectic transformation on this thermal state to change it into a coherent state. The squeezing device then applied some symplectic transformation and changed the coherent state into a squeezed state. Similarly, all optical components can be thought of as symplectic transformations on the

state of the light field and all these transformations are jointly described by the single symplectic transformation S_γ.

The fact that $S_\gamma \gamma S_\gamma^T$ is again a covariance matrix also implies that the uncertainty relation in Eq. (2.40) applies. More concretely, consider the symplectic eigenvalues s_i of γ, which can be obtained by computing the eigenvalues of the matrix $i\Omega\gamma$, i.e.

$$\{s_i\}_{i=1}^N = |\text{eig}\{i\Omega\gamma\}| \ .$$

The uncertainty relation in Eq. (2.40) can then be written as

$$\min\{s_i\} \geq 1 \ .$$

This will be our final form of the uncertainty relation, which we employ later in this thesis. Due to its simple structure (we only need to compute the eigenvalues of a finite-dimensional matrix and check whether these eigenvalues are greater than or equal to 1), it is not difficult to use this uncertainty relation to check for "physicality" of a quantum state.

Let us now provide some important examples of Gaussian channels.

Phase shift

The phase is a typical property of a wave and is only reasonably defined if a reference is provided. A *phase shift* is a rotation of the state in phase space by the angle θ with respect to this reference system and can be described by the symplectic transformation [7]

$$d = \begin{pmatrix} 0 \\ 0 \end{pmatrix} \ , \quad S_{\text{rot}}(\theta) = \begin{pmatrix} \cos(\theta) & \sin(\theta) \\ -\sin(\theta) & \cos(\theta) \end{pmatrix} \ . \tag{2.42}$$

The rotation changes as well the Wigner function and causes a mixture between the quadratures, resulting in

$$W_{\text{rot}}(X, P, \theta) = W(X\cos\theta + P\sin\theta, -X\sin\theta + P\cos\theta) = W(X_\theta, P_\theta) \ . \tag{2.43}$$

The two expressions for W_{rot} can here seen as different interpretations of the rotation. The first term express the rotated Wigner function in the original quadrature axes X and P, revealing how the terms get mixed. The second expression gives the Wigner function in terms of two rotated axes, namely X_θ and P_θ. Regarding the rotated axes, the rotated Wigner function W_{rot} is given in the same form as the initial Wigner function W. For example the Wigner function of a rotated squeezed state, i.e. Eq. (2.37), is given by

$$W_{\text{rot,r}}(X_\theta, P_\theta) = \frac{1}{2\pi\sqrt{V_{\text{sq}}V_{\text{anti}}}} \exp\left(-\frac{X_\theta^2}{2V_{\text{sq}}} - \frac{P_\theta^2}{2V_{\text{anti}}}\right) \ .$$

A phase shift is a Gaussian operation, however we will see in Section 2.4.2 that so called phase noise, which is a statistical average of phase shifts applied to the state, can degaussify the state.

Beam splitter

The beam splitter is one of the most important passive components in quantum optics. On this device, two incident beams interfere and create two output beams. The splitting is defined by the power transmissivity $t \in [0,1]$ of the beam splitter. However, for a shorter notation, we will write the beam splitter with the amplitude transmissivity $\tau = \sqrt{t}$. For a lossless beam splitter, the amplitude reflectivity is then given by $\varrho = \sqrt{1-t}$ and τ and ϱ suffice

$$\varrho^2 + \tau^2 = 1 \; .$$

The beam splitter is described by the symplectic transformation

$$S_{\mathrm{BS}}(t) := \begin{pmatrix} \tau & 0 & -\varrho & 0 \\ 0 & \tau & 0 & -\varrho \\ \varrho & 0 & \tau & 0 \\ 0 & \varrho & 0 & \tau \end{pmatrix} \; . \tag{2.44}$$

It is important to be aware of the fact, that it is not sufficient to regard only one input port of the beam splitter. A beam splitter is always a four-port object consisting two inputs and two outputs. Even if the signal is just split with a beam splitter, a vacuum mode couples in the other input port and generates a mixed state at the output ports.

The state vector of two arbitrary input states $\xi_{\mathrm{in,A}}$ and $\xi_{\mathrm{in,B}}$ is therefore transformed according to

$$\begin{pmatrix} X_{\mathrm{out,A}} \\ P_{\mathrm{out,A}} \\ X_{\mathrm{out,B}} \\ P_{\mathrm{out,B}} \end{pmatrix} = S_{\mathrm{BS}} \begin{pmatrix} X_{\mathrm{in,A}} \\ P_{\mathrm{in,A}} \\ X_{\mathrm{in,B}} \\ P_{\mathrm{in,B}} \end{pmatrix} = \begin{pmatrix} \tau X_{\mathrm{in,A}} - \varrho X_{\mathrm{in,B}} \\ \tau P_{\mathrm{in,A}} - \varrho P_{\mathrm{in,B}} \\ \varrho X_{\mathrm{in,A}} + \tau X_{\mathrm{in,B}} \\ \varrho P_{\mathrm{in,A}} + \tau P_{\mathrm{in,B}} \end{pmatrix} \; .$$

The Wigner function changes in the same way, given by

$$W_{\mathrm{out}}(X_{\mathrm{in,1}}, P_{\mathrm{in,1}}, X_{\mathrm{in,2}}, P_{\mathrm{in,2}}) = W_{\mathrm{in}}(X_{\mathrm{out,1}}, P_{\mathrm{out,1}}, X_{\mathrm{out,2}}, P_{\mathrm{out,2}}) \; .$$

2.3 Entangled states of light

The existence of entanglement is one of the most important features of quantum mechanics and is a central part of many quantum information protocols [5–12]. Generally, the state of a two-mode system is said to be separable, if the density matrix $\hat{\rho}_{AB}$ can be written as convex combination of product states, [58]

$$\hat{\rho}_{AB} = \sum_i p_i \hat{\rho}_i^A \otimes \hat{\rho}_i^B \ . \tag{2.45}$$

A system, which cannot be described by Eq. (2.45) is called entangled.

In this thesis, the terms "entangled states" or "entanglement" will always refer to so-called *two-mode-squeezed vacuum states*. The name originates from the generation process, where two squeezed vacuum states are overlapped on a balanced beam splitter [11, 12]. Due to the fact, that both the input states as well as the beam splitter operation is Gaussian, it is clear that a two-mode-squeezed state is as well a Gaussian state. Therefore, the entanglement criteria, which we will present in the following, are formulated for the covariance matrix of the two-mode state. Applying the same criteria on states which are not Gaussian will not properly clarify whether the state is entangled or not. In such cases entanglement can sometimes only be present in the higher order moments.

In this section, we will first present a method to prepare two-mode entangled states and discuss their representation via the covariance matrix. Then an entanglement criterion is presented which can witness the presence of Gaussian entanglement.

2.3.1 Preparation of two-mode-squeezed states

Two-mode-squeezed states are generated by superimposing two squeezed light fields, denoted by A and B, on a beam splitter. The state vector $\boldsymbol{x}$, Eq. (2.26), of the input two-mode state reads

$$\boldsymbol{x} = (\hat{X}_{A,in}, \hat{P}_{A,in}, \hat{X}_{B,in}, \hat{P}_{B,in})^T \ .$$

The covariance matrix of the input state is given by

$$\gamma = \begin{pmatrix} \gamma_A & 0 \\ 0 & \gamma_B \end{pmatrix} = \begin{pmatrix} e^{2r} & 0 & 0 & 0 \\ 0 & e^{-2r} & 0 & 0 \\ 0 & 0 & e^{-2s} & 0 \\ 0 & 0 & 0 & e^{2s} \end{pmatrix} \ ,$$

where mode A is phase squeezed with the squeezing parameter r and mode B is amplitude squeezed with the squeezing parameter s. Interfering these modes on a
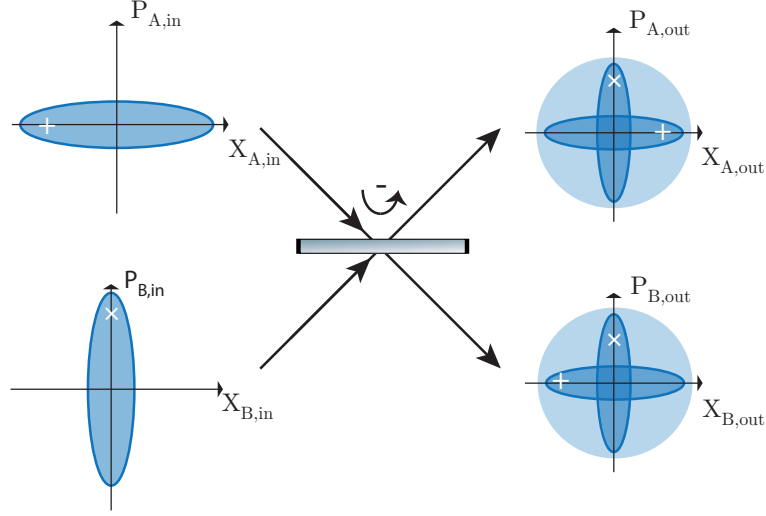
Figure 2.3: Generation of two-mode-squeezed states. The blue shaded ellipses symbolize the squeezed states by their variances. The output ports of the beam splitter present the two-mode-squeezed state and are entangled. Regarded separately, each mode of the entangled state is in a thermal state, indicated by the blue shaded circle. However, the modes show correlations and anti-correlations, indicated with the white plus and cross [60].

balanced beam splitter, i.e. a beam splitter with $t = 0.5$ (c.f. Eq. (2.44)), leads to

$$\boldsymbol{x}' = S_{\mathrm{BS}}(0.5)\boldsymbol{\xi} = \begin{pmatrix} \frac{1}{\sqrt{2}}(\hat{X}_{\mathrm{A,in}} - \hat{X}_{\mathrm{B,in}}) \\ \frac{1}{\sqrt{2}}(\hat{P}_{\mathrm{A,in}} - \hat{P}_{\mathrm{B,in}}) \\ \frac{1}{\sqrt{2}}(\hat{X}_{\mathrm{A,in}} + \hat{X}_{\mathrm{B,in}}) \\ \frac{1}{\sqrt{2}}(\hat{P}_{\mathrm{A,in}} + \hat{P}_{\mathrm{B,in}}) \end{pmatrix}$$

and the covariance matrix changes according to

$$\begin{aligned} \gamma' = \gamma_{AB} &= S_{\mathrm{BS}}(0.5)\,\gamma'\,S_{\mathrm{BS}}(0.5)^T \\ &= \begin{pmatrix} \frac{1}{2}(\mathrm{e}^{2r} + \mathrm{e}^{-2s}) & 0 & \frac{1}{2}(\mathrm{e}^{2r} - \mathrm{e}^{-2s}) & 0 \\ 0 & \frac{1}{2}(\mathrm{e}^{-2r} + \mathrm{e}^{2s}) & 0 & \frac{1}{2}(\mathrm{e}^{-2r} - \mathrm{e}^{2s}) \\ \frac{1}{2}(\mathrm{e}^{2r} - \mathrm{e}^{-2s}) & 0 & \frac{1}{2}(\mathrm{e}^{2r} + \mathrm{e}^{-2s}) & 0 \\ 0 & \frac{1}{2}(\mathrm{e}^{-2r} - \mathrm{e}^{2s}) & 0 & \frac{1}{2}(\mathrm{e}^{-2r} + \mathrm{e}^{2s}) \end{pmatrix} . \end{aligned} \quad (2.46)$$

We have chosen orthogonal squeezed quadratures and a balanced beam splitter for simplicity, but any squeezed input states (as long as they are not orientated along the exact same direction) and any value of t for the beam splitter will result in a two-mode-squeezed state. It is also possible to set one squeezing parameter to zero and interfere a squeezed state with vacuum, thereby creating so-called *v-class*

entanglement [59]. The generation of two-mode-squeezed states is depicted in Fig. 2.3.

If the squeezing parameters r and s of the input states are chosen to be the same, the covariance matrix simplifies to

$$\gamma_{AB} = \begin{pmatrix} a & 0 & b & 0 \\ 0 & a & 0 & -b \\ b & 0 & a & 0 \\ 0 & -b & 0 & a \end{pmatrix} , \qquad (2.47)$$

with $a = \cosh(2r)$ and $b = \sinh(2r)$. Taking only into account the covariance matrix of one mode, each state by itself appears to be in a thermal state, see Eq. (2.30), with a mean photon number $\bar{n}$ of

$$\bar{n} = \frac{\cosh(2r) - 1}{2} .$$

Entanglement can be seen in the covariance matrix γ_{AB} from the correlation terms between the modes: if $b > 0$ then there exist correlations between the amplitude quadratures and anti-correlations between the phase quadratures of the modes A and B and we know that A and B are entangled.
However, in typical experiments two-mode-squeezed states do not have this idealized shape. Asymmetries of the squeezing parameters require us to work with the lengthy expression from Eq. (2.46) instead of the simple expression with the parameters a and b from Eq. (2.47). Also, if the squeezing ellipses are not orientated along the amplitude and phase quadrature axis in phase space, the covariance terms $\mathrm{Cov}(\hat{X}_i \hat{P}_i)$ become non-zero as the probability distributions of amplitude and phase quadrature are partly correlated or anti-correlated.

2.3.2 Entanglement witnesses

An entanglement witness is a certain computable value which can be used to certify if a state is entangled. This means that if the value is, say, below a certain threshold, then we can be sure that the corresponding state is entangled.

There exist various different entanglement witnesses, each suitable for different situations. Here, we present two such witnesses, namely one based on the so-called *PPT criterion* and one based on the squeezing variance V_{sq}.

PPT criterion

For bipartite systems, the PPT criterion is a sufficient criterion to detect entanglement; for Gaussian states it is even necessary [61]. The term "PPT" is an

acronym for *positive partial transpose*. Originally, the criterion was formulated by A. Peres and P. Horodecki [62], [63] for density matrices and uses the separability condition of Eq. (2.45). The idea behind the criterion is the following: If a state is separable, then the density matrix of the partially transposed state, given by

$$\hat{\rho}_{AB}^{T_A} = \sum_i p_i \hat{\rho}_i^{A,T} \otimes \hat{\rho}_i^B \ ,$$

must be again a density matrix of a physical state. This implies that $\text{tr}[\hat{\rho}^{T_A}] = 1$ and that all eigenvalues must be greater or equal to zero as they provide the probabilities, see Eqs. (2.1) and (2.2). If this is not the case, the state $\hat{\rho}^{T_A}$, created by partial transposition, is not physical and therefore the state $\hat{\rho}$ is not separable. Simon transferred this to continuous-variable (CV) systems [61], using the fact that the partial transpose is equivalent to a mirror reflection of the phase quadrature in phase space, i.e.

$$\hat{\rho} \rightarrow \hat{\rho}^T \Leftrightarrow W(X,P) \rightarrow W(X,-P) \ .$$

In terms of the covariance matrix, the partial transpose is given by

$$\gamma \rightarrow \gamma^{(T_i)} := R_i \gamma R_i^T \ ,$$

where i denotes which mode is transposed and e.g. R_B is defined as

$$R_B = \begin{pmatrix} 1 & 0 & 0 & 0 \\ 0 & 1 & 0 & 0 \\ 0 & 0 & 1 & 0 \\ 0 & 0 & 0 & -1 \end{pmatrix} \ .$$

If the transposed state with $\gamma^{(T_i)}$ still describes a physical state, it must also satisfy the uncertainty relation from Eq. 2.2.7

$$\mu := \min\{|\text{eig}(i\Omega\gamma^{(T_i)}|\} \geq 1 \ . \tag{2.48}$$

If this is the case, we know that the two-mode system is separable.

Therefore, the smallest symplectic eigenvalue, denoted by μ corresponds to an entanglement witness: If $\mu < 1$, the state is entangled, whereas $\mu \geq 1$ implies separability (at least for Gaussian states).

Entanglement witness via squeezing variance

Recalling Eq. (2.47), the covariance matrix of a pure symmetric Gaussian two-mode-squeezed state is given by

$$\gamma = \begin{pmatrix} a & 0 & b & 0 \\ 0 & a & 0 & -b \\ b & 0 & a & 0 \\ 0 & -b & 0 & a \end{pmatrix}$$

with $a = \cosh(2r)$, $b = \sinh(2r)$, where r denotes the squeezing parameter of the incident squeezed light fields. The symplectic eigenvalues of such a matrix are given by $a - b$ and $a + b$, thus the smallest symplectic eigenvalue is $\mu = a - |b|$. Writing this in terms of the squeezing parameter, we get [64]

$$\mu = a - |b| = \cosh(2r) - \sinh(2r) = e^{-2r} = V_{\mathrm{sq}} \, , \qquad (2.49)$$

where we used the definition of the squeezing variance V_{sq} from Eq. (2.36). Thus for pure symmetric squeezed states, the presence of initial squeezing implies entanglement and vice versa. The squeezing variance V_{sq} therefore corresponds to an entanglement witness.

2.4 Detrimental effects for the nonclassical properties of light

The nonclassical properties of light, such as entanglement, are highly susceptible to certain effects, which are common in quantum optical experiments. Two of the main such detrimental effects, which we have to consider for the experiments presented in Chapter 5 and Chapter 6 are optical loss and decoherence effects like phase noise.

In the following we provide the theoretical description of these effects.

2.4.1 Optical loss

In quantum optical experiments, the transmission of light is always affected by optical loss which occurs if photons get lost on the way due to stray effects, absorption or imperfect alignment. Mathematically, this optical loss is described by a specific quantum channel, which we call *lossy channel* in the following. Intuitively, this channel can be understood with a model, where optical loss is represented by a virtual beam splitter in the path of the light field. We denote by ϵ the power reflectivity of the beam splitter, which corresponds to the amount of "loss" due the lossy channel. Conversely, we call $\eta = 1 - \epsilon$ the optical efficiency of the beam splitter. The open port of the beam splitter causes the light field to be mixed with vacuum with a factor of the loss ϵ. The covariance matrix of a state affected by loss ϵ is therefore given by

$$\gamma_{\eta} = \eta\gamma_{\mathrm{sig}} + (1 - \eta)\gamma_{\mathrm{vac}} \, . \qquad (2.50)$$

If we consider a two-mode state, where each mode is affected independently by lossy channels with efficiencies η_A and η_B, respectively, then Eq. (2.50) reads [64]

$$\gamma_{\mathrm{AB},\eta} = S_{\eta}\gamma_{\mathrm{AB}}S_{\eta}^{T} + G_{\eta}, \qquad (2.51)$$

(a) Lossy channel   **(b)** Noisy channel
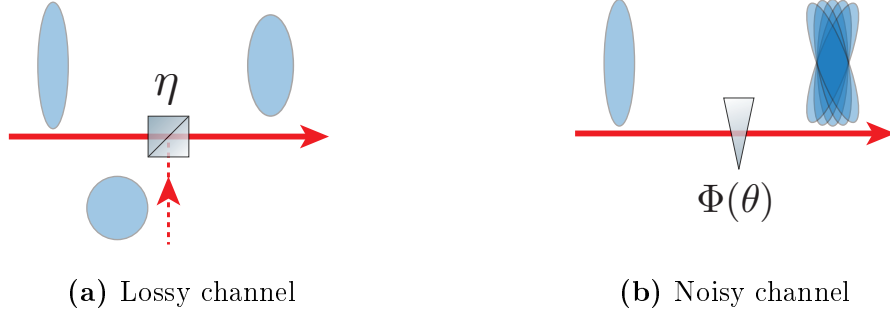
Figure 2.4: Visualization of a lossy and a noisy channel by its effect on a squeezed vacuum state. (a): The lossy channel acts like a virtual beam splitter in the path of the light field, causing an admixture of vacuum. (b): The noisy channel leads to a statistical mixture of rotated squeezed states.

where

$$
S_\eta = \begin{pmatrix} \sqrt{\eta_A} & 0 & 0 & 0 \\ 0 & \sqrt{\eta_A} & 0 & 0 \\ 0 & 0 & \sqrt{\eta_B} & 0 \\ 0 & 0 & 0 & \sqrt{\eta_B} \end{pmatrix}, \qquad G_\eta = \begin{pmatrix} 1 - \eta_A & 0 & 0 & 0 \\ 0 & 1 - \eta_A & 0 & 0 \\ 0 & 0 & 1 - \eta_B & 0 \\ 0 & 0 & 0 & 1 - \eta_B \end{pmatrix}.
$$

2.4.2 Phase noise

As introduced in Section 2.2.7, a phase shift corresponds to a Gaussian operation that causes a rotation of the state in phase space by the angle θ. The Wigner function of the rotated state is then given by $W_{\mathrm{rot}}(X,P,\theta)$ as in Eq. (2.43).

Now, consider the situation where not only a single, but *multiple* phase shifts affect our state. We assume that the distribution of angles θ of these phase shifts is most generally given by a function $\Phi(\theta)$. This situation is what we refer to as *phase noise* or a *noisy channel*.

Phase-diffused squeezed states

Let us first consider phase noise acting on a squeezed state. The phase shifts then diffuse the state and lead to a statistical mixture of the rotated squeezed states. More concretely, the Wigner function of the phase diffused state is given by [65]

$$
W_{\mathrm{PN}}(X,P) = \int W_{\mathrm{rot}}(X,P,\theta)\Phi(\theta)d\theta \ .
$$

The marginal probability distributions are affected in a similar way: For example, we can use Eq. (2.17) to find that the marginal distribution of the amplitude
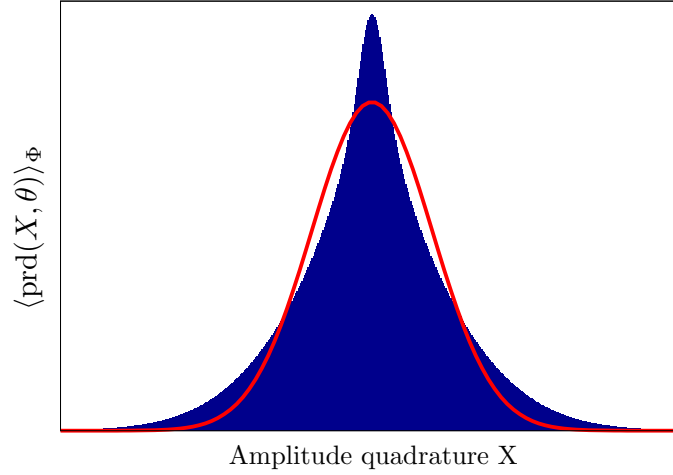
Figure 2.5: Probability distribution of a dephased amplitude squeezed state. The probability distribution prd(X,θ) is given in blue for a phase diffused amplitude squeezed state with an original squeezing variance of $V_{\mathrm{sq}} = 0.1$ without phase noise. The added phase noise yields a Gaussian distribution with a variance of $V_\phi = 0.9$ and is symmetric around zero. It is clear to see that the distribution of the phase diffused state is not longer Gaussian. For comparison, a Gaussian distribution is given by the red line.

quadrature for the phase diffused state is given by

$$
\langle \mathrm{prd}(X,\theta) \rangle_\Phi = \int W_{\mathrm{PN}}(X,P) dP
$$
$$
= \int \int W_{\mathrm{rot}}(X,P,\theta) \Phi(\theta) d\theta dP \ . \qquad (2.52)
$$

From this, it is possible to see that phase diffusion causes a degaussification of the state as shown in calculations from B. Hage and A. Franzen, i.e. [66], [67]. Indeed, assuming symmetric, Gaussian distributed phase noise, i.e.

$$
\Phi(\theta) = \frac{1}{\sqrt{2\pi V_\Phi}} e^{-\frac{\theta^2}{2 V_\Phi}}
$$

where V_Φ denotes the variance of the Gaussian distribution and can therefore be interpreted as the phase noise strength, it is possible to solve the integral in Eq. (2.52) explicitly. The resulting probability distribution of the amplitude quadrature is depicted in figure 2.5 and clearly shows the degaussification of the initial state.

Phase-diffused two-mode-squeezed vacuum states

Let us now consider a two-mode-squeezed state affected by phase noise. For this we first recall the action of a single phase shift on such a state. If both modes are rotated by the angles θ_A and θ_B respectively, then the covariance matrix is transformed according to

$$\gamma_{AB} \rightarrow R\gamma_{AB}R^T \ ,$$

with $R = S_{\mathrm{rot}}(\theta_A) \oplus S_{\mathrm{rot}}(\theta_B)$.

Phase noise now corresponds to multiple phase shifts where the angles are distributed according to some function $\Phi(\theta_A,\theta_B)$. The angles can be correlated, partially correlated or completely uncorrelated. The phase diffused state is again given by the average over these phase shifts.

For simplicity, let us first assume that the dephasing of both modes is independent and symmetric around zero. Moreover, we assume a pure and symmetric two-mode-squeezed state such that the covariance matrix before the phase noise is given as in Eq. (2.47). Then the covariance matrix of the phase diffused two-mode-squeezed vacuum state is given by [64]

$$\gamma_{\mathrm{PN}} = \langle R\gamma_{AB}R^T \rangle_\Phi = \begin{pmatrix} a & 0 & qb & 0 \\ 0 & a & 0 & -qb \\ qb & 0 & a & 0 \\ 0 & -qb & 0 & a \end{pmatrix} \tag{2.53}$$

where $\langle \ldots \rangle_\Phi$ denotes the statistical averaging over the phase shifts as in Eq. (2.52) and q denotes the dephasing parameter defined as

$$q = \langle \cos\theta_A \cos\theta_B \rangle_\Phi.$$

The dephasing parameter q can take values between 0 and 1 and is related to the strength of the phase noise, as we explain in the following. The detailed calculation to obtain Eq. (2.53) is given in the Appendix A.1, and assumes a vanishing mean value which is legitimate as only vacuum states are used throughout this thesis.

From Eq. (2.53) we see that the individual modes are not affected by the phase noise. This is plausible since they are each in a thermal state and thus rotationally invariant. However, the phase noise reduces the correlations between the modes which is seen by the suppression of b due to the dephasing parameter q. If $q = 1$, which corresponds to "no phase noise", then the covariance matrix remains unaffected as expected. However, if the strength of the phase noise is maximal, i.e. if $q = 0$, then all correlations between modes A and B are suppressed. Indeed, we will see this effect explicitly in Chapter 4.

Let us now consider the more general case, where the covariance matrix is not in the highly symmetric form of Eq. (2.47). Additionally, we also drop the assumption that the phase noise needs to be independent and symmetric. The calculation of the phase diffused covariance matrix then becomes much more involved and we find that, instead of one parameter (the dephasing parameter q from above), a set of eight parameters is needed to fully describe the dephasing of the initial state γ, namely

$$\{\langle\cos^2\theta_A\rangle_\Phi \ , \langle\cos\theta_A\sin\theta_A\rangle_\Phi \ , \langle\cos\theta_A\cos\theta_B\rangle_\Phi \ , \langle\cos\theta_A\sin\theta_B\rangle_\Phi \ ,$$
$$\langle\cos^2\theta_B\rangle_\Phi \ , \langle\cos\theta_B\sin\theta_B\rangle_\Phi \ , \langle\sin\theta_A\sin\theta_B\rangle_\Phi \ , \langle\sin\theta_A\cos\theta_B\rangle_\Phi\} \ .$$

Details on how these parameters appear in the dephased covariance matrix are shown in Appendix A.2. The experimental method to obtain these parameters is described in Section 3.3.

In the theoretical analysis of entanglement distillation, presented in Chapter 4, we will restrict ourselves to the idealized case, where the phase noise is characterized by the dephasing parameter q. Our presentation and discussion of the experimental results however is based on the completely general case, where the effect of the phase noise is characterized by the above eight parameters.

CHAPTER 3

Experimental methods

The experimental methods for generation and detection of squeezed and entangled states of light have been developed and sophisticated in the last decades [60]. Depending on the focus, the designs emerged in different directions but started all from the same basics. In this chapter, some of these basic techniques and setups are presented.

The chapter starts with an overview of the generation of squeezed states, focusing on the parts which are equal in the experiments. Detailed information on the particular devices are given in the respective chapters. The second part is a discussion about different devices for light detection. As the most important tool for detection of light in this thesis, the principle of the *balanced homodyne detector* (BHD) is discussed in detail, including techniques to stabilize on amplitude and phase quadrature measurement. Based on that, the principle of *eight-port homodyne detection* (EHD) is introduced. Then with a focus on the first experiment, the experimental realization of phase noise and the determination of the dephasing parameters out of the experimental data is explained.

3.1 Squeezed-light source

The squeezed vacuum states produced for this thesis are created by the process of degenerated optical parametric down-conversion [52]. For this process, a nonlinear medium with a second-order dielectric susceptibility $\chi^{(2)}$ is placed inside an optical cavity. A pump field with frequency 2ω, here $532\,\mathrm{nm}$, is coupled into the medium, where one photon of the pump field decays into two photons with $\omega_{\mathrm{pump}} = \omega_1 + \omega_2$.
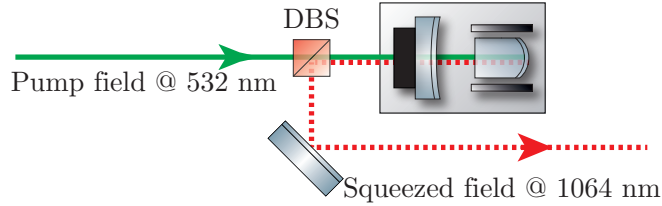
Figure 3.1: Schematic setup of a squeezed-light source: The highly reflective curved back of the nonlinear crystal forms a hemilithic cavity with the coupling mirror. The pump field enters the cavity through the mirror and the generated squeezed light field can be separated from the pump field with a dichroic beam splitter (DBS). The stabilization on the optimal phase matching temperature is realized with Peltier elements.

In the degenerate case, these created fields have identical frequencies $\omega = 1064\,\text{nm}$ and form the so-called signal field. The time-dependent Hamiltonian describing this process can be identified as the squeezing operator [52], i.e. Eq. (2.34) and the pair-wise created photons form the squeezed vacuum field.

A schematic of this setup is shown in Fig. 3.1. The curved and highly reflective end surface of the nonlinear crystal forms a standing wave cavity together with a curved mirror which is attached to a *piezoelectric transducer* (PZT). This cavity defines the spatial mode of the signal field and guarantees as well the overlap with the pump field for the nonlinear process. The hemilithic setup has proven to offer a good trade-off between low losses and flexibility. Due to the movable coupling mirror, the cavity length can be varied easily to match the resonance condition for the signal field. Using the crystal itself as a back mirror reduces the amount of surfaces which needs to be passed in the cavity as this causes additional loss for the created squeezing.

First the pump field propagates through a *dichroic beam splitter* (DBS), which transmits 532 nm and reflects 1064 nm, and couples in the cavity through the mirror. The squeezed-light field leaves the cavity through the coupling mirror, gets reflected at the DBS and is available for downstream experiments.

To ensure constructive interference of the created signal photons, pump and signal field need to propagate with the same speed which means that the beams need to be phase matched [60].

For most materials, the refractive index depends on the frequency (normal dispersion), which would make the phase matching of pump and signal field impossible. To overcome this problem, different solutions exist that are based on temperature control of the crystal. The techniques are just briefly explained here, a detailed description can be found in [68].

To control and stabilize the temperature, the crystal is placed on a copper element that is heated by a Peltier element. A resistor with negative temperature coefficient attached to the copper element serves as a temperature sensor for the control loop.

Type I phase matching   For this technique, the nonlinear crystal needs to show birefringence. These materials show different refractive indices, depending on the polarization of the optical light field. This effect can be used to compensate for the difference of the refractive indices caused by the frequency difference. The polarization of the pump field is chosen to fit the axis with lower refractive index while the polarization of the signal field is chosen to be perpendicular to the pump. As the refractive index is temperature dependent, the temperature can be optimized to achieve the same index for both light fields. This results in a perfect phase matching and the corresponding temperature is called phase matching temperature. This method is used for the squeezing source in Chapter 5.

Quasi phase matching   Another possibility is the usage of a periodically poled medium which enables the technique of *quasi phase matching*. To understand this technique, we consider first what happens in a normal medium without periodical poling. If the process starts with perfect phase matching, the phases of pump and signal field drift apart while propagating in the medium due to mismatch of the wave vectors. This reduces the efficiency of the conversion process and after some distance, namely the so-called coherence length l_c, the phases are so far apart that the process is inverted and the power gets converted back to the pump. To counteract this effect, a periodically poled medium is composed of different areas which show inverted susceptibility relative to each other and the width of these areas is chosen to match the coherence length l_c. The fields propagate through this medium but instead of the back conversion of the field after l_c, the phase mismatch is decreasing again due to the inverted susceptibility in the subsequent area. This leads to a continuous increase of the signal field. As the medium expands with temperature, this method has as well a "phase matching temperature", where the length of the sections fits exactly the coherence length and guarantees thus optimal conversion. The squeezing source in chapter 6 utilizes the method of quasi phase matching.

3.2 Detection of light

3.2.1 Detection with a single photo diode

The detection of light is usually realized with photo diodes, using the photoelectric effect. In the optimal case one photon is hitting the photosensitive area of the semiconductor and creates thereby one photo electron. With this process, the optical field is converted into an electronic signal which can be analyzed.

The standard type is a *PIN photo diode*, where the letters stand for the doping of the semiconductor material, being P(osivitely) doped, I(ntrinsic) and N(egatively) doped [54]. The created photo current is proportional to the power of the input light field. This proportionality is usually given by the responsivity in the unit A/W. A very common characteristic of photo diodes is the so-called quantum efficiency which gives the probability for a successfully created photo electron per incident photon. Photo diodes with quantum efficiencies of up to 99 % are available for the standard wavelengths in the near-infrared regime. However, PIN photo diodes are not optimal if the light field is very weak. At some point the dark current, created by the electronic noise of the detector and of the photo diode itself, covers the signal and thus limits the resolution for small intensities.

To detect even single photons, so called *avalanche photo diodes* (APD) are available. In the Geiger mode, a created photo electron is causing an avalanche which generates a distinct event or "click" at the detector [54].

The signal of an APD is not linear to the intensity of the optical light field as the same avalanche is created, regardless of the presence of one or several photons. As electrons can be created without the presence of a photon, there is as well the possibility that the detector gives a false signal. This effect is called dark clicks of the APD, analogous to the dark current of the PIN photo diodes.

APDs are used to detect single photon events of a field where the probability of several photons at the same time is low. In the continuous-variable regime, a possible application is the heralding of a single photon in a dim light field, e.g. [69, 70].

APDs do not provide a frequency resolved signal, as they do not distinguish between electrons created by photons of different frequencies. Therefore careful frequency filtering of the signal field before the APD is mandatory.

However in most cases it is not enough to detect and characterize the intensity of a light field. As shown in Chapter 2, several properties of the quantum mechanical systems are expressed in terms of the quadratures, like e.g. nonclassical noise statistics.

Since there is a significant difference between the intensity of a light field, corresponding to the photon number $\hat{n} = \hat{a}^\dagger \hat{a}$, and its field amplitude quadrature,
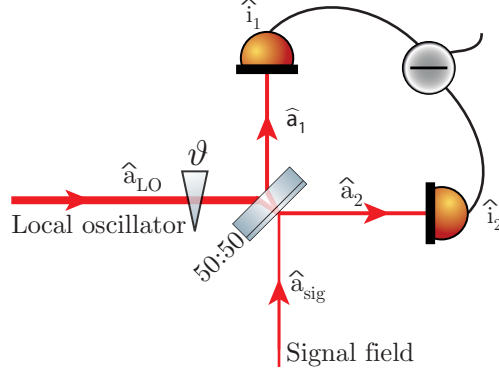
Figure 3.2: Schematic of a balanced homodyne detector: The signal field gets superimposed with a strong local oscillator on a balanced beam splitter. The two outputs are detected with photo detectors and the photo currents get subtracted. The relative phase ϑ between the two incident light fields determine the observed quadrature of the signal field.

meaning $\hat{X} = \hat{a} + \hat{a}^\dagger$ [54], there exists no simple relationship between photon statistics and quadrature distributions. Hence, individual measurement devices are needed to access one or the other. While we already presented devices to access the first, homodyne detection is the method of choice to access the quadrature distributions.

3.2.2 Homodyne detection

The method of balanced homodyne detection (BHD) can be used to access the probability distributions $\mathrm{prd}(X)$ and $\mathrm{prd}(P)$ of the quadratures, introduced in Section 2.2.2, see Eq. (2.14). The schematic setup of a homodyne detector is depicted in Fig. 3.2. For the detection, our signal field of interest, denoted by $\hat{a}_{\mathrm{sig}}$, is superimposed on a balanced beam splitter with a strong coherent field, called the *local oscillator* (**LO**). The local oscillator field has the same frequency and spatial mode form as the signal field and is given by $\hat{a}_{\mathrm{LO}}e^{\mathrm{i}\vartheta}$ where ϑ denotes the relative phase between the LO and the signal field. The vectorial form is given by

$$\hat{\boldsymbol{x}} = (\hat{a}_{\mathrm{sig}}, \hat{a}_{\mathrm{sig}}^\dagger, \hat{a}_{\mathrm{LO}}e^{\mathrm{i}\vartheta}, \hat{a}_{\mathrm{LO}}^\dagger e^{-\mathrm{i}\vartheta}) \ .$$

Note, that we assume a fixed phase relation between the two fields which is ensured by the fact, that both light fields are generated from the same laser.

After interference on the balanced BS, given by the symplectic transformation

from section 2.2.7 we obtain for the output

$$S_{\mathrm{BS}}(0.5)\hat{\boldsymbol{x}} = \begin{pmatrix} \frac{1}{\sqrt{2}}(\hat{a}_{\mathrm{sig}} - \hat{a}_{\mathrm{LO}}e^{\mathrm{i}\vartheta}) \\ \frac{1}{\sqrt{2}}(\hat{a}^\dagger_{\mathrm{sig}} - \hat{a}^\dagger_{\mathrm{LO}}e^{-\mathrm{i}\vartheta}) \\ \frac{1}{\sqrt{2}}(\hat{a}_{\mathrm{sig}} + \hat{a}_{\mathrm{LO}}e^{\mathrm{i}\vartheta}) \\ \frac{1}{\sqrt{2}}(\hat{a}^\dagger_{\mathrm{sig}} + \hat{a}^\dagger_{\mathrm{LO}}e^{-\mathrm{i}\vartheta}) \end{pmatrix} \; .$$

These fields are then detected by standard photo diodes, giving photo currents proportional to the number of photons in the field

$$\begin{aligned} \hat{i}_1 \propto \hat{n}_1 &= \hat{a}^\dagger_1 \hat{a}_1 \\ &= \frac{1}{2}(\hat{a}^\dagger_{\mathrm{sig}} - \hat{a}^\dagger_{\mathrm{LO}}e^{-\mathrm{i}\vartheta})(\hat{a}_{\mathrm{sig}} - \hat{a}_{\mathrm{LO}}e^{\mathrm{i}\vartheta}) \\ &= \frac{1}{2}(\hat{a}^\dagger_{\mathrm{sig}}\hat{a}_{\mathrm{sig}} - \hat{a}^\dagger_{\mathrm{LO}}\hat{a}_{\mathrm{sig}}e^{-\mathrm{i}\vartheta} - \hat{a}^\dagger_{\mathrm{sig}}\hat{a}_{\mathrm{LO}}e^{\mathrm{i}\vartheta} + \hat{a}^\dagger_{\mathrm{LO}}\hat{a}_{\mathrm{LO}}) \end{aligned}$$

and analogous

$$\begin{aligned} \hat{i}_2 \propto \hat{n}_2 &= \hat{a}^\dagger_2 \hat{a}_2 \\ &= \frac{1}{2}(\hat{a}^\dagger_{\mathrm{sig}}\hat{a}_{\mathrm{sig}} + \hat{a}^\dagger_{\mathrm{LO}}\hat{a}_{\mathrm{sig}}e^{-\mathrm{i}\vartheta} + \hat{a}^\dagger_{\mathrm{sig}}\hat{a}_{\mathrm{LO}}e^{\mathrm{i}\vartheta} + \hat{a}^\dagger_{\mathrm{LO}}\hat{a}_{\mathrm{LO}}) \; . \end{aligned}$$

These photo currents are then electronically subtracted, yielding only the interference terms

$$\hat{i}_2 - \hat{i}_1 \propto \hat{a}^\dagger_{\mathrm{LO}}\hat{a}_{\mathrm{sig}}e^{-\mathrm{i}\vartheta} + \hat{a}^\dagger_{\mathrm{sig}}\hat{a}_{\mathrm{LO}}e^{\mathrm{i}\vartheta} \; .$$

We now linearize the input fields as

$$\hat{a}_{\mathrm{sig}} = |\alpha_{\mathrm{sig}}| + \delta\hat{a}_{\mathrm{sig}}, \quad \hat{a}_{\mathrm{LO}} = |\alpha_{\mathrm{LO}}| + \delta\hat{a}_{\mathrm{LO}}$$

where $|\alpha_{\mathrm{sig}}|$ and $|\alpha_{\mathrm{LO}}|$ denote the coherent excitations and $\delta\hat{a}_{\mathrm{sig}}$ and $\delta\hat{a}_{\mathrm{LO}}$ the noise contributions. The latter are supposed to be small and are only taken into account in first order.

The subtraction of the photo currents can be rewritten as

$$\begin{aligned} \hat{i}_2 - \hat{i}_1 \propto\; &2|\alpha_{\mathrm{sig}}||\alpha_{\mathrm{LO}}|\cos(\vartheta) + |\alpha_{\mathrm{LO}}|(\delta\hat{a}_{\mathrm{sig}}e^{-\mathrm{i}\vartheta} + \delta\hat{a}^\dagger_{\mathrm{sig}}e^{\mathrm{i}\vartheta}) \\ &+ |\alpha_{\mathrm{sig}}|(\delta\hat{a}_{\mathrm{LO}}e^{\mathrm{i}\vartheta} + \delta\hat{a}^\dagger_{\mathrm{LO}}e^{-\mathrm{i}\vartheta}) \\ =\; &2|\alpha_{\mathrm{sig}}||\alpha_{\mathrm{LO}}|\cos(\vartheta) + |\alpha_{\mathrm{LO}}|\hat{X}_{\delta a_{\mathrm{sig}}}(\vartheta) + |\alpha_{\mathrm{sig}}|\hat{X}_{\delta a_{\mathrm{LO}}}(-\vartheta) \; . \end{aligned} \tag{3.1}$$

In the second lines the noise terms are expressed by the generic quadrature operator, introduced in Eq. (2.15).

The first term describes the interference between the DC parts of both light fields. The second term presents the quadrature of the signal field scaled with

the power of the LO field while the last term gives the quadrature of the LO field scaled with the power of the signal field. Since we are interested in the properties of the signal field, it is common to choose $|\alpha_{\mathrm{LO}}| \gg |\alpha_{\mathrm{sig}}|$ in order to make the contribution of the last term negligible. For squeezed vacuum, $|\alpha_{\mathrm{sig}}| = 0$ anyway, however in some experiments, a coherent field with amplitude $|\alpha|$ is co-propagating with the squeezed field for which this condition needs to hold as well. Depending on the relative phase between signal and LO field, we can then inspect the different quadratures of the signal field.

If only vacuum enters the signal port, the variance of the quadrature operator is equal for all quadrature angles and the subtraction is linear to the LO power. Twice the LO power should then result in an increase of the variance by $3\,\mathrm{dB}$. This is a good way to test if the experimental setup is shot noise limited and the homodyne detector is working properly [60].

For a data stream measured with a constant LO power and a fixed phase relation ϑ, the probability distribution is then exactly given by Eq. (2.14). This measurement is used to define the vacuum reference at this LO power.

A squeezed field as a signal field shows a change of the variance depending on the relative phase. The squeezed quadrature will yield a lower variance compared to the vacuum variance at the same LO power.

The homodyne detector is not only a measurement tool for the different quadratures but serves as well as an amplifier for very weak signals like squeezed vacuum fields, consisting only of a few photons for low squeezing values. Even though the field intensities can be too small to be detected with a PIN photo diode, the BHD gives access the quadratures of this state.

The homodyne detector enables a frequency resolved measurement, which means that the noise properties of the signal field can be analyzed at different sideband frequencies.

Stabilization to phase quadrature measurement

If we recall the generic quadrature operator of Eq. (2.15), we find that the phase quadrature is given for $\vartheta = 90°$. Therefore the first term in Eq. (3.1) can be used to stabilize the homodyne detector on the phase quadrature. For $\vartheta = 90°$, the light fields interfere in a way that both photo detectors see the same DC power. The subtraction is then zero and this term vanishes. Tuning ϑ will change the interference in a way that either the first or the second detector sees more of the light, resulting in a proper change of the sign for the subtracted current. It is important to note that the phase relation is then fixed between the LO and the bright light field that caused the interference in the first term. As this method is depending on the intereference, it is not working if the input consists only of

e.g. squeezed vacuum. Therefore we need a light field co-propagating with the squeezed light which enables this technique. In any case it should be clear that the LO is stabilized to a fixed phase relation to this field and not necessarily to the squeezed light field. A stable phase relation between the squeezed field and the auxiliary field is therefore mandatory.

Stabilization to amplitude quadrature measurement

To lock the BHD to the amplitude quadrature of the signal beam, a phase modulation imprinted on the auxiliary field is required. The phase modulation only vanishes in the homodyne detector signal, when the detector measures the amplitude quadrature and gets maximized in the phase quadrature. Therefore, demodulation of the homodyne detector signal with an electronic LO at the phase modulation frequency provides a sinusoidal error signal with a zero crossing exactly when the amplitude quadrature is measured.

Reconstruction of a covariance matrix with homodyne detection

Homodyne detection gives insight to only one quadrature of the state. As the photons are measured and thus destroyed, no other information can be obtained after a homodyne measurement. For characterization of the state just with homodyne measurements, a valid way is as follows. Assuming that the source is preparing exact copies of the state with same properties, one can perform different measurements on different copies to characterize the state. E.g. for a squeezed-light field, first the quadrature yielding the squeezing variance can be measured, followed by a measurement of the orthogonal quadrature to obtain the variance of the anti-squeezing. For a Gaussian squeezed vacuum state these two measurements are already sufficient to characterize the state.

However, to reconstruct the covariance matrix of the state, these two measurements are not sufficient as they do not provide information about correlations between the quadratures. This is especially important for the multi-mode case where the covariance between quadratures of different modes can e.g. be used to witness entanglement in a two-mode-squeezed state.A workaround is to measure additionally a quadrature between amplitude and phase quadrature to get information about the correlations. This technique is proposed and explained in [59]. With a combination of the pure quadrature measurements and e.g. a 45° measurement, the covariance between the two quadratures can be calculated. This procedure enables to reconstruct the full covariance matrix of a squeezed light mode with only one homodyne detector and the reconstruction of the covariance matrix of a two-mode-squeezed state with only two balanced homodyne detectors.
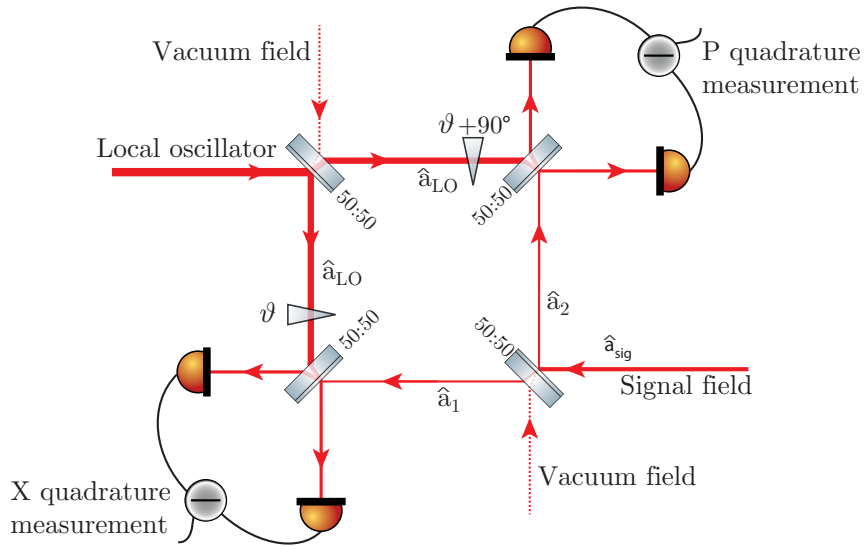
Figure 3.3: Schematic setup of an eight-port homodyne detector: Four incident fields are involved, namely the signal field, the local oscillator and two vacuum fields. The signal field and the local oscillator are mixed with vacuum on beam splitters, respectively. The "copies" of the signal field with the admixed vacuum are send to two balanced homodyne detectors. One detector measures the amplitude quadrature while the other field measures the phase quadrature. With this results, the full information about the signal field can be gained. For the sake of simplicity we leave out the beam splitter of the LO in schematics for the rest of this thesis.

3.2.3 Eight-port homodyne detection

A different method to access the full covariance matrix of a state is *eight-port homodyne detection* (EHD). This section will just sketch the idea of EHD, reducing on the necessary points needed for this work. A detailed description of the technique is given in [54].

The uncertainty relation Eq. (2.21) tells us, that it is not possible to measure both quadratures simultaneously *and* precisely at the same time. However, that means simply, that a simultaneous measurement need to be paid with some loss of the precision of the measurement. At the cost of some extra noise coupling, the following detector scheme, depicted in Fig. 3.3, offers these simultaneous measurements without violation of the uncertainty relation.

To measure both quadratures at the same time, the signal field, denotes by its annihilation operator $\hat{a}_{\text{sig}}$ is split on a beam splitter, given by the symplectic transformation S_{BS} as introduced in Eq. (2.44). A vacuum mode enters at the other

input port of the beam splitter and interferes with the signal field. The outputs $\hat{a}_1$ and $\hat{a}_2$, which are now mixtures of the signal with vacuum are then directed to two balanced homodyne detectors. For the homodyne detection, the local oscillator field is divided on a beam splitter, which causes as well an admixture of vacuum to the local oscillator fields. However, as the LO is a strong coherent field, the vacuum admixture can be neglected for the LO. The detector in the output port 1 is measuring the amplitude quadrature $\hat{X}_1$ of the mixed mode while the other detector measures the phase quadrature $\hat{P}_2$ of the second output. This is realized by choosing the LO phase ϑ for detector 1 accordingly and shift the phase of LO for detector 2 by $90°$ relative to the first. In terms of the input signal the measured quadratures are given by

$$\hat{X}_1 = \tau \hat{X}_{\text{sig}} - \varrho \hat{X}_{\text{vac}} \ , \qquad \hat{P}_2 = \varrho \hat{P}_{\text{sig}} + \tau \hat{P}_{\text{vac}} \ , \tag{3.2}$$

with τ and ϱ denoting the amplitude transmissivity and reflectivity of the beam splitter. A quick calculation of the commutator with usage of Eq. (3.2) shows that these two operators commute and can thus be measured simultaneously,

$$
\begin{aligned}
[\hat{X}_1, \hat{P}_2] &= \hat{X}_1 \hat{P}_2 - \hat{P}_2 \hat{X}_1 \\
&= \tau \hat{X}_{\text{sig}} \varrho \hat{P}_{\text{sig}} - \varrho \hat{X}_{\text{vac}} \varrho \hat{P}_{\text{sig}} + \tau \hat{X}_{\text{sig}} \tau \hat{P}_{\text{vac}} - \varrho \hat{X}_{\text{vac}} \tau \hat{P}_{\text{vac}} \\
&\quad - \varrho \hat{P}_{\text{sig}} \tau \hat{X}_{\text{sig}} - \tau \hat{P}_{\text{vac}} \tau \hat{X}_{\text{sig}} + \varrho \hat{P}_{\text{sig}} \varrho \hat{X}_{\text{vac}} + \tau \hat{P}_{\text{vac}} \varrho \hat{X}_{\text{vac}} \\
&= \varrho \tau [(\hat{X}_{\text{sig}} \hat{P}_{\text{sig}} - \hat{P}_{\text{sig}} \hat{X}_{\text{sig}}) - (\hat{X}_{\text{vac}} \hat{P}_{\text{vac}} - \hat{P}_{\text{vac}} \hat{X}_{\text{vac}})] \\
&= \varrho \tau ([\hat{X}_{\text{sig}}, \hat{P}_{\text{sig}}] - [\hat{X}_{\text{vac}}, \hat{P}_{\text{vac}}]) \\
&= 0 \ .
\end{aligned}
$$

Note, that for this calculation the fact was used that the signal and the incoupling vacuum are independent from each other and thus their quadrature operators commute with each other.

To summarize this, eight fields are involved in this detector scheme, four input fields and four output fields. Due to this reason the scheme is named *eight-port homodyne detector* (EHD). To make the schematic more handy, we leave out the beam-splitting of the LO for the rest of this thesis.

As the EHD enables the simultaneous measurement of amplitude and phase quadrature of the new modes that are mixed with vacuum, the covariance matrix γ_{EHD} of the detected state can directly be reconstructed. However, as we are interested in the covariance matrix of the signal field, we recall from the section 2.4.1 how a beam splitter operation acts on the covariance matrix, given by [64]

$$\gamma_{\text{EHD}} = \tau \gamma_{\text{sig}} + \varrho \gamma_{\text{vac}} \ .$$

The most common case with a balanced signal splitting at the eight-port homodyne detector simplifies this to

$$\gamma_{\text{EHD}} = \frac{1}{2}(\gamma_{\text{sig}} + \gamma_{\text{vac}}) \ .$$

This equation gives us the possibility to get the covariance matrix of the signal field from the reconstructed covariance matrix γ_{EHD}. Recalling from Section 2.2.4 that the covariance matrix of the vacuum state is given by the identity matrix $\mathbb{1}$, the covariance matrix of the signal field before the EHD beam splitter is calculated by

$$\gamma_{\text{sig}} = 2\gamma_{\text{EHD}} - \gamma_{\text{vac}} = 2\gamma_{\text{EHD}} - \mathbb{1} \ . \tag{3.3}$$

By calculating the probability distribution $\text{prd}(X_A, P_B)$ of the eight-port homodyne detector measurement, one can show that the probability distribution is given by [54]

$$\text{prd}(X_A, P_B) = Q(X_{\text{sig}}, P_{\text{sig}}) \ ,$$

so the eight-port homodyne detector measures the Q-function, see section 2.2.5. As discussed in Section 2.2.5 such a measurement corresponds to a projection of the state onto a coherent state α. The complex amplitude $\alpha = \frac{X_1 + iP_2}{2}$ of this coherent state is determined by the measurement outcomes X_1 and P_2.

3.3 Experimental realization of phase noise

3.3.1 Implementation of the phase noise

To investigate the distillation protocol, a noisy channel has to be implemented, which exposes the entangled states to phase noise in a controlled way. The technique, as depicted in Fig. 3.4, is analogue to the one used in [65] and [28].

Here, the phase noise is realized by changing the relative phase of the entangled light field to the LO of the homodyne detector which causes a rotation in the phase space. Experimentally this is done by a steerable mirror in the signal path that is driven by a *piezoelectric transducer* (PZT). The voltage applied to the PZT is changing the position of the mirror and thus the optical path length. Driving the PZT with a voltage that follows the statistic of the phase noise causes then a diffusion in the phase of the light field.

The frequency of the phase noise had to be high enough that it is outside the frequency range of the homodyne detector stabilization. Otherwise the control loop of the homodyne detector quadrature phase would be able to follow these phase changes and thus compensate for the phase noise. To ensure, that the imprinted noise is mirroring the noise introduced to the PZT, the transfer function
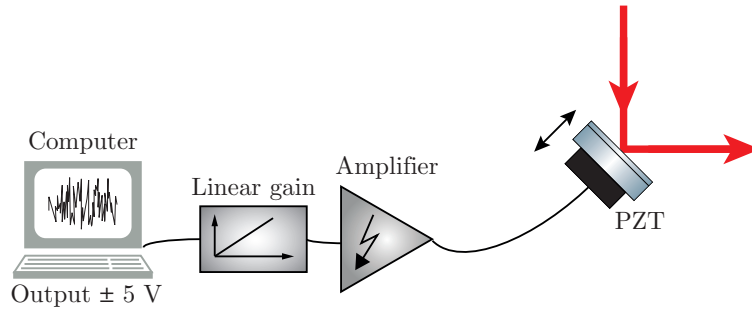
Figure 3.4: Experimental realization of phase noise: The noise is created on the computer which produces an output voltage via the computer soundcard. A linear amplification stage is used to control the strength of the noise. The noise is shifted to positive voltages, amplified with an high voltage amplifier and send to a PZT in the signal path. The optical path length and thus the phase of the signal field is therefore modulated by the noise, mimicking a noisy channel.

of the PZT needs to be flat in this area, which excludes frequencies higher then about 10 kHz as the PZT show resonances in this regime. All these considerations result in a frequency interval between 1 kHz and 5 kHz. The noise was chosen to be white in this range and Gaussian distributed for each frequency. We want to note that, from the theoretical side, there are no restrictions on the noise distribution for a successful distillation. Therefore the chosen experimental realization is solely based on technical considerations to ease the implementation. As the phase noise on the two entangled modes are planned to be independent, two independent phase noise generations are required.

The noise was created with a *LabView* program and saved in an audio file of approximately 37 minutes. The two independent noise traces were saved to the different stereo outputs. With this soundfile, the phase noise can be exported by the computer sound card as a symmetric voltage around zero with a maximal output power of ± 5 V. Selfmade electronics are used to implement a linear gain stage, shift the signal to positive voltages (the PZT can only handle positive voltages) and amplify it.

3.3.2 Estimation of the dephasing parameters

As the experimental implementation of the phase distribution is likely not be perfect, we can not rely on an optimal transfer of the phase noise properties to the light. For this reason, the eight dephasing parameters, introduced in section 2.4.2 are estimated from the data as follows. Additionally to the measurement of a

phase diffused state, a measurement without the implementation of phase noise was performed and used to reconstruct the undiffused covariance matrix. The elements of the covariance matrix are already introduced in Eq. (2.38). If we assume states without any coherent displacement ($\langle\hat{A}\rangle = \langle\hat{B}\rangle = 0$), which is the case for squeezed vacuum states, the covariance can be shortened to

$$\text{Cov}(\hat{A},\hat{B}) = \frac{1}{2}\left(\langle\hat{A}\hat{B}\rangle + \langle\hat{B}\hat{A}\rangle\right) - \langle\hat{A}\rangle\langle\hat{B}\rangle = \frac{1}{2}\left(\langle\hat{A}\hat{B}\rangle + \langle\hat{B}\hat{A}\rangle\right) \ .$$

Having this as the only assumption, the covariance matrix is given by the general form

$$\gamma = \begin{pmatrix} \langle\hat{X}_A^2\rangle & 1/2(\langle\hat{X}_A\hat{P}_A\rangle + \langle\hat{P}_A\hat{X}_A\rangle) & \langle\hat{X}_A\hat{X}_B\rangle & \langle\hat{X}_A\hat{P}_B\rangle \\ & \langle\hat{P}_A^2\rangle & \langle\hat{P}_A\hat{X}_B\rangle & \langle\hat{P}_A\hat{P}_B\rangle \\ & & \langle\hat{X}_B^2\rangle & 1/2(\langle\hat{X}_B\hat{P}_B\rangle + \langle\hat{P}_B\hat{X}_B\rangle) \\ & & & \langle\hat{P}_B^2\rangle \end{pmatrix} \ .$$

The matrix is here for simplicity just presented by the upper half which is legitimate due to the symmetry of the covariance matrix. Note, that the quadrature operators of different modes do commute and the covariance can thus be written in a shorter way for these entries. Analogously, the phase diffused covariance matrix is given by

$$\gamma_{\text{PN}} = \langle S\gamma S^T\rangle_\Phi$$
$$= \begin{pmatrix} \langle\langle\hat{X}_A^2\rangle\rangle_\Phi & 1/2\langle\langle\{\hat{X}_A,\hat{P}_A\}\rangle\rangle_\Phi & \langle\langle\hat{X}_A\hat{X}_B\rangle\rangle_\Phi & \langle\langle\hat{X}_A\hat{P}_B\rangle\rangle_\Phi \\ & \langle\langle\hat{P}_A^2\rangle\rangle_\Phi & \langle\langle\hat{P}_A\hat{X}_B\rangle\rangle_\Phi & \langle\langle\hat{P}_A\hat{P}_B\rangle\rangle_\Phi \\ & & \langle\langle\hat{X}_B^2\rangle\rangle_\Phi & 1/2\langle\langle\{\hat{X}_B,\hat{P}_B\}\rangle\rangle_\Phi \\ & & & \langle\langle\hat{P}_B^2\rangle\rangle_\Phi \end{pmatrix} \ ,$$

where $\Phi(\theta_A,\theta_B)$ denotes the phase distribution of the phase shifts θ_A and θ_B for the two modes A and B, and $\{\hat{X}_A,\hat{P}_A\} = \hat{X}_A\hat{P}_A + \hat{P}_A\hat{X}_A$. The terms for the phase diffused covariance matrix can also be written explicitly by the original undiffused variances, e.g.

$$\langle\langle\hat{X}_A^2\rangle\rangle_\Phi = \langle\hat{X}_A^2\rangle\langle\cos^2\theta_A\rangle_\Phi + 2\langle\hat{X}_A\hat{P}_A\rangle\langle\cos\theta_A\sin\theta_A\rangle_\Phi + \langle\hat{P}_A^2\rangle\langle\sin^2\theta_A\rangle_\Phi \ .$$

The full set of ten equations is calculated in the appendix, see A.2.

As the variances of the undiffused covariance matrix are known due to the measurement of the undiffused state, these equations can be used to obtain a system of linear equations [64]. From this, the eight dephasing parameters can be estimated without requiring knowledge about the exact phase distribution.

CHAPTER 4

Emulated entanglement distillation of non-Gaussian states: Theory

All experimental implementations of quantum information protocols suffer from optical loss and decoherence effects during the transmission, which reduce the non-classical properties of the state. To counteract these effects the idea of distillation protocols has been widely exploited in the last years. Many ideas for distillation protocols in the discrete variable regime were proposed and realized [23, 24, 26, 27] as well as protocols for continuous variables [28, 47, 71, 72]. In this work the focus is on the distillation of continuous-variable entangled states and mainly the distillation against phase noise. Nevertheless, distillation protocols work similarly for other nonclassical states like squeezed states which as well suffer from the effect of decoherence and optical loss as well.

The general idea of a distillation protocol is to start with a large amount of weakly entangled states which are originally strongly entangled but lost their nonclassical properties due to noisy or lossy channels. The distillation protocols recover parts of the entanglement for the price of a smaller amount of states.

This chapter starts with the *no-go-theorem* which predicts the impossibility to distill Gaussian states with Gaussian operations. Focusing on the case where the state is already degaussified, a general protocol for Gaussification and distillation is introduced and the extension to an iterative distillation protocol is described. Based on the iterative protocol, a new approach is presented where the distillation is performed in the postprocessing. This idea was developed by Jaromír Fiurášek and Nicolas Cerf and published in the joint paper together with

some results of this work [46]. As this technique allows any number of iteration steps, we will present some analysis in the asymptotic limit, derived by Jaromír Fiurášek. To make clear which findings and calculations are from him, they will be complemented with the reference [64]. Although experimentally not accessible, the limit gives insight to the performance of the protocol performed in this work and presents a benchmark for the measurement results presented in Chapter 5.

4.1 Restrictions to distillation in the Gaussian regime

Distillation protocols are usually executed in a way that the states are distributed between the parties, which can then perform local operations on their part of the state to perform the distillation, followed by classical communication between the parties. This is generally known under the term *LOCC* (local operations and classical communication). In 2002 it has been mathematically proven by three independent groups that it is not possible to distill Gaussian states with Gaussian methods [43–45]. This restriction is called *no-go-theorem* and reduces the possibilities for distillation in the Gaussian regime. The loophole is to leave the Gaussian regime either with the state which should be distilled or with a non-Gaussian operation in the distillation apparatus. An obvious application is thus the distillation of phase-diffused states which were originally Gaussian states but got diffused in a noisy channel during the transmission. The phase noise reduces the original entanglement in the second moments as shown in Section 2.4.2 and possibly ruins the state for following quantum information protocols. The distillation of phase-diffused states is the main focus of this chapter and will be extensively discussed.

Not covered by this protocol is the group of Gaussian states which show reduced entanglement due to optical loss. Since optical loss can be mimicked by a beam splitter operation and thus maintain the Gaussianity of the state, a non-Gaussian process needs to be included to the distillation in order to recover the entanglement from these states. This can be realized with photon subtraction [30–32,47] or with the idea of noiseless amplification [39–41, 48]. We will focus on this problem in Chapter 6 and investigate some of the prerequisites which these protocols give to the experimental realization.

4.2 Entanglement distillation of degaussified states

4.2.1 Measures for the success of the distillation protocol

The protocols in this section are Gaussification protocols [32, 47, 73, 74] as they drive a degaussified state back to the Gaussian regime. The original state is e.g.

degaussified by transmission through a noisy channel which exposes the modes to phase noise. The degaussification has as a consequence that the state is no longer fully described by the first and second statistical moments, see Section 2.2.4. Intuitively this can be understand in such a way, that the original Gaussian entanglement is shifted to higher moments and consequently the entanglement in the second moments is reduced. Since most quantum information protocols for continuous variables are based on Gaussian states the entanglement therefore seems to be reduced or even lost. As the state is no longer fully described by a Gaussian state, the phase noise also leads to reduced Gaussian purity of the state. In the Gaussification protocol, the nonclassical properties are so to speak shifted back to the second moments, entailing thus a distillation effect and enable following Gaussian information protocols.

The success of the distillation protocol can thus be quantified by an increase of the following three characteristics:

- **Gaussification**: The protocol increases the Gaussianity as the state is driven again to the Gaussian regime. To have an indicator for the Gaussification in the experiment, let us recall that Gaussian states have vanishing higher moments and are completely described by the first and second moment. Monitoring the higher moments of the state before and after the distillation gives therefore a marker for the Gaussification. The undistilled degaussified state will show non-zero higher moments. The distillation protocol will lead to a decrease of these contributions as the state becomes more Gaussian.

- **Distillation**: Under the term "distillation", we want to summarize the improvement of the nonclassical properties like entanglement or squeezing that are increased during the distillation process and thus witness the success of the protocol. To monitor the distillation effect of the protocol, the PPT value μ is given as an entanglement witness, see Eq. (2.48). The squeezing variance of the two-mode-squeezed state show as well the distillation effect.

- **Purification**: Distillation protocols increase the purity of the state, leading to a purification. A general expression for the purity of the state was given by Eq. 2.3. For Gaussian states, a simpler equation can be provided. Combining the expression of the purity via the Wigner function with the Wigner function expression via the covariance matrix, Eqs. (2.25) and (2.18), lead to the following purity equation:

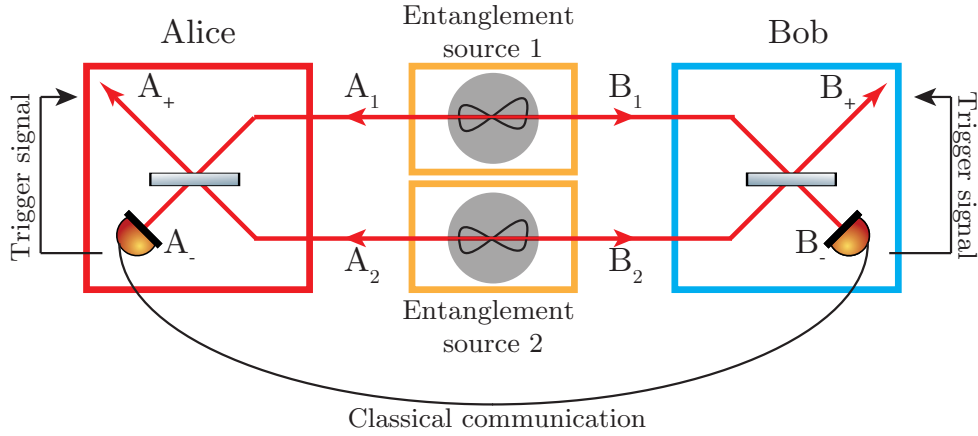$$\mathcal{P}_{\mathrm{G}} = \frac{1}{\sqrt{\det\gamma}} \ . \tag{4.1}$$

Figure 4.1: Elementary two-copy distillation (E2CD): Two copies A_1, B_1 and A_2, B_2
of an entangled state are prepared and sent to the parties Alice and Bob.
The parties superimpose the modes locally on a balanced beam splitter
and perform a projective measurement on one output port. The outcome
of these measurements give a trigger signal for accepting or rejecting the
other output ports. This is classically communicated and the corresponding
modes are only accepted if both measurements yield a positive trigger. The
accepted modes A_+ and B_+ are a distilled copy of the input modes and
show improved properties.

As only Gaussian states are fully described by the first two moments this
equation is correct if the state is Gaussian. However, even for non-Gaussian
states this equation can be seen as an indicator for the Gaussian purity.

4.2.2 Elementary step of entanglement distillation

A typical start for quantum information protocols is that two parties called Alice
and Bob want to share an entangled state. The entanglement is created locally by
one of the parties or by an external party and then distributed to Alice and Bob.
During this transmission, the entangled modes can pass a noisy channel and suffer
from phase noise. To recover parts of the entanglement, a distillation protocol can
be performed.

For an elementary step of the distillation protocol, as depicted in Fig. 4.1, two
copies of the entangled state are needed. We name the modes for Alice A_i and the
modes for Bob B_i, with complex amplitudes α_i and β_i respectively. The index i
is denoting the number of the copy.

Alice and Bob locally interfere their parts of the state on balanced beam split-

ters. The outputs are then given by

$$\alpha_+ = \frac{1}{\sqrt{2}}(\alpha_1 + \alpha_2), \qquad\qquad \beta_+ = \frac{1}{\sqrt{2}}(\beta_1 + \beta_2)$$

$$\alpha_- = \frac{1}{\sqrt{2}}(\alpha_1 - \alpha_2), \qquad\qquad \beta_- = \frac{1}{\sqrt{2}}(\beta_1 - \beta_2)\,,$$

where the plus and minus signs denote the phase flip on the beam splitter.

Alice and Bob locally detect the "minus modes", performing a projective measurement and therefore reduce the state again to a two-mode state. On the measurement result, a distillation condition is applied. There are several distillation conditions possible which are separately discussed in section 4.4. Alice and Bob then communicate over a classical channel the results of their conditioning measurement. Only if the distillation condition is satisfied for the measurement of both parties, the corresponding modes α_+ and β_+ are accepted. All states, for which the condition fails for one or both parties are discarded.

4.2.3 Extending to an iterative protocol

An elementary step of the distillation protocol is not capable of restoring every amount of the original Gaussianity and entanglement. To increase the distillation effect further, the elementary distillation steps can be concatenated and the already distilled states serve as input states for the next elementary distillation step [32, 47]. However it should be noted, that even the iterative protocol can not restore all of the original entanglement as we will discuss later. This has been theoretically proposed in [71] and as well experimentally realized by [33] and [75]. In Fig. 4.2, a *canonical iterative entanglement* distillation protocol with three iteration steps is presented. At the first stage, eight copies of the state are consumed as input states. The four elementary distillation steps are performed simultaneously and the successful distilled states serve as input states for the next stage. With each additional distillation, the purity, Gaussianity and entanglement properties of the state are increased.

Despite their advantages, iterative protocols have some severe problems. One problem is the enormous experimental overhead for the realization of these protocols. Every additional iteration stage is doubling the numbers of copies which need to be provided simultaneously in the beginning. Simply the realization of identical prepared entanglement sources will thus limit the number of iteration steps that can be experimentally realized.

The other problem is the drastically decreasing success probability of the protocol with additional iteration steps. All input states need to be available at
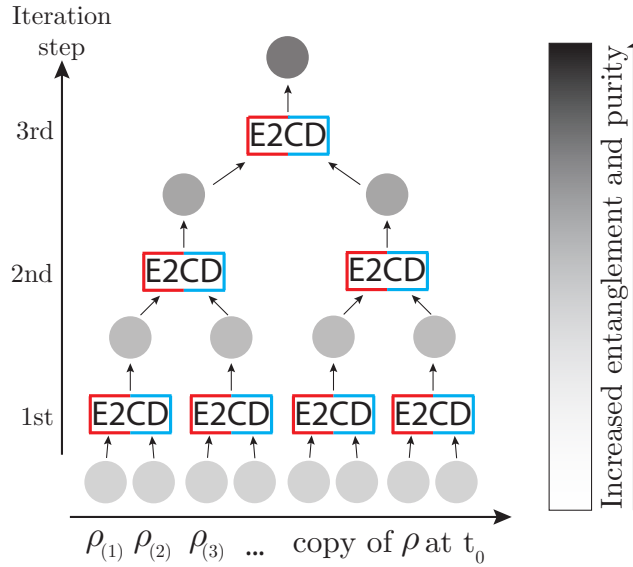
Figure 4.2: Iterative entanglement distillation: At each iteration step, several elementary two-copy distillations (E2CD) are performed. The successful outcomes serve as input states for the elementary two-copy distillations in the next iteration step. Entanglement and purity is increased with each additional iteration step. The different copies of the entangled states $\{A_i, B_i\}$ are here denoted by their density matrices $\rho_{(i)}$ with i giving the number of the copy. As all states at one iteration step need to be available at the same time, all elementary two-copy distillations in one iteration stage need to be performed at the same time t_0.

the same time to perform the elementary distillations in parallel. However, this requires that for the second iteration stage, *all* previous elementary distillation steps need to succeed. If just one elementary distillation fails, the results from all parallel elementary distillation steps have to be discarded. The same is required for further iteration steps, decreasing the success probability even further.

Assuming an elementary distillation steps succeed with a probability of P_1, we can calculate the success probability P_N to create one copy after N iterations. 2^N input states are needed in this case and all $2^N - 1$ elementary distillation steps need to succeed. Therefore the probability that one copy is created in the end is given by $P_N = P_1^{2^N-1}$. On average one thus need $2^N/P_1^{2^N-1}$ input states for one successfully distilled copy. For the continuous-variable protocol, a certain number of distilled states need to be obtained to get statistically relevant results. A decreasing success probability is therefore vastly increasing the measurement time of the experiment as the acquisition of the same amount of data takes significantly longer.

It should be mentioned, that there exist several proposals to use quantum memories [34] in order to make iterative distillation protocols feasible. In the most simple scenario, a quantum memory is used after each elementary two-copy distillation to store the successful result until all parallel stages have succeeded. Ideally this implementation would reduce the number of required input states for one distilled copy to $2^N/P^N$. The development of quantum memories is ongoing, however suited quantum memories are not realized to date.

4.3 New approach: Emulated iterative distillation

A strategy to implement an iterative distillation protocol in an efficient way without quantum memories was proposed by Jaromír Fiurášek and Nicolas Cerf. The core idea here is to shift the experimentally demanding and inefficient part of the distillation to the postprocessing and emulate the distillation. The result of this emulated protocol is identical to the measurement result of a distilled state. In other words, an experimentally performed distillation where the distilled state gets measured afterwards would show exactly the same data.

For this measurement, an *eight-port homodyne detector* (EHD) as introduced in Section 3.2.3 is needed. The fact that a standard BHD is not sufficient can be understand by the following considerations. The crucial part of the emulation is a correct and unconditional prediction of the beam splitter outputs used for the distillation. Using BHD, which measure for example the amplitude quadratures X_1, X_2 of both input fields, a perfect prediction of the amplitude quadratures $X_+ = \frac{1}{\sqrt{2}}(X_1 + X_2)$ and $X_- = \frac{1}{\sqrt{2}}(X_1 - X_2)$ of the output fields is possible. The same is true for a measurement of the phase quadrature.

However, this is no longer working if we want to predict the outcomes of different quadratures for the two output ports, for example the amplitude quadrature of the "plus" port and the phase quadrature of the "minus" port. A prediction of the amplitude quadrature of the "plus" port, given by $X_+ = \frac{1}{\sqrt{2}}(X_1 + X_2)$, requires knowledge of the amplitude quadratures of the input states. At the same time the prediction of the result of the phase quadrature measurement $P_- = \frac{1}{\sqrt{2}}(P_1 - P_2)$ would require a measurement of the phase quadratures of the input states. The homodyne detector measurement provides only the quadrature value of one chosen quadrature. Since a measurement destroys the state, no information about the orthogonal quadrature can be obtained afterwards. In contrast, the EHD provides the complex amplitude $\alpha = \frac{X+\mathrm{i}P}{2}$ of the state and thus enables the postprocessing and emulation of the distillation.

It should be mentioned that emulated distillation is in principle possible with BHDs, in which case one is restricted to one quadrature measurement. This
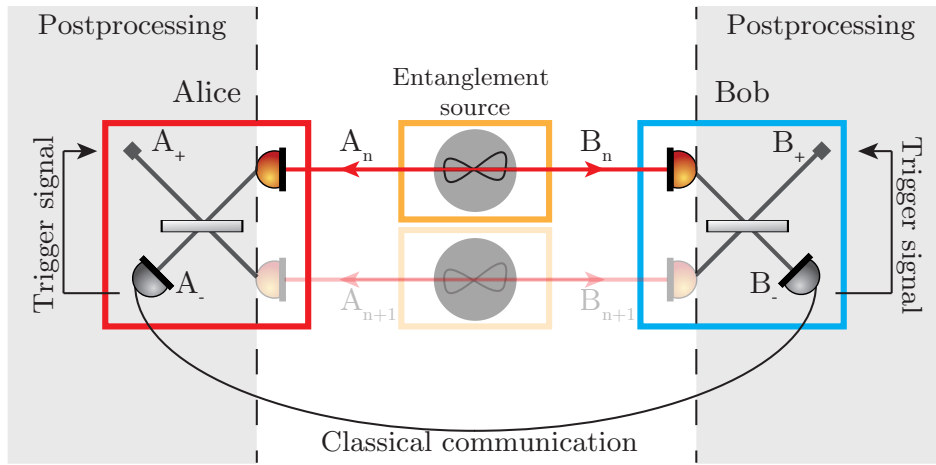
Figure 4.3: Emulation of the distillation protocol: Alice and Bob measure the degaussified entangled states directly and perform the distillation protocol including the beam splitter operation in the postprocessing. The measurement devices are eight-port homodyne detectors, here for simplicity depicted with a single photo detector. As both copies are distributed and detected individually, they do not need to be present at the same time. This is indicated by the transparent second entanglement source. The result of the emulated distillation is identical to the measurement result of a physically performed distillation protocol.

quadrature will thereafter show an improved statistics. However, the full information about the distilled state is not accessible with this device.

The shift of the distillation part to the postprocessing is depicted in Fig. 4.3. For convenience the eight-port homodyne detectors are here simply depicted with a single photo detector. The gray parts are performed in the postprocessing. Since the interaction between the copies happens solely in the postprocessing, the distribution and detection of the two copies is completely independent of each other. This means as well that there is no longer a need for the copies to be present at the same time. As both sources are completely identical, this enables a further simplification of the setup, see Fig. 4.4. Only one entanglement source is necessary to distribute the states to Alice and Bob, measuring their part of the state with an eight-port homodyne detector, respectively. With the measurement results they are able to reconstruct the complex amplitudes α and β of the entangled subsystems. They continuously measure the phase-diffused copies provided by the entanglement source until they have sufficiently large data
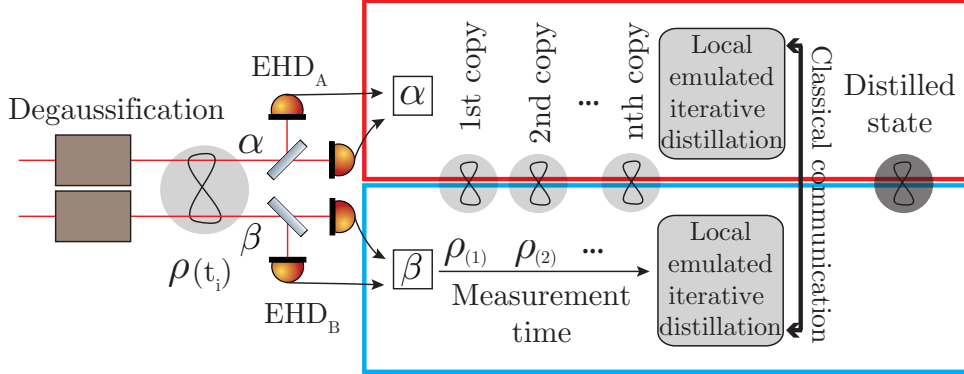
Figure 4.4: New setup for emulated iterative distillation: One entanglement source provides the entangled states which gets degaussified during the transmission. Alice and Bob measure the modes locally with an eight-port homodyne detector and continue this procedure until they share a sufficiently large data set of copies. The iterative distillation protocol is performed in the postprocessing as described in the previous section. In the end, Alice and Bob share a shorter data set with improved properties which is equivalent to the measurement result of a physical implementation of a distillation protocol.

sets $\{\alpha_j\}$ and $\{\beta_j\}$. In the postprocessing they combine their measurement results in pairs to emulate the interference beam splitter:

$$\alpha_{n,+} = \tfrac{1}{\sqrt{2}}(\alpha_{2n} + \alpha_{2n+1}), \qquad \alpha_{n,-} = \tfrac{1}{\sqrt{2}}(\alpha_{2n} - \alpha_{2n+1}),$$
$$\beta_{n,+} = \tfrac{1}{\sqrt{2}}(\beta_{2n} + \beta_{2n+1}), \qquad \beta_{n,-} = \tfrac{1}{\sqrt{2}}(\beta_{2n} - \beta_{2n+1}) .$$

On these states, the distillation protocol is exactly performed like it would have been done in a physical implementation. $\alpha_{n,-}$ and $\beta_{n,-}$ are identical to the measurement results of a projective measurement in the minus ports. On these results, the distillation condition is applied. If the distillation condition is not satisfied for both sides, the corresponding set $\{\alpha_{n,+}, \beta_{n,+}\}$ is discarded. After the conditioning, we obtain a reduced data set from the plus ports, given by $\alpha_j^{(1)} = \alpha_{n_j,+}$ and $\beta_j^{(1)} = \beta_{n_j,+}$ where n_j gives the surviving data of n. The pair $\alpha_j^{(1)}$ and $\beta_j^{(1)}$ represents the output of the first distillation round and can serve as an input for a next iteration of the distillation protocol. After repeating the distillation procedure k times, the outputs will be the shortened data set $\alpha_j^{(k)}$ and $\beta_j^{(k)}$ of the kth iteration step. With this procedure, any number of iteration steps can be realized. The only limiting factor is the length of the initial data stream as

the final data set still needs to be large enough to provide an appropriate statistic. The outcome of the protocol is identical to the measurement result of a distilled state. It can for example be used to obtain a secret key from a data set, which would not yield a positive key rate without the distillation.

It should be explicitly mentioned that the emulated distillation is as efficient as a realization of the iterative protocol with even perfect quantum memories. As the distillation is performed in the postprocessing all successful distillation results can be kept for subsequent iterations. This makes the emulated distillation not only appealing due to the simplified experimental setup but especially due to the improved success rate.

4.4 Projective measurement and distillation conditions

For the elementary two-copy distillation, which is the core element of the iterative protocol, we did not specify the distillation condition and the corresponding measurement device and just claimed it to be some kind of projective measurement. Recalling Eq. (2.6), a state is projected by the projector M_i, if we obtain the corresponding measurement outcome m_i. Although we do not obtain a postmeasurement state in our measurements, the fact that we measure this state alters the corresponding state in the other port. By postselecting on specific measurement outcomes which means successful projection on certain eigenstates, this leads to a distillation effect.

The original proposal is a projective measurement on vacuum, which will consequently lead to a Gaussification of the state and thus to a distillation [32]. Only if the state in the condition path is successfully projected onto vacuum, it heralds a success for the distillation path. For the realization of such a projective measurement in the regime of continuous variables, several approaches are possible which are presented in this section. These distillation conditions do not necessarily have to be realized with an eight-port homodyne detector but include as well proposals employing other measurement devices that were successfully demonstrated in the past already.

It should be mentioned that the underlying process, causing that this conditioning leads to a distillation of the state is not trivial. Therefore no intuitive picture can be presented in this thesis and the reader is referred to the theoretical papers for a more detailed theoretical analysis [32, 47, 71, 76].

4.4.1 Conditioning on projection onto vacuum with photon detectors

The most obvious way to realize a projection on vacuum is the usage of a photon detector, which can distinguish between presence or absence of photons. The

success is heralded if the detector measures no photons, which means a projection on $|0\rangle\langle0|$. The measurements with a projection on any other number of photons, given by $I-|0\rangle\langle0|$ herald a failure and the corresponding state gets discarded. Thus for this measurement an APD which clicks if it measures any number of photons is suitable and the click of the photon gives a veto signal for the distillation. This procedure is proposed in the paper by Browne *et al.* in [32] and Eisert *et al.* [47].

However, single photon detectors are not available with high quantum efficiencies for all wavelengths yet. This results in a projection on vacuum although a photon was present which alters the distillation result and depending on the quantum efficiency can even ruin the protocol. Furthermore, dark counts of the detector will decrease the success rate of the protocol additionally since successful vacuum projections are discarded in this case.

4.4.2 Conditioning on outcomes of quadrature measurements

A different approach has been proposed by Jaromír Fiurášek in [71]. Instead of utilizing APDs, this protocol relies on standard homodyne detection which has the advantage of high quality PIN photo diodes. In this protocol, the minus ports are measured with balanced homodyne detectors. This detectors are set to amplitude quadrature measurement and project the states on the amplitude quadratures with the eigenstates $|X_{A,-}\rangle$ and $|X_{B,-}\rangle$. Alice and Bob communicate their measurement results and combine their measurement results to a joint value $\delta X = \frac{1}{\sqrt{2}}(X_{\mathrm{A},-} - X_{\mathrm{B},-})$. The distillation is successful if the absolute value of $|\delta X|$ is smaller than a tunable threshold T_{acc}:

$$|\delta X| < T_{\mathrm{acc}} \ .$$

This protocol has been experimentally demonstrated in [65] for squeezed states and [28] for entangled states. The distillation condition is visualized in Fig. 4.5, where an the acceptance probability is given in dependence of the joint quadrature result $|\delta X|$.

4.4.3 Conditioning on projection onto coherent states

As the emulated distillation uses eight-port homodyne detectors, these measurement devices should as well be taken into account for the condition measurements in the minus port. The distillation conditions described here are used to perform the distillation for this thesis. As these devices project the modes on coherent states, the measurement results are given by the complex amplitudes $\alpha_- = \frac{X_A + \mathrm{i}P_A}{2}$ and $\beta_- = \frac{X_B + \mathrm{i}P_B}{2}$. $X_{A/B}$ and $P_{A/B}$ denotes here the amplitude and
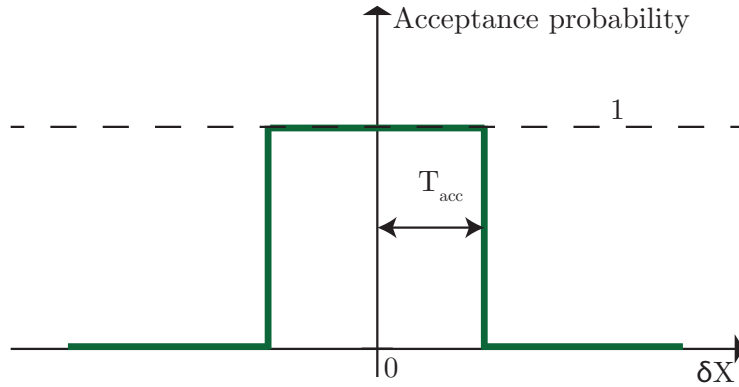
Figure 4.5: Distillation conditioning on outcomes of quadrature measurements: For entanglement distillation, the modes A_- and B_- are measured with balanced homodyne detectors, both measuring the amplitude quadrature of their mode. The measurement results are communicated between the parties, giving the joint quadrature value δX. Alice and Bob accept only the corresponding modes A_+ and B_+ if the absolute value of δX is below a certain threshold T_{acc}.

phase quadrature measurements of the eight-port homodyne detector measurement, respectively.

If only states are accepted where

$$\alpha_- = 0 \quad \text{and} \quad \beta_- = 0 \; ,$$

then this would exactly correspond to a conditioning on successful projection onto vacuum states equivalent to the measurement with the single photon detectors [76]. However, as the outcomes for these measurements are continuous the probability of measuring exactly zero is vanishing. To make this protocol thus feasible, we need to allow some kind of acceptance area, similar to the conditioning on quadrature outcomes.

In analogy to the conditioning on quadrature outcomes, a distillation condition like [64]

$$|\alpha_-| < T_{\mathrm{acc}} \quad \text{and} \quad |\beta_-| < T_{\mathrm{acc}}$$

can be used. As visualized in Fig. 4.6a, this can be seen as a cylindric acceptance area around the origin which we will name the *top-hat condition* for the rest of this thesis. For very small T_{acc}, it converges to a conditioning on successful projection onto vacuum. From a theoretical point of view, this conditioning is not very appealing as it does not lead to a Gaussian state. For a non-zero T_{acc} the distilled state will still have some residual non-Gaussianity even after an infinite
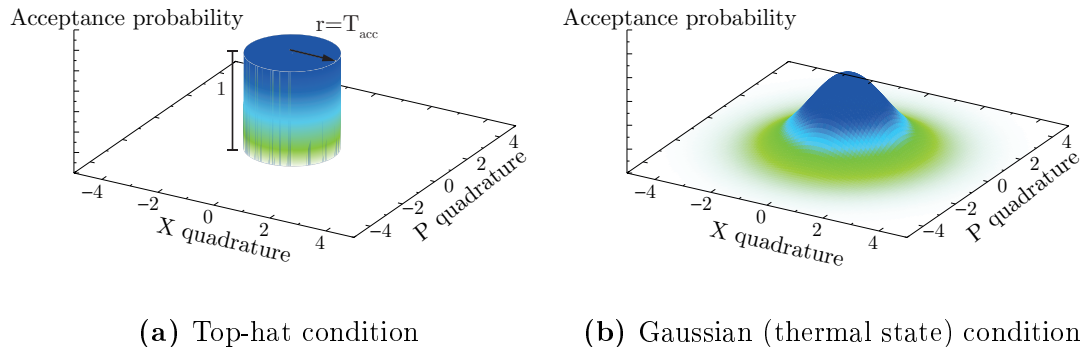
(a) Top-hat condition **(b)** Gaussian (thermal state) condition

Figure 4.6: Conditioning on the complex amplitudes α_- and β_-: (a) Simple conditioning: The threshold T_{acc} gives an acceptance window around the origin. Measurements with a coherent amplitude inside this area are accepted. (b) Conditioning on thermal states: The acceptance condition is given by a Gaussian function of a thermal state with $\bar{n}$ denoting the mean number of photons. The complex amplitude is accepted or rejected with a probability given by the distribution.

amount of iteration steps.

Another possible distillation condition that could be realized with an eight-port homodyne detector is a Gaussian acceptance probability, given by

$$P_{\mathrm{acc}}(\alpha_-, \beta_-) = \exp\left(-\frac{|\alpha_-|^2}{\bar{n}}\right) \exp\left(-\frac{|\beta_-|^2}{\bar{n}}\right) \ . \tag{4.2}$$

In terms of the acceptance function, this can be interpreted as follows. Instead of the cylindric acceptance probability area, the acceptance probability is now given by a Gaussian function $P_{\mathrm{acc}}(\alpha_-, \beta_-)$ of the complex amplitudes. The state with the measurement results α_- and β_- is then accepted with the probability given by the acceptance probability $P_{\mathrm{acc}}(\alpha_-, \beta_-)$. The acceptance probability function is visualized in Fig. 4.6b. The Gaussian character of the acceptance probability guarantees the convergence to Gaussian states in the asymptotic limit of the iterative distillation protocol [47, 76].

Physically, this condition can be understand as a projection of the modes A_- and B_- on thermal states with a mean photon number given by $\bar{n}$. Instead of projecting onto vacuum states, which yield a vanishing success probability, the condition is loosened in such a way that a successful projection on a state with a higher mean photon number $\bar{n}$ counts also as a success. For larger $\bar{n}$, the distillation condition becomes less strict. Using $\bar{n}$ as a tunable variable for the protocol is therefore comparable to the acceptance parameter T_{acc}.

Comparison of the top-hat condition and the Gaussian condition

The Gaussian acceptance probability has a clear physical picture and leads to Gaussian states in the asymptotic limit. This enables calculations of the state in the asymptotic limit and is used for the theoretical analysis of the protocol. Perfect Gaussification, however, is only achieved in the asymptotic limit. If we leave the theoretical view and consider experimental details, this condition has some drawbacks. The additional randomness of the acceptance probability will cause scattering of the data which will increase the amount of data needed for a smooth statistic. And since in an experimental realization only a finite and most likely small number of iterations will be performed, the final data will show some residual non-Gaussianity in both schemes. As the simple distillation approaches the conditioning on projection onto vacuum in the limit of small acceptance threshold T_{acc} a good performance of the protocol can be expected.

In Chapter 5, distillation results for both distillation conditions are presented and it turns out, that the simple threshold is completely suitable for the experimental realization of the distillation.

To make the different distillation conditions comparable, we can try to relate $\bar{n}$ and T_{acc} by equating the variances of the acceptance functions. The Gaussian distribution has a variance of $V_{\mathrm{gaussian}} = \bar{n}/2$ while the simple condition with the cylindric acceptance has a variance of $V_{\mathrm{cylindric}} = T_{\mathrm{acc}}^2/3$. Hence, both acceptance functions are comparable, i.e. accept the same states, if $T_{\mathrm{acc}} \sim \sqrt{\bar{n}}$ [64]. E.g. if T_{acc} is squared, the corresponding value for the other distillation condition would be given by the quadruple of $\bar{n}$. This correspondence will be used later in Section 5.6, when the distillation results for the different distillation conditions are compared.

4.5 Theoretical analysis of the limits of the protocol

4.5.1 Entanglement in the asymptotic limit

For analyzing the quality of the iterative distillation protocol Jaromír Fiurášek derived, based on the theory from [76], a formula for the covariance matrix of the distilled state in the asymptotic limit of the iterative distillation protocol. The formula is derived for the Gaussian distillation condition with a mean photon number of $\bar{n}$, i.e. Eq. (4.2). The covariance matrix in the asymptotic limit then evolves to [46]

$$\gamma_{\mathrm{AB},\infty} = \left\langle S_{\mathrm{rot}}(\theta)[\gamma_{\mathrm{AB}} + (2\bar{n} + 1)\mathbb{1}]^{-1} S_{\mathrm{rot}}^T(\theta) \right\rangle_{\phi}^{-1} - (2\bar{n} + 1)\mathbb{1} \ , \qquad (4.3)$$

where $\mathbb{1}$ denotes the identity matrix and $S_{\mathrm{rot}}(\theta)$ the rotation transformation, i.e. Eq. (2.42). $\langle \ldots \rangle_{\phi}$ denotes the statistical averaging over the random phase
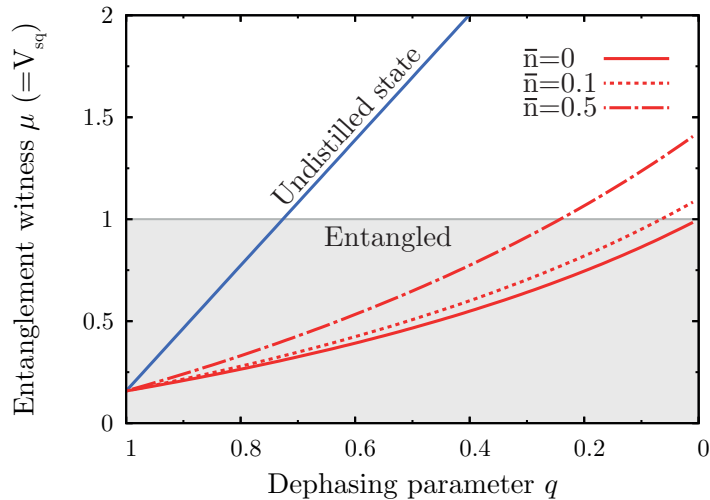
Figure 4.7: Performance of the distillation protocol in the asymptotic limit: The entanglement witness μ is plotted for the dephased state (blue line) and for the distilled state in the asymptotic limit for different $\bar{n}$ (red lines). Details are discussed in the main text. The input state for this calculation is a symmetric pure two-mode-squeezed state with a squeezing variance of $V_{\mathrm{sq}} = 0.158$. The corresponding entries of the covariance matrix are thus $a = 3.234$ and $b = 3.076$, denoting the diagonal elements and the cross correlations of the matrix.

diffusion, see Section 2.4.2.

The performance of the protocol can be quantified if we compare the behavior of the entanglement under phase noise with the restored entanglement in the asymptotic limit of the distillation protocol. In Fig. 4.7, a theoretical analysis for this is shown for which we assume a pure symmetric two-mode-squeezed state and quantify the entanglement by the PPT value μ. For a pure and symmetric state this is identical with the squeezing variance V_{sq}, c.f. Section 2.3.2. The entanglement witness is shown in dependence of the dephasing parameter q, which quantifies the strength of the phase noise, see Section 2.4.2. We assume here for simplicity symmetric and uncorrelated phase noise on both states so that the phase noise strength is completely given by this one parameter. In the figure, the blue solid line shows the behavior of the undistilled state after transmission through the noisy channel. The stronger the phase noise, which corresponds to a smaller q-value, the less entanglement is available in the second moments and for a certain q the state is no longer entangled on the level of the second moments

($\mu \geq 1$). The exact q that is needed to demolish the entanglement in the second
moments is depending on the strength of the initial state. For the exemplary
state in Fig. 4.7 this is the case for $q = 0.73$. The red lines give the entanglement
witness of the state with covariance matrix $\gamma_{\mathrm{AB},\infty}$ in the asymptotic limit of the
iterative distillation protocol for differently tight distillation conditions. The red
solid line is calculated for the ideal case with conditioning on a thermal state
with mean photon number $\bar{n} = 0$, which corresponds to projection onto vacuum.
As stated before, this condition leads to a vanishing acceptance probability and
is therefore not experimentally accessible. However, it denotes the maximum
achievable entanglement which can be recovered for a given dephasing parameter
q. The dashed and the dotted lines are calculated for a more realistic scenario
with different non-zero $\bar{n}$. It is clearly visible that the choice of a smaller $\bar{n}$
results in better distillation effect. The distillation protocol can as well recover
entanglement ($\mu < 1$), even if the dephased state does not show any entanglement
in the second moments ($\mu \geq 1$). This statement is not only true for the ideal case
of projecting onto vacuum but as well for a acceptance conditions with $\bar{n} > 0$.

4.5.2 Maximum tolerable phase noise for pure states

For conditionings with different $\bar{n}$, the red lines in Fig. 4.7 cross the "entanglement
border", meaning $\mu \geq 1$, for different dephasing parameters q. Therefore, there
exists a maximum tolerable phase noise (minimum $|q|$) for which it is still possible
to distill entanglement from a given two-mode-squeezed state. Higher phase noise
values disturb the state in a way, that no entanglement can be restored.
Entanglement is only visible in the asymptotic limit if

$$\mu_\infty = V_{\mathrm{sq},\infty} = a_\infty - |b_\infty| < 1 \; , \tag{4.4}$$

with μ_∞ and $V_{\mathrm{sq},\infty}$ denoting the entanglement witness and squeezing variance of
the asymptotic distilled state and a_∞ and b_∞ giving the entries of the covariance
matrix γ_∞. For Eq. (4.4), we assumed again a pure and symmetric Gaussian two-
mode-squeezed state and used the identity given by Eq. (2.49). With Eq. (4.3)
and Eq. (4.4) a formula for the maximum tolerable phase noise can be determined
to [46, 64]

$$|q| > \frac{\bar{n}}{\bar{n}+1} \tanh r \; . \tag{4.5}$$

 The maximum tolerable phase noise is thus depending on the mean photon num-
ber $\bar{n}$ of the state onto which is projected and on the initial squeezing, given by the
squeezing parameter r. The dependence on $\bar{n}$ is already confirmed and discussed
in the analysis of Fig. 4.7. If the distillation condition is given for successful pro-
jection onto vacuum, meaning $\bar{n} = 0$, it is possible to distill entanglement for any
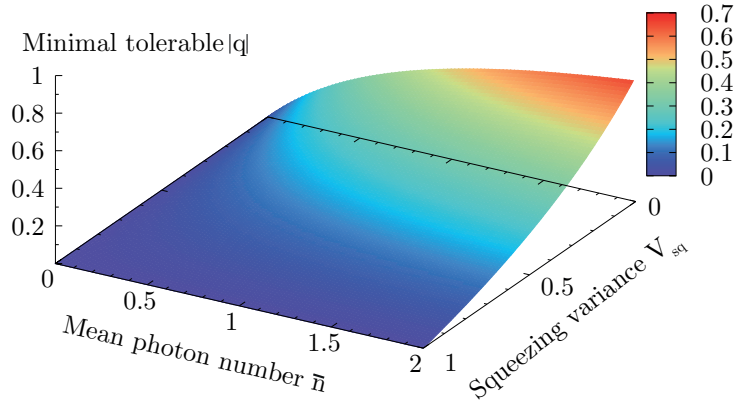
Figure 4.8: Minimal tolerable dephasing parameter q for pure states: This is an illustration of Eq. (4.5) and shows the dependence of the minimal tolerable dephasing parameter q of the mean photon number $\bar{n}$ of the state we project onto and the initial squeezing variance V_{sq} which corresponds to the squeezing parameter by $\exp[-2r] = V_{sq}$, see Eq. (2.36).

phase noise strength $|q| > 0$ and any strength of the entanglement or squeezing. For $\bar{n} > 0$, the maximum tolerable phase noise is as well depending on the squeezing parameter r. Eq. (4.5) is visualized in Fig. 4.8. Here, the minimal tolerable q is shown in dependence of the mean photon number $\bar{n}$ from the distillation condition and the squeezing variance V_{sq} of the initial state. The formula reveals as well, that states with higher squeezing values and thus stronger entanglement are more sensitive to phase noise because the minimum tolerable $|q|$ is higher for high squeezing strength.

4.5.3 Maximum tolerable phase noise for mixed states

For mixed states, which have $a^2 - b^2 < 1$, which is usually the case in real life, the whole situation looks even more critical. Eq. (4.5) changes to [64]

$$\frac{(a + 2\bar{n} + 1)^2 - b^2}{a + 2n + 1 + qb} < 2(\bar{n} + 1) \ .$$

If we now check the limit for $\bar{n} = 0$, we get

$$\frac{(a + 1)^2 - b^2}{a + 1 + qb} < 2 \ .$$

Even for the conditioning on vacuum it is no longer possible to distill entanglement for all phase noise strengths q. This effect is shown in Fig. 4.9. A initial two-mode-squeezed state with squeezing variance $V_{sq} = 0.158$ is effected by different losses ϵ.
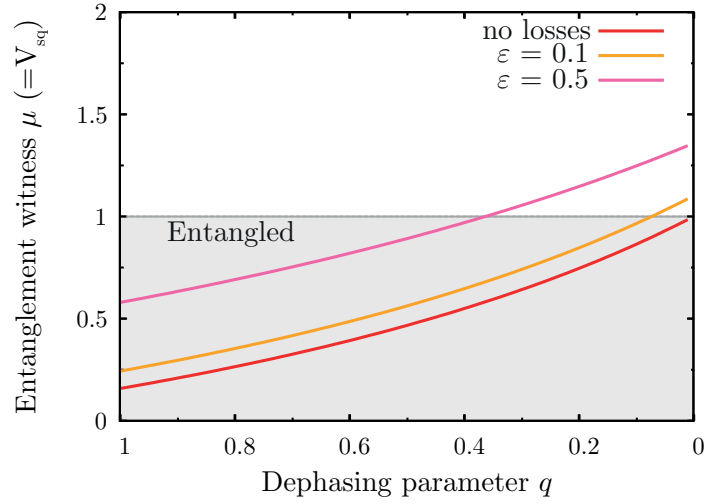
Figure 4.9: Asymptotic limit of distilled mixed states: The entanglement witness μ for an asymptotic distilled state with $\bar{n} = 0$ is shown for different initial states. Identical to Fig. 4.7, the red line gives the limit for a symmetric pure two-mode-squeezed state with a squeezing variance of $V_{\mathrm{sq}} = 0.158$. The orange curve is calculated for the same mode after a lossy channel with a loss of $\epsilon = 0.1$ and the magenta curve for a loss of $\epsilon = 0.5$.

Even for projecting on vacuum, entanglement can no longer be distilled for a non-zero q and higher losses shift the crossing point to larger dephasing parameters.

CHAPTER 5

Emulated entanglement distillation of non-Gaussian states: Experimental realization

---

This chapter is dedicated to the experimental realization of emulated entanglement distillation. The chapter starts with a detailed explanation of the experimental setup, including the locking schemes and technical details. In particular, the generation of the two-mode-squeezed state and the imprinting of the phase noise on this state is briefly recalled from Chapter 3. This is followed by a presentation of the data preparation for the emulated entanglement distillation protocol. As described in Section 4.3, the protocol for emulated distillation is performed and the distillation results for up to three iteration steps are shown. The chapter concludes with an investigation of the Gaussification and purification effect of the distillation protocol and with a comparison of two different distillation conditions, namely the top-hat condition and the Gaussian condition presented in Section 4.4.

5.1 Experimental setup

In this section the experimental setup for this experiment is presented. The full optical setup is depicted in Fig. 5.1. Details of the individual stages are explained in the corresponding sections.
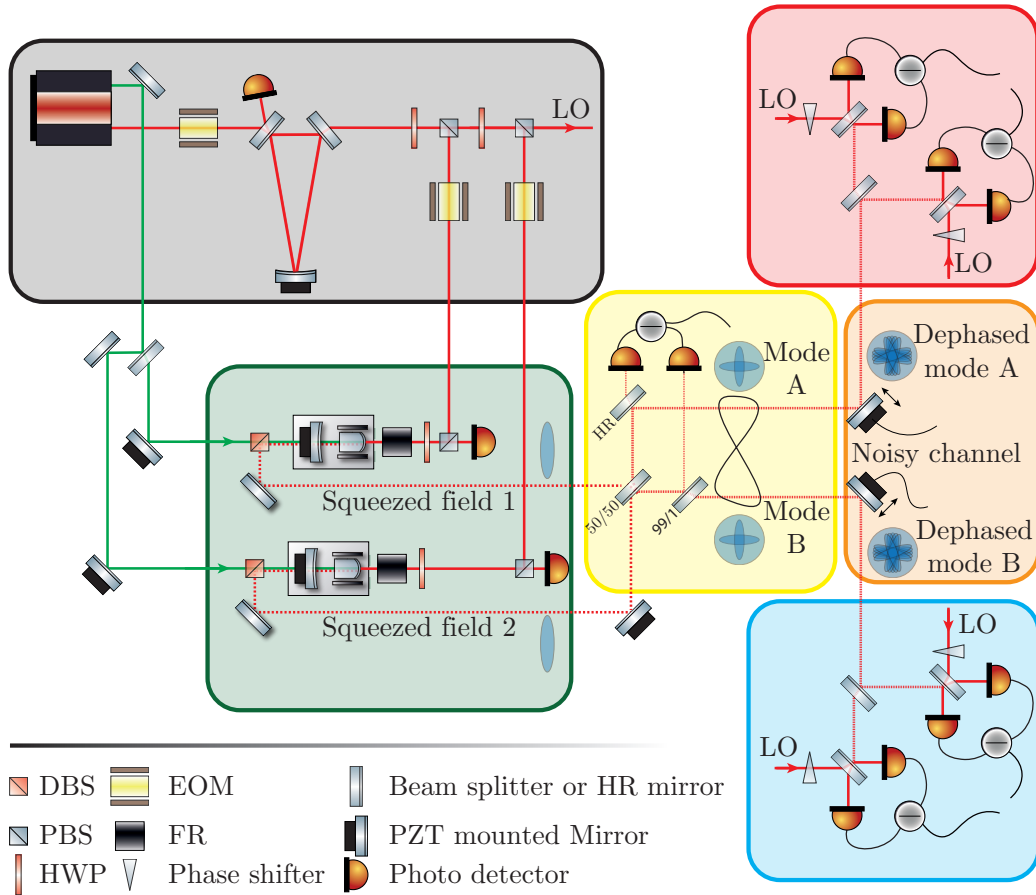
Figure 5.1: Setup for emulated entanglement distillation of phase-diffused states: Here
the complete optical setup is depicted. The setup is divided in subparts:
light preparation (gray box), squeezing generation (green box), entangle-
ment generation (yellow box), noisy channel (orange box) and the eight-
port homodyne detectors of the two parties (red and blue box). All stages
are explicitly explained in the following sections, including description of
the locking schemes and technical details.

Figure 5.2: Preparation of the light fields: The Laser provides the fundamental field at 1064 nm and as well the frequency doubled light at 532 nm. The light gets spatial and polarization cleaned in a filter resonator, providing a clean mode for control fields and local oscillators for the homodyne detectors. The explanation of locking scheme and details of the resonator are given in the main text.
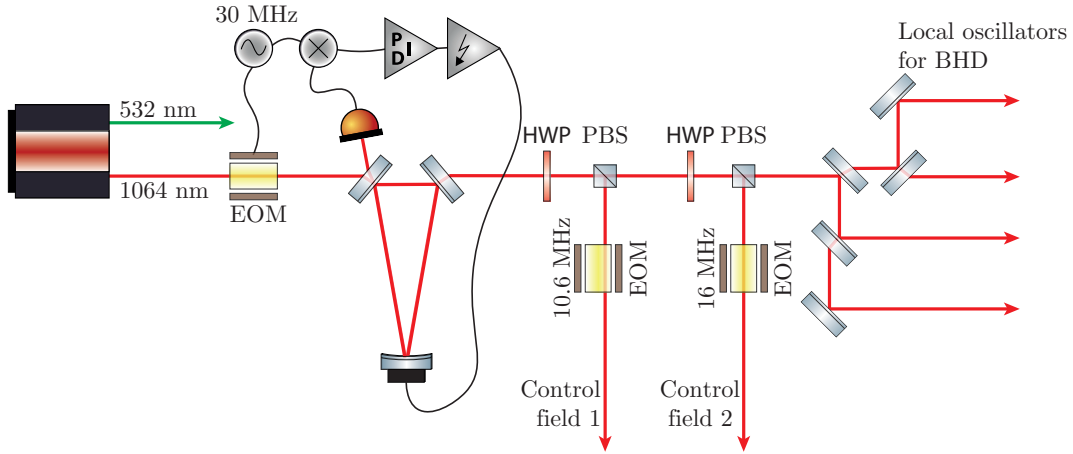
5.1.1 Laser preparation and generation of squeezed states of light

Preparation of the light fields

The light source used for the experiments presented in this thesis is a Nd:YAG laser from the company *Innolight*. The continuous-wave light field (fundamental beam) at a wavelength of 1064 nm has a maximum power of about 350 mW. The laser includes a frequency doubling stage (*second harmonic generation*, SHG) for the generation of light at 532 nm of about 800 mW which serves as a pump beam for the squeezer resonators. Further information about the laser unit and the SHG can be found in [66].

The first stage on the optical table is the spatial and polarization cleaning of the laser beam, shown in Figure 5.2. For this purpose, the fundamental beam is sent through a ring cavity which serves as a *mode cleaner* (MC). The MC ensures that the beam is in a pure TEM_{00} mode and suppresses noise from the laser source. In this experiment, the MC has a linewidth of 1.56 MHz (*'full width at half maximum'*, FWHM) which ensures that the beam is shot-noise limited for sufficiently small powers at the measurement frequency. The *Pound-Drever-Hall* (PDH) stabilization scheme is used to stabilize the resonator [77]. Therefor the light is phase modulated by an *electro-optical modulator* (EOM) at 30 MHz. The reflected light is detected with a photo detector. The *alternating current* (AC) is

converted to a voltage, demodulated at 30 MHz and lowpass filtered. This error signal is sent to a *servo controller* (PID), amplified by a *high voltage amplifier* (HV) and fed back to a PZT that stabilizes the length of the MC.

With a combination of a *half-wave plate* (HWP) and a *polarizing beam splitter* (PBS), the output field is split up. Two beams are used as control beams for the squeezed-light resonators. The other part is again divided by balanced beam splitters to provide the four local oscillator fields for the homodyne detectors with about 3 mW per beam.

The control fields pass another EOM, respectively, that imprints a phase modulation at 10.65 MHz/16 MHz on the respective light field. These modulations are used to stabilize the length of the squeezing resonators. As the modulated control field is partly transmitted through the squeezer, the phase modulations are as well used to lock the homodyne detectors on the amplitude quadrature, see Section 3.2.2.

Squeezing Generation

In this experiment two identical squeezed-light sources were operated to generate the vacuum squeezed states for the two-mode-squeezed state. As they were already built up and used during other experiments, detailed informations can be found in [66]. Each *optical parametric amplifier* (OPA) contains a 7 % magnesium oxide doped lithium niobate (MgO:LiNbO3) crystal with the dimensions $2.5 \times 5 \times 6.5 \, \text{mm}^3$ as nonlinear medium. The back of the crystal is highly reflective (HR) for the fundamental wavelength 1064 nm and as well for the pump field at 532 nm and spherically curved with $r = 8 \, \text{mm}$. The opposite crystal surface is flat and anti-reflective (AR) coated for both wavelengths. The curved side of the crystal forms the hemilithic cavity together with the coupling mirror, see Section 3.1. This mirror has 25 mm radius of curvature and is coated with a reflectivity of 94 % for 1064 nm and 25 % for 532 nm. Therefore, the cavity has a finesse of 100 for the fundamental beam and a finesse of 4.3 for the pump field. The squeezer has a linewidth of about 40 MHz. The coupling mirror back is AR coated for both wavelength and curved with $r = 20 \, \text{mm}$. The curvature provides a lens effect and therefore reduces the divergence of the squeezed light field.

A stabilization on the phase matching temperature was achieved with peltier elements which kept the crystal at a temperature of about 60 °C.

Stabilization of a squeezed-light source with control field

In this cavity design, the length of the cavity is stabilized using a control field at 1064 nm with an imprinted phase modulation. The setup, including the control
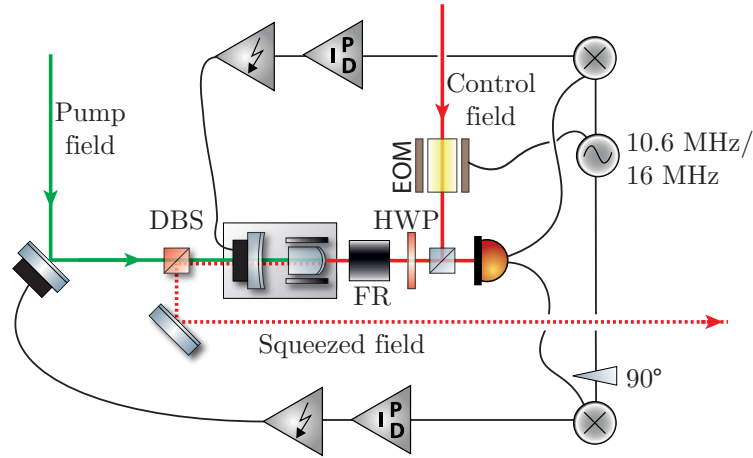
Figure 5.3: Stabilization scheme of a squeezing resonator with a control field. The control field, that couples in from the back is used to stabilize the length of the cavity. The same photo detector signal, demodulated with $90°$ phase shift to the other signal, as well is used to stabilize the pump phase.

loops, is depicted in Fig. 5.3. A PBS which reflects vertical polarized light (s-polarized) and transmits horizontal polarized light (p-polarized) is reflecting the control field that is tuned to s-polarization. The light field is passing a combination of HWP and *faraday rotator* (FR) and enters in s-polarization through the curved crystal side in the cavity. The reflected control field gets rotated to p-polarization while passing the HWP/FR combination. The field is therefore transmitted at the PBS and can be detected by a resonant photo detector. The stabilization of the cavity length is realized with the PDH technique, analogue to the filter resonator. The control field is co-propagating with the squeezed vacuum field. However as this field is shot noise limited above a frequency of about $5\,\text{MHz}$, the unaffected measurement of the squeezed light field is given.

The generated squeezed light field causes amplification or deamplification of the control field, depending on the relative pump phase. Amplification corresponds to a phase-squeezed state in relation to the control field while deamplification corresponds to an amplitude-squeezed state. We can thus say that the relative pump phase defines the squeezing angle ϕ, c.f. Eq. (2.35).

The pump phase is stabilized with the same photo detector which is used for the cavity length stabilization. The AC signal gets therefor mixed with an electronic LO phase that is $90°$ shifted to the LO used for the length stabilization. This demodulated signal provides the error signal for the pump phase which is sent to a steering mirror in the pump beam path.
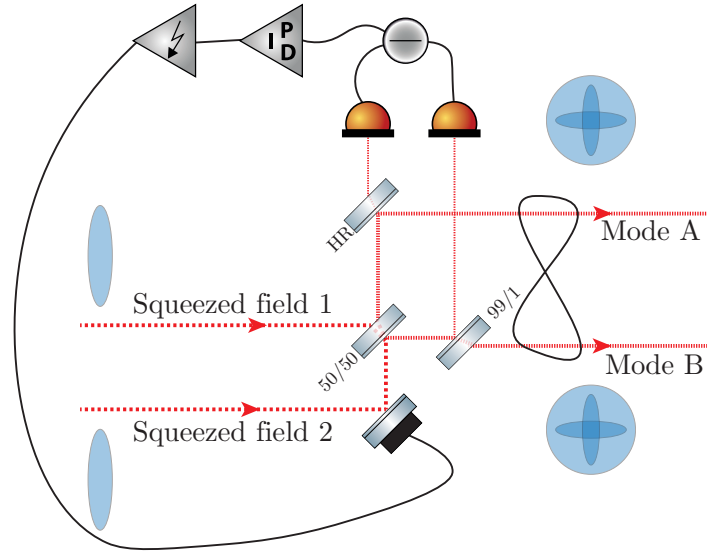
Figure 5.4: Generation of two-mode-squeezed vacuum states: Two amplitude-squeezed states are superimposed on a balanced beam splitter with $90°$ phase shift. The relative phase of the light fields at the beam splitter is controlled with a PZT mounted mirror in one of the squeezed light paths. The error signal for the control loop is obtained analogously to the stabilization of a balanced homodyne detector. For this method, a fraction of both outputs is tapped of to generate the error signal.

5.1.2 Entanglement generation and experimental realization of dephasing in a noisy channel

Preparation of two-mode-squeezed states

To achieve maximum entanglement, the squeezed light fields are superimposed on a balanced beam splitter in such a way that the squeezing ellipses are aligned perpendicular to each other. In the experiment both squeezed-light sources are operated to produce amplitude-squeezing in comparison to their control fields. Maximal entanglement is therefore achieved with $90°$ phase shift to generate a two-mode-squeezed state as explained in Section 2.2.7. With respect to the control field 1, the squeezing field 2 is then phase-squeezed.

As the control fields need to be orthogonal to each other for this scheme, the relative phase can be stabilized identically to the phase-quadrature stabilization of a homodyne detector, see Section 3.2.2. For this reason, a small amount of light is tapped off from both output ports of the beam splitter. In one output it is possible to measure a fraction of the light behind an HR mirror, in the other output port a beam splitter was used which reflects $1\,\%$ of the light to a photo
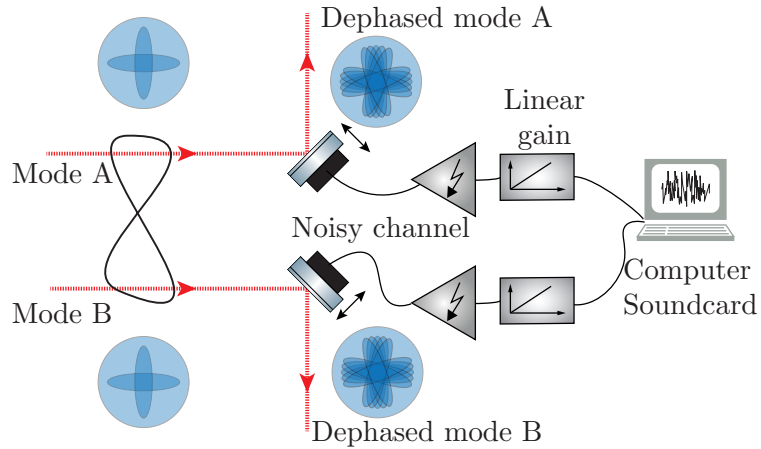
Figure 5.5: Imprinting of the phase noise to the entangled modes. PZT mounted mirrors in the entanglement paths are moved according to the phase noise distribution. This causes a path length change and thus a change in the phase of the entangled light fields. Both modes of the two-mode-squeezed states are diffused individually and independently.

detector. The two photo detector signals are subtracted and provide then the error signal for the beam splitter phase which is controlled with a PZT mounted mirror in one of the squeezing paths.

Simulation of a noisy channel

The experimental realization of the noisy channel is performed as described in Section 3.3 and depicted in Fig. 5.5. The strength of the imprinted phase noise on the PZT mounted mirrors is tunable with the linear amplification stage. The phase noise can be individually set for both modes and was chosen to be uncorrelated. For the experimental results, we performed measurements with different phase noise strengths.

5.1.3 Detection and data acquisition

Detection with eight-port homodyne detectors

The phase-diffused states are sent to the eight-port homodyne detectors. The EHDs including their locking scheme and the data acquisition are shown in Fig. 5.6. The phases of the balanced homodyne detectors are chosen in a way, that the detectors in one arm measure the amplitude quadratures with respect to control beam 1 and the phase quadratures in the other arm. With respect to the
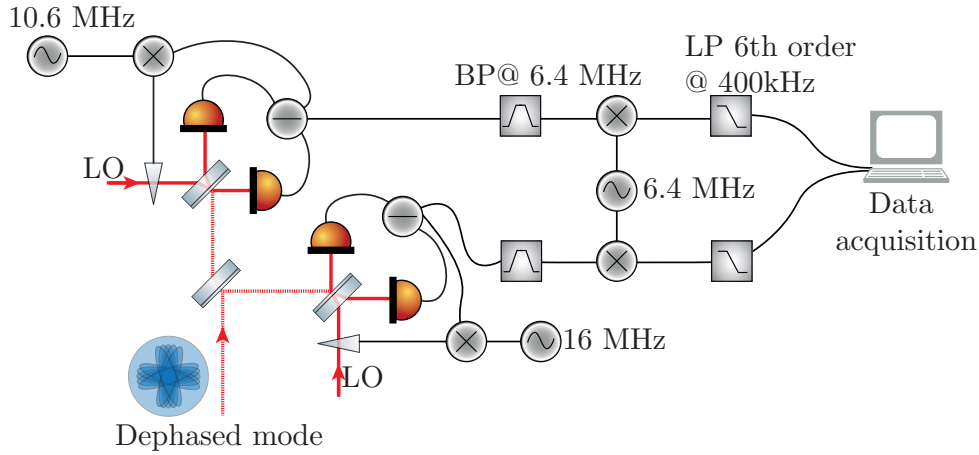
Figure 5.6: Stabilization scheme of eight-port homodyne detection and schematic of the data acquisition. The individual BHDs of the EHD are stabilized orthogonally to each other to the phase quadratures of the control fields, co-propagating with the two-mode-squeezed state. The AC signals are mixed at the measurement frequency of 6.4 MHZ, lowpass filtered and acquired with a data acquisition card at the computer.

control beam 2, the quadratures would be exactly the opposite.

This effect was indeed used in the stabilization method of the detectors. The DC-Lock, which was planned to stabilize one detector in the phase quadrature has turned out to be less stable in time then the lock in the amplitude quadrature. The problem was bypassed as one detector in each arm is stabilized in the amplitude quadrature of one control field, while the other detector got stabilized in the amplitude quadrature of the orthogonal field. The subtraction signal of one homodyne detector of the EHD on each side is thus demodulated at the phase modulation frequency 10.6 MHz of control field 1 while the other subtraction signal is demodulated at the phase modulation frequency of 16 MHz of control field 2. The created error signals are fed back to phase shifters which are positioned in the paths of the corresponding optical local oscillator.

The control loops of the homodyne detectors are implemented in such a way that they only compensate for disturbances below frequencies of about 200 Hz which ensures that the control loops are not capable to follow the phase noise.

Data acquisition

The measurements are performed at a sideband frequency of 6.4 MHz, which is inside the squeezer linewidth and high enough to guarantee a shot-noise limited control field.

To prepare the signals for the data acquisition card, the subtracted signals of the homodyne detector are first bandpass filtered at 6.4 MHz and then mixed with an electronic LO at this frequency. The demodulated signals are then sent to a sixth order lowpass filter with a corner frequency of 400 kHz. The analog signals are converted to digital samples with a 14-bit analog-to-digital conversion card *PCI-6133* from *National Instruments*. All four signals are simultaneously measured with a sample rate of 1 MHz.

The monitoring and data acquisition was performed with a LabView program, based on a program written by Aiko Samblowski [78].

5.1.4 Preparation of the data

The data acquisition system saves the directly obtained voltages from the detectors. To normalize the data to vacuum, an additional vacuum measurement for each BHD is performed. From these results, the vacuum variances are calculated and used to normalize all data samples.

The normalized data is then prepared for the distillation protocol as explained in section 4.3. For this purpose, the complex amplitudes $\alpha_j = \frac{1}{\sqrt{2}}(X_{\mathrm{A},j} + iP_{\mathrm{A},j})$ and $\beta_j = \frac{1}{\sqrt{2}}(X_{\mathrm{B},j} + iP_{\mathrm{B},j})$ are calculated for the whole data set. This is finally the data set on which the distillation protocol is performed. Note that the different prefactors compared to the form given in Section 2.2.5 result from the normalization process of the data.

Additionally, the data can be used to reconstruct the covariance matrix γ_{AB} before distillation. As the full set $\{X_{\mathrm{A}}, P_{\mathrm{A}}, X_{\mathrm{B}}, P_{\mathrm{B}}\}$ is measured at the EHDs, the covariance matrix γ_{EHD} can be obtained. From this, the covariance matrix γ_{AB} before the EHD can be calculated by Eq. (3.3).

5.1.5 Estimation of the dephasing parameter and investigation of an additional loss channel

From comparison of the undiffused covariance matrix γ_{AB} and the diffused covariance matrix $\gamma_{\mathrm{AB,PN}}$ an estimation for the phase noise in terms of the eight dephasing parameters is possible, i.e. Section 3.3 for the method. For this reason, an additional measurement without application of phase noise has been performed.

It turned out that the noisy channels impose as well losses to the states [64]. This becomes obvious by a decreased trace of the covariance matrix which suggests a reduction of the mean number of photons. The additional loss can be explained by the technique that is used to implement the phase noise, i.e. Section 3.3. The phase noise is implemented by a PZT that moves a mirror in the optical path and thus changes the optical path length of the light field. This movement can cause
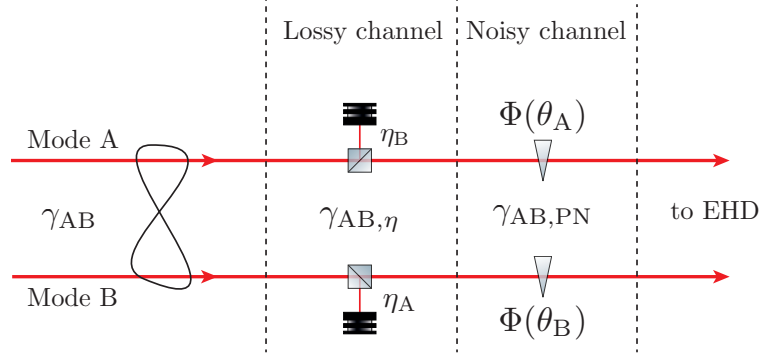
Figure 5.7: Visualization of the lossy and noisy channel applied to the entangled state. The implementation of the phase noise imposes as well losses to the entangled modes which is visualized with an additional loss channel.

slight changes in the spatial orientation which results directly in a reduction of the BHD visibility. This theory is strongly supported by the fact, that we observed higher losses by stronger phase noise implementations.

The efficiencies of these lossy channels can be estimated by [64]

$$\eta_A = \frac{\mathrm{Tr}(\gamma_{A,PN}) - 1}{\mathrm{Tr}(\gamma_A) - 1}, \qquad \eta_B = \frac{\mathrm{Tr}(\gamma_{B,PN}) - 1}{\mathrm{Tr}(\gamma_B) - 1} \; , \tag{5.1}$$

with γ_A and γ_B denoting the covariance matrices of the single modes A and B respectively.

The strength of the applied phase noise is obtained by comparison of the diffused and undiffused covariance matrix as explained in Section 3.3. With the knowledge of the dephasing parameter and the undiffused covariance matrix, the covariance matrix $\gamma_{AB,\infty}$ in the asymptotic limit for the distillation protocol can be calculated, i.e. Eq. (4.3). The calculation, however, gets biased by this additional optical loss which as well alters the covariance matrix. To avoid this problem the two effects can be divided into a lossy channel and a noisy channel. Since pure loss and phase noise are commuting operations this is possible without any restrictions. The concept is illustrated in Fig. 5.7.

Assuming that the state is first passing the lossy channel, the covariance matrix γ_{AB} transforms according to Eq. (2.51) to $\gamma_{AB,\eta}$. In this picture, this covariance matrix is then exposed to the noisy channel. Therefore, $\gamma_{AB,\eta}$ is used to calculate the asymptotic limit via Eq. (4.3).

5.2 The effect of phase noise on entanglement and the possible recovery regime of the iterative distillation protocol

For first investigations, 10^7 samples at each detector are acquired with different noise strength applied. The original (undiffused) state had a two-mode-squeezing variance of $V_{sq} = 0.41$ and the PPT value, which serves as an entanglement witness, of $\mu = 0.46$. The discrepancy between these values indicates that the original state was not symmetric.

Phase noise is imprinted to this state which degaussifies the state and reduces the nonclassical properties. The full set of dephasing parameters is estimated for each applied phase noise strength. In the following the phase noise is only quantified by the dephasing parameter q which, even if the other parameters are not exactly zero, still provides a good marker for the phase noise strength. However, for completeness the full set of parameters is for each measurement listed in the appendix, see B.1. The estimated losses of the additional lossy channel are given there as well.

In Fig. 5.8, the entanglement witness μ under the presence of phase noise is shown by the blue dots. With increasing phase noise, the value of μ is increasing. For $\mu > 1$, which is here the case for approximately $q \leq 0.90$, no entanglement is visible in the second moments.

For each phase noise strength, the covariance matrix and thus the entanglement witness μ in the asymptotic limit can be calculated with Eq. (4.3). The resulting entanglement witnesses μ for conditioning on projection onto vacuum ($\bar{n} = 0$) are shown with the red squares. The asymptotic limit gives the properties of the state after an infinite amount of iterations of the distillation protocol. The conditioning on projection onto vacuum is the optimal conditioning, i.e. Section 4.4. Thus, the red squares mark the absolute bound for entanglement recovery that can be achieved by iterative distillation. Although this bound can never be reached experimentally, the area between these two curves marks the regime in which the distillation results for the entanglement witness μ are expected. The most interesting part is the area, where for the undistilled state entanglement is no longer available in the second moments but the distillation protocol is capable of recovering this entanglement ($\sim 0.90 > q > 0.35$). For higher phase noise strengths, the distillation protocol is not able to restore the entanglement. This can be explained by the fact, that the initial state is mixed due to optical losses, which sets a lower bound to the minimal tolerable dephasing parameter q, see Section 4.5.3.
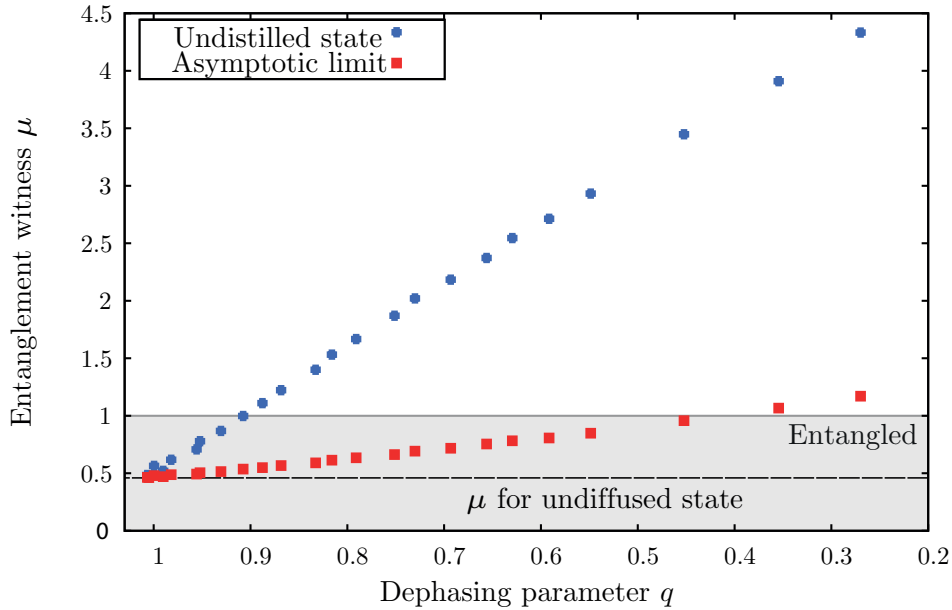
Figure 5.8: Reduction of entanglement due to phase noise and theoretical analysis of the asymptotic limit. The blue dots indicate the value of the entanglement witness μ for a given dephasing parameter q. The red squares denotes the minimal achievable μ value which can be achieved with entanglement distillation. They are calculated with Eq. (4.3) for the asymptotic limit of the distillation protocol with optimal, but experimentally not accessible distillation threshold $\bar{n} = 0$.

5.3 Results for entanglement distillation on 10^7 data points

To investigate the improvement of the nonclassical properties due to the distillation protocol, one iteration step is performed by splitting the samples in two data sets that serve as inputs for the emulated distillation protocol. The distillation is successful if $|\alpha_-| < T_{\mathrm{acc}}$ and $|\beta_-| < T_{\mathrm{acc}}$ is fulfilled, which is the *top-hat condition* from Section 4.4. From the reduced data set the covariance matrix of the state before the EHD is calculated as explained in Section 5.1.4. In Fig. 5.9 the improvement for the entanglement witness μ is shown in dependence of the condition threshold T_{acc} for different strength of the dephasing parameter q.

It is clear to see that the undiffused Gaussian state (black crosses) is completely unaffected by the distillation process as Gaussian entanglement cannot be distilled. For stronger phase noise (decreasing q), the distillation effect becomes more significant. For small dephasing parameters q, no entanglement is witnessed in the second moments ($\mu > 1$) for the undistilled state. For the state presented
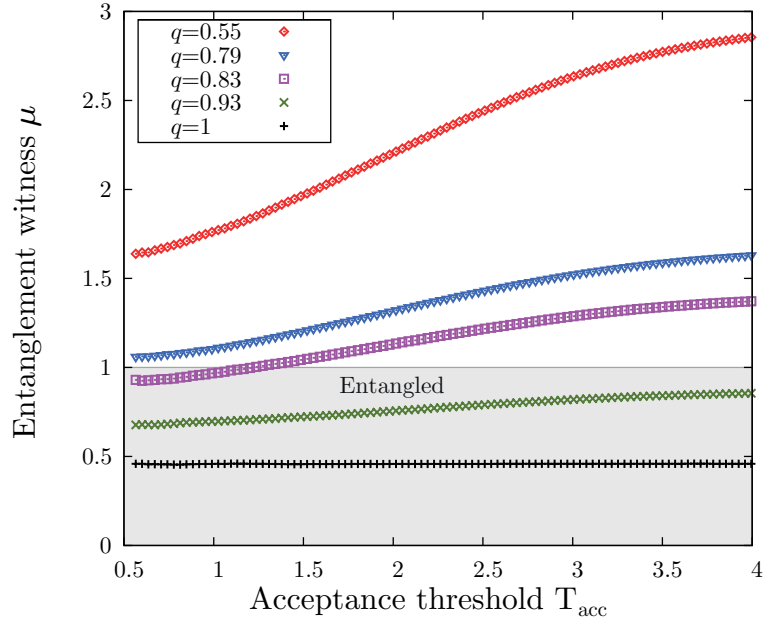
Figure 5.9: Entanglement witness μ in dependence of the acceptance threshold T_{acc} after one iteration of the emulated distillation protocol. The distillation is performed on different data sets that were obtained by the detection of states exposed to phase noise quantified by the dephasing parameter q. From the reduced data set after the distillation, the covariance matrix is reconstructed and the PPT value μ is calculated to provide an entanglement witness.

in Fig. 5.9 this is the case for $q = 0.83$ (purple squares), $q = 0.79$ (blue triangles) and $q = 0.55$ (red diamonds). For the magenta data set the distillation protocol is capable to restore entanglement for a distillation threshold below $T_{\mathrm{acc}} = 1.2$. However, one iteration step is not able to restore entanglement for strongly diffused states, e.g. for $q = 0.83$ and $q = 0.55$.

In Fig. 5.10, the improvement by performing two iterations of the distillation protocol is shown. The successfully distilled data set from the previous section is here again divided into half and the emulated distillation is performed. The second iteration step increases the distillation effect further and the data set for $q = 0.83$, which did not show entanglement after the first iteration of the protocol now has an entanglement witness $\mu < 1$ for thresholds below $T_{\mathrm{acc}} = 1.4$.

The results for the entanglement witness μ start to scatter for small thresholds. This can easily be understood if we recall that for two iteration steps the data was divided in half, distilled, again divided in half and distilled again. For small thresholds, which correspond to a lower success probability of the protocol, this
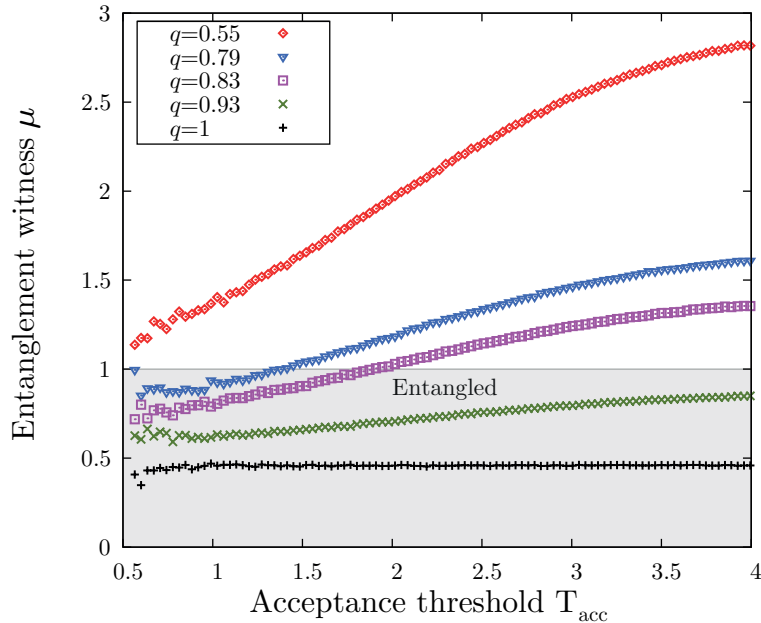
Figure 5.10: Entanglement witness μ for different dephasing parameters q after two iterations of the distillation protocol. The distillation protocol is performed iteratively with the same acceptance threshold T_{acc} in both iteration steps.

results in small data sets that do not have enough data points for adequate statistics. It is therefore natural to investigate the distillation protocol as well in terms of the success probability. The success probability is given by

$$p_{\mathrm{succ}} = \frac{\text{number of successfully distilled samples}}{\text{number of input samples}} \tag{5.2}$$

and can be seen as the "survivor rate" of the data after the execution of the protocol. Lower success probability will result in smaller data sets and depending on the size of the original data set, one should not distill with too small success probability as the statistical relevance is then no longer given.

It is unlikely that a third iteration of the distillation protocol will provide enough data for statistically relevant results. Therefore, the amount of data points taken for one phase noise strength was increased for further analysis in the next section.

5.4 Results for entanglement distillation on $5 \cdot 10^8$ data points

To investigate the effect of the distillation protocol for more iteration steps, a larger data set of $5 \cdot 10^8$ samples was measured. As the data acquisition time increases
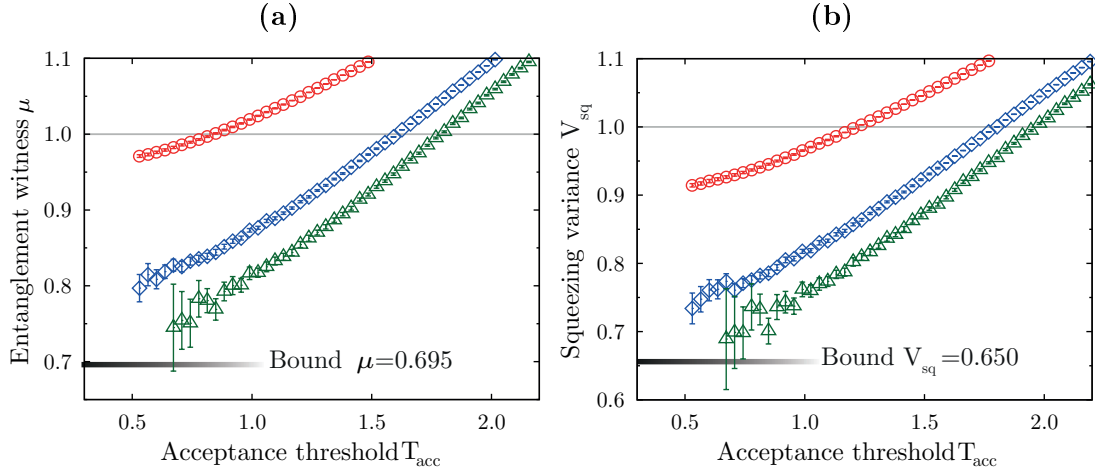
Figure 5.11: Dependence of (a) the entanglement witness μ and (b) the squeezing variance V_{sq} for one (red, circle), two (blue, square) and three (green, triangle) iterations of the emulated distillation protocol on the threshold T_{acc}. The short fading lines give the asymptotic limit of the corresponding variable for conditioning on vacuum $\bar{n} = 0$. The difference between the two values is given by the asymmetry of the entangled state.

significantly for larger data sets, this was only performed for three different phase noise strength. The distillation protocol performs qualitatively similar on each of these data sets. Therefore only the results for one phase noise strength will be shown in the next session.

The undiffused data is again used to reconstruct the covariance matrix before the BS with Eq. (3.3). From this data, the entanglement witness is calculated to $\mu = 0.49$ and the two-mode-squeezing variance is calculated to $V_{\mathrm{sq}} = 0.49$ for the undiffused state. The phase noise applied to this state is calculated to $q = 0.78$. Like in the previous measurement, the noise application adds as well losses to the entangled states and according to Eq. (5.1) the efficiencies of the lossy channels are calculated to $\eta_A = 0.87$ and $\eta_B = 0.95$. For calculations of the properties in the asymptotic limit the covariance matrix $\gamma_{\mathrm{AB},\eta}$ of the state after the lossy channel are used as described in Section 5.1.5.

Three iteration steps of the distillation protocol were performed on the data set with the top-hat distillation condition $|\alpha_-| < T_{\mathrm{acc}}$ and $|\beta_-| < T_{\mathrm{acc}}$. The effect on the PPT value μ and the squeezing variance V_{sq} is shown in Fig. 5.11 for the three iteration steps. An improvement of these properties with every additional iteration is visible. For small acceptance thresholds T_{acc} and increasing iterations, the values for μ and V_{sq} of the distilled state start to look scattered again. The uncertainty of the distillation results due to these statistical effects is quantified by
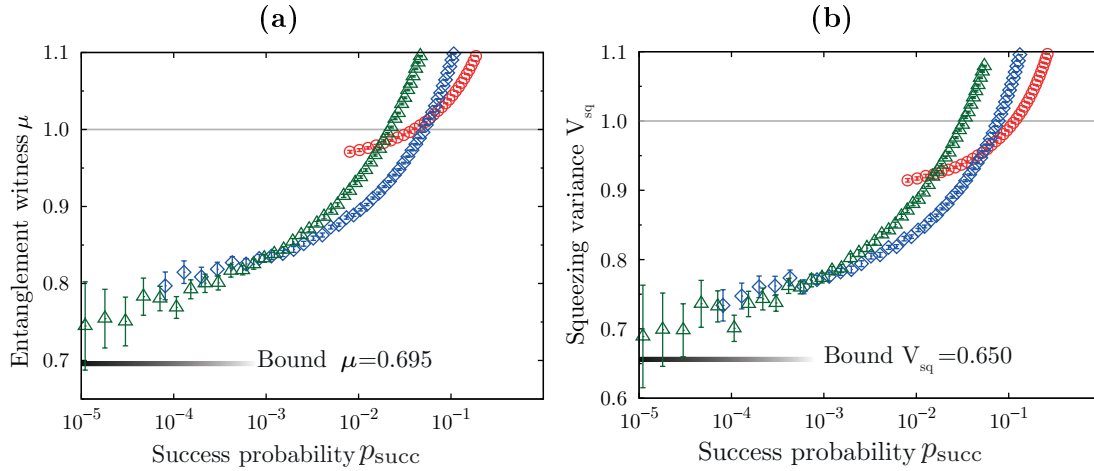
Figure 5.12: Dependence of (a) the entanglement witness μ and (b) the squeezing variance V_{sq} for one (red, circle), two (blue, square) and three (green, triangle) iterations of the emulated distillation protocol on the success probability p_{succ}. The short fading lines give the asymptotic limit of the corresponding variable for conditioning on vacuum $\bar{n} = 0$.

error bars. Therefore, a bootstrapping method is applied to give a 2σ-confidence interval. This method is briefly explained in Appendix B.2.

The short fading lines in the bottom give the calculated values for μ and V_{sq} in the asymptotic limit with conditioning on vacuum. It is quite remarkable how close the distilled properties approach to this limit after the third iteration step.

The true strength of the emulated iterative protocol gets revealed if the results of the iteration steps are analyzed regarding their success rate as it is done in Fig. 5.12. The results from Fig. 5.11 are here presented in dependence of their success probability p_{succ}, see Eq. (5.2). It is clear to see that the curve for the first iteration step is crossing the curve for two iteration steps in the range for $10^{-2} < p_{\mathrm{succ}} < 10^{-1}$. The crossing points mean that from this point on a higher entanglement witness can be achieved with the same success probability if two iterations of the protocol are performed instead of one. Thinking in costs for the experimentalist, one looses less data points for the same distillation result. The crossing point between two and three iterations can be seen for $10^{-4} < p_{\mathrm{succ}} < 10^{-3}$ although the data is there already quite affected by statistic uncertainties.

This result is remarkable as one would first intuitively question if the iterative protocol is efficient in terms of success probability. The decision for an additional iteration step reduces the amount of data by default to half as the data needs to be split for the protocol. However, a higher entanglement recovery for less iterations needs a stricter threshold which also decreases the success probability.
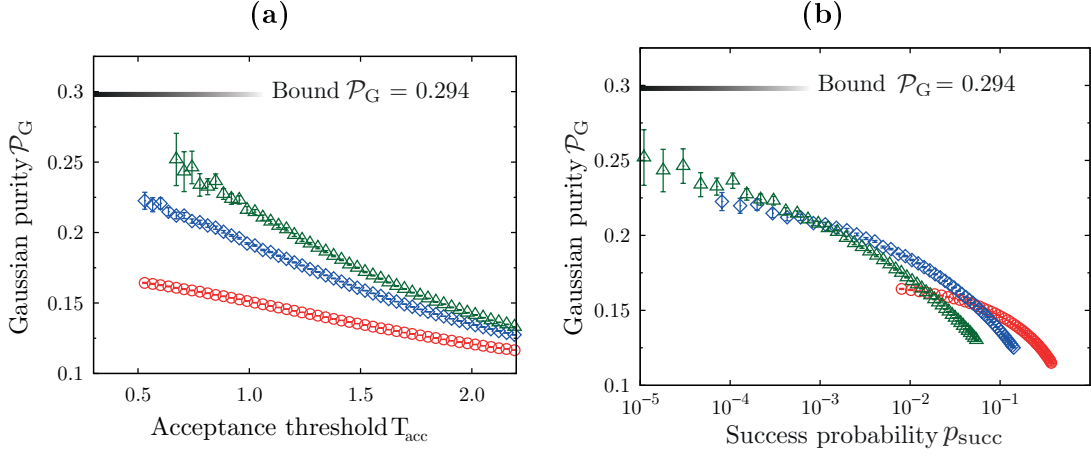
Figure 5.13: Dependence of the Gaussian purity $\mathcal{P}_G$ for one (red, circle), two (blue, square) and three (green, triangle) iterations. (a) Dependence on the threshold T_{acc}. (b) Dependence on the success probability p_{succ}. The short fading lines give the asymptotic limit for conditioning on vacuum $\bar{n} = 0$. The error bars are obtained by a bootstrapping technique, i.e. Appendix B.2.

The optimal way is therefore always a trade-off between these two processes which can be explored and tested with the emulated distillation protocol.

5.5 Further verifications for the success of the distillation

Increase of purity

As discussed in Section 4.2.1, a successful distillation will also increase the purity $\mathcal{P}_G$ of the state, see Eq. (4.1). In Fig. 5.13, the Gaussian purity $\mathcal{P}_G$ is plotted for the distilled states depending on the distillation threshold T_{acc} (a) and the success probability p_{succ} (b). The increase of this parameter strongly suggests an improvement of the state purity. The short fading line presents the optimal value of the asymptotic limit. The general low purity of the state is caused by the mixedness of the undiffused state due to optical losses.

Increase of Gaussianity

Since the distillation protocol presented here is mainly working as a Gaussification protocol it is also possible to monitor this Gaussification process. Gaussian states are completely determined by the first and second moments. As the phase noise degaussifies the state this results in an increase of the higher moments, i.e. Sec-
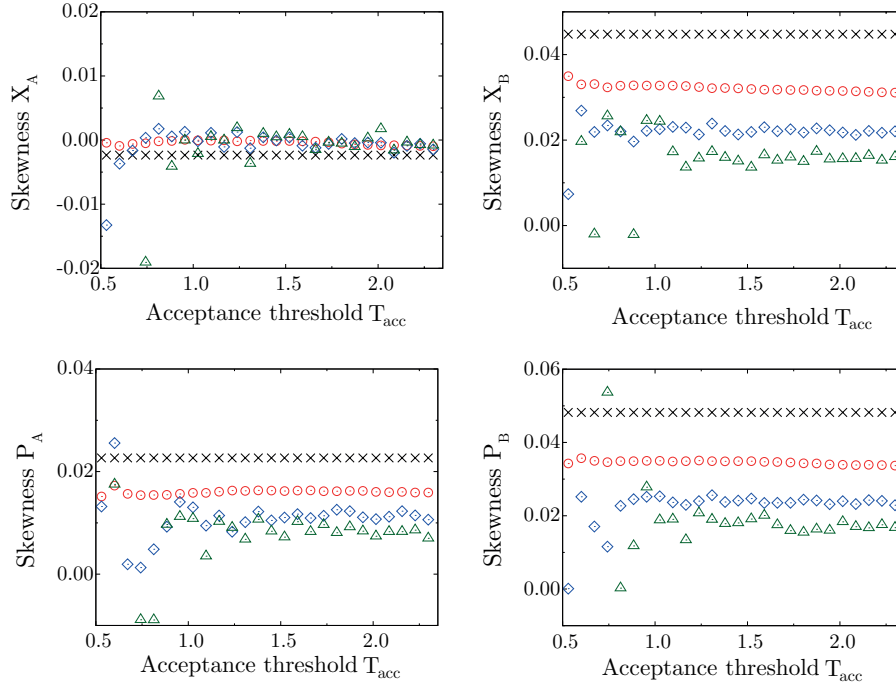
Figure 5.14: Dependence of the skewness on the threshold T_{acc} for the four quadratures for the undistilled state (black, cross) and the state after one (red, circle), two (blue, square) and three (green, triangle) iteration steps. The skewness is calculated according to Eq. (2.9).

tion 2.1.3. In Figs. 5.14 and 5.15, the skewness and the excess kurtosis are shown for all four quadratures of the undistilled state (black crosses) and after the first three iteration steps (color coding as before) in dependence of the acceptance threshold T_{acc}.

The dephased state shows non-zero higher moments which indicate that the state is non-Gaussian while the distilled states show values closer to zero with each iteration step. The discrepancy of the excess kurtosis is hereby bigger then the deviations of the skewness. This is clearly caused by the general form of the applied phase noise which was designed to be symmetric on the state. As the skewness is a marker for the lopsidedness of the distribution, a symmetric noise does not increase the skewness significantly. However, the fact that the skewness does not stay zero shows that the phase noise was not perfectly symmetric. This is as well seen by the other phase noise parameters, see App. B.1.

In contrast, if we recall the effect of phase noise on a Gaussian distribution in Fig. 2.5, we see that it causes a clear tailedness of the distribution. This is confirmed by the comparable high values of the excess kurtosis for the undistilled
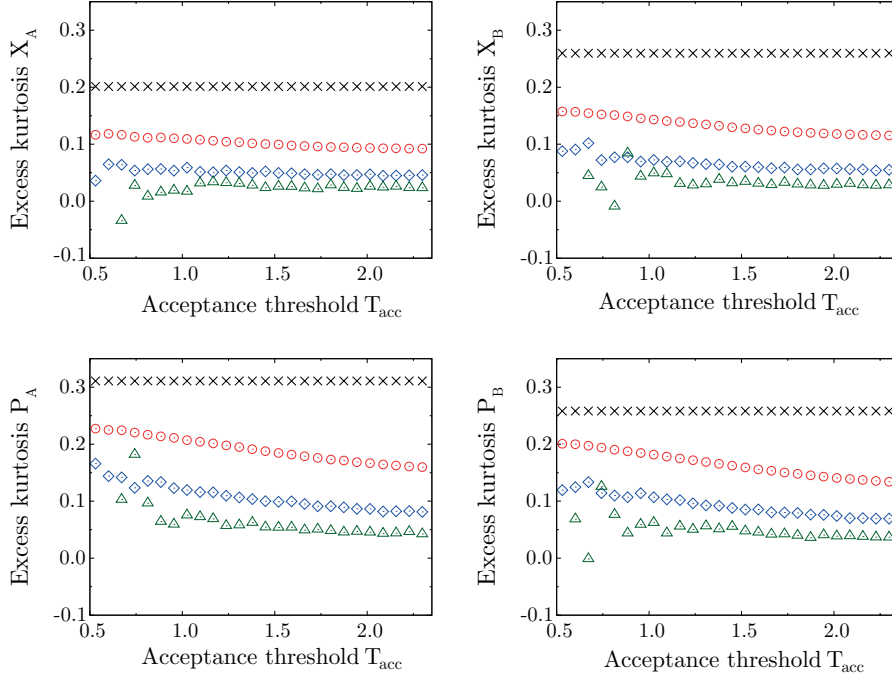
Figure 5.15: Dependence of the excess kurtosis on the threshold T_{acc} for the undistilled state (black, cross) and the state after one (red, circle), two (blue, square) and three (green, triangle) iteration steps. The excess kurtosis is calculated according to Eq. (2.10).

state in Fig. 5.15. Here, the improvement by the iteration steps is clearly visible. The fluctuations for the second and third iteration step at small acceptance thresholds can again be explained with the small residual data set and thus statistical problems.

5.6 Comparison to conditioning on projections onto thermal states

Up to now, we performed the distillation protocol with the top-hat condition in form of a sharp threshold in phase space, i.e. Section 4.4. It is not intuitively clear, that this condition leads to a distillation effect for non-zero T_{acc}. However, the distillation results show clearly the success of the protocol with this threshold. For comparison in this section the distillation results with the Gaussian conditioning on thermal states with mean photon number $\bar{n}$ are presented. The distillation is performed on the same data set as in the previous section. To give a comparability to the conditioning with T_{acc} as the tunable parameter, the distillation results are

(a) **(b)**

Figure 5.16: Dependence of (a) the entanglement witness μ and (b) the squeezing variance V_{sq} for one (red, circle), two (blue, square) and three (green, triangle) iterations of the emulated distillation protocol. Here the distillation is performed by conditioning on projections onto thermal states with me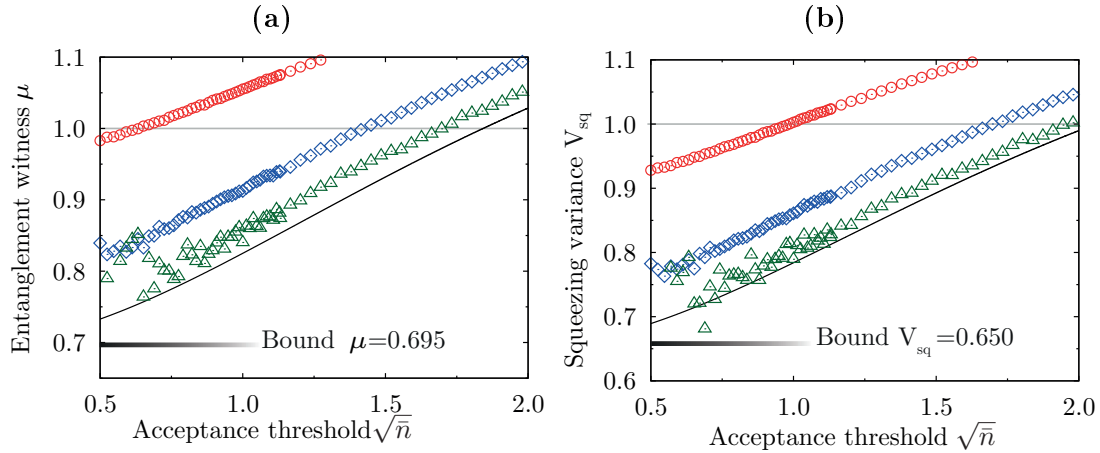an photon number $\bar{n}$. The distillation results for μ and V_{sq} are given in dependence of $\sqrt{\bar{n}}$. The black line gives the asymptotic limit for conditioning on a thermal state with the respective $\bar{n}$. The short fading line gives the asymptotic limit for conditioning on vacuum, $\bar{n} = 0$.

shown in dependence of $\sqrt{\bar{n}}$. The explanation for this connection is given at the end of Section 4.4.

In Fig. 5.16, the distillation results for the entanglement witness μ and the squeezing variance V_{sq} for conditioning on projection onto thermal states is presented. As the asymptotic limit can be calculated for each $\bar{n}$, the limit is given by the black curve in each of these plots. It is clear to see that the distillation results are following the slope of the asymptotic limit. As well it becomes obvious, that the distillation results of one iteration has more or less the same distance to the asymptotic limit, regardless the value of $\bar{n}$. This underlines the good performance of the iterative distillation protocol even after the execution of three iteration steps. Compared to the top-hat condition, the qualitative behavior is identical and the improvement with each iteration is visible. However, the data is more scattered for three iteration steps already by larger thresholds. This is caused by the additional randomness, that is introduced due to the condition.

To conclude, both methods show obvious distillation effects on the data which increases with increasing number of iterations and gets better the closer the distillation condition is chosen to the successful projection onto vacuum states. However, the top-hat condition showed for the same data set smoother curves which

is caused by the additional randomness of the other protocol. This approves the choice for the top-hat condition for the main analysis of the protocol. Nevertheless, the other condition showed as well satisfying distillation results and verifies the overall good agreement with the theoretical modeling of the asymptotic limit as shown in Fig. 5.16.

5.7 Conclusion

In this chapter we presented the measurement, postprocessing and analysis of data, taken for emulated entanglement distillation. The entanglement source is a two-mode-squeezed state, created by the overlap of two squeezed vacuum states. The noisy channel is simulated with PZT mounted mirrors in the entanglement paths, which enables to add different strength of phase noise to the modes. The entangled diffused modes are detected with an eight-port homodyne detector respectively. Afterwards the distillation protocol as introduced in Section 4.3 is performed in the postprocessing.

The measurement results for different phase diffusion strength are shown for two iteration steps. For a larger data set up to three iterations of the emulated distillation protocol are realized. The increase of nonclassical properties like entanglement and two-mode squeezing is presented but as well the improvement of purity and Gaussianity of the state is verified. Especially we showed, that the protocol is capable to restore quadrature entanglement ($\mu < 1$) from dephased states which do not exhibit any entanglement witness in the second moments. The theoretically calculated asymptotic value for all properties provides a comparison how good the protocol has performed. We made a comparison to a different distillation condition and showed that the simple condition with a sharp threshold is well suited for the distillation protocol. The plots for the properties in dependence of the success probability p_{succ} show the strength of the emulated distillation protocol as one can optimize the distillation parameter for a maximum amount of surviving data.

The emulated distillation protocol presented in this chapter does *not* provide a distilled state that is physically available for subsequent experiments. Thus, this distillation protocol is *not* capable to improve states e.g. for quantum teleportation. However, for an external observer, the distilled data set of the emulated distillation shows no difference to the result from a physical implementation of an iterative distillation with a subsequent EHD measurement.

Consequently, this protocol is particularly well suited for all experiments that terminate with an eight-port homodyne detector measurement. This makes this protocol especially interesting for quantum key distribution protocols [79–81]. For

such protocols the secret key rate can be improved by emulated distillation of the distributed data.

CHAPTER 6

Prerequisites for emulated entanglement distillation of Gaussian states

---

This chapter is dedicated to the development of a stabilization scheme for eight-port homodyne detection without the need of a bright light field co-propagating with the squeezed vacuum field. To test these techniques, the stabilized detection of a squeezed vacuum field with an eight-port homodyne detector (EHD) is realized. In the experiment presented in Chapter 5, a control field with an imprinted phase modulation is used to stabilize the length and phase of the squeezed-light source as well as the relative phases between light fields interfering on the beam splitters for entanglement generation and balanced homodyne detection. The presence of a bright light field however makes the usage of single photon detectors like APDs difficult or even impossible. These detectors are sensitive to single photons and are quickly saturated even for low intensities.

In this chapter, we will first motivate why there is a need for EHD without a bright light field as such a setup is necessary for emulated entanglement distillation against optical losses. Then the experimental setup is described and a characterization of the utilized squeezed-light source and the homodyne detectors is given. We present as well a method to stabilize the phases of the EHD without a bright light field in the signal path. In the following section, a stabilized measurement of a squeezed vacuum field with the EHD is presented and the quality of the state measured with the EHD is compared with a direct measurement of the squeezed state on just one BHD. The chapter concludes with the presentation of the idea how the locking scheme for the phases can as well be used for the sta-

bilization of filter cavities in a single photon path. The experiment provides thus all techniques to perform a generic emulated distillation on Gaussian squeezed or v-class entangled states.

6.1 Motivation - Distillation against optical loss

This section gives the motivation for an experimental setup that works without a bright light field and as well points out the requirements on the experimental setup. The implementation of the single photon subtraction is briefly sketched to highlight the needs for the setup. For detailed information the reader is referred to the given references.

The experiment presented in Chapter 5 shows the successful realization of an emulated multi-copy iterative entanglement distillation protocol. The emulation, based on EHD, makes the iterative protocol feasible. The distillation is performed on degaussified states which enables a distillation method only with Gaussian operations. However, as mentioned in the theoretical treatment of distillation, i.e. Chapter 4, the distillation protocol can as well be performed on Gaussian states, e.g. to distill optical loss. In this case, one needs to implement a non-Gaussian operation to the distillation protocol to circumvent the no-go theorem, i.e. Section 4.1.

A method that is already exploited in several experiments as [30, 31] is the subtraction of a single photon from an entangled state. This is a non-Gaussian operation that leads to a degaussification of the state. The distillation can then be performed with the Gaussification protocol analogue to the distillation of the phase-diffused states.

Experimentally, single photon subtraction is realized by implementing a beam splitter with a very low reflectivity in the path of the signal field. For a sufficiently low reflectivity, only a single photon is tapped off and the probability for reflection of more then one photon at the same time is small. An APD detecting the reflected part can herald the presence of this photon which means that the photon has been subtracted from the signal field. The signal field itself is detected with a BHD or an EHD. The states reaching the detector are mixtures of the unaffected Gaussian entangled states and the degaussified states where a single photon is subtracted. Conditioning of the detector on the heralding of the APD will select only the states which show the non-Gaussian statistic and enables the subsequent distillation.

Experiments to distill Gaussian states with conditioned photon subtraction have already be performed by [30, 31]. In this experiments, solely the subtraction of a single photon from each of the entangled modes was performed without a sub-

sequent distillation protocol as this already shows an improvement in the entanglement witness of the state. Combined with the emulated distillation from the previous chapter, the conditioned eight-port homodyne detection of the entangled modes would provide a generic distillation protocol which yields the measurement results of Gaussian purified states as outcome. The reader should note that the distillation of optical loss is only capable to counteract losses that happen before the photon subtraction. Losses that happen afterwards are still affecting the state. Therefore the subtraction should ideally happen in the last possible step and the detection still needs to be performed with high quality photo detectors.

6.1.1 Requirements for the experimental realization

The implementation of APDs imposes several restrictions on the experimental setup. As already mentioned, single photon detectors are designed for small intensities. Any bright light field co-propagating with the signal field is also partially reflected and this part can saturate the detector or even destroy it. Additionally, subtracted photons from the co-propagating field are as well detected by the APD and cause a herald signal. In this case however the signal field is not degaussified which results in a mixed detected state that will reduce the success of the distillation. For this reason a realization without an additional bright field co-propagating with the signal field is desirable.

The second restriction is that single photon detectors do not measure frequency resolved. That means that, within their frequency bandwidth which is usually quite broadband, they herald every photon arriving in the same way, regardless of the frequency. A BHD however is limited to a frequency range given by the photo diodes and the electronics of the detector. A heralded photon from the APD in a frequency range where the BHD is blind will result in the measurement of vacuum. This appears as optical loss on the state at the detector, unavoidably decreasing purity and entanglement of the state. The bandwidth of the light impinging on the APD should therefore be filtered to match the range of the detector. This can be realized with filter cavities in the reflected single photon path as for instance demonstrated in [30,82]. The correct choice of the detection bandwidth is depending on several conditions that need to be considered. First, the linewidth of the filter cavities in front of the APDs should not be chosen too narrow. The implementation of filter cavities with small linewidth in comparison to the squeezer linewidth can cause problems to correlate the single photon event to the corresponding state on the homodyne detector due to long intra cavity round trip times [82]. On the other hand, the two-mode-squeezed light field has a limited bandwidth in which the entanglement is present. The bandwidth of the entanglement is depending on the bandwidth of the squeezed-light sources provid-

ing the squeezed states for the entangled state. As the detected entanglement will be an average of the entanglement strength over the whole frequency bandwidth, this gives an upper limit to the measurement frequency range. The BHD should also be flat in the measurement bandwidth as its transfer function would affect the detected signal field otherwise.

To conclude, the optimal frequency band is depending on the linewidth of the squeezed-light source and the desired average entanglement. The homodyne detectors should be capable to measure sideband frequencies in the whole measurement frequency range and provide a flat transfer function. Within the possibilities of the detector frequency range and the available squeezing at different frequencies, the measurement range should be chosen as high as possible to avoid problems in the correlation between the single photon event and the detector measurement. In the following section the experimental setup will be introduced. Keeping the considerations that we just made in mind, the linewidth of the squeezed-light source will be characterized and a suitable homodyne detector will be presented. Squeezed light resonator and homodyne detectors will be stabilized with a method that does not rely on a control field co-propagating with the squeezed vacuum field.

6.2 Experimental setup

In this section the complete experimental setup is presented for the stabilized eight-port homodyne detection without bright light field. The setup is depicted in Fig. 6.1 and consists of the laser light preparation, the squeezed-light source and the eight-port homodyne detection. The stabilization schemes are explained in detail in the respective sections. This section contains as well a presentation and characterization of the squeezed-light source and the broadband homodyne detectors used for this experiment.

6.2.1 Laser light preparation

The light source used in this experiment is the same as in the previous experiment. As far as basic information or the stabilization techniques are identical to the previous experiment, a detailed description is skipped here and the reader is referred to Chapter 5.

An EOM imprints a phase modulation at 72 kHz onto the infrared light field at 1064 nm. This phase modulation is used for the PDH stabilization of the mode cleaner length. In this experiment the MC has by design a linewidth of 751 kHz for s polarized light, a finesse of 950 and roundtrip length of 42 cm. The spatial and frequency cleaned output light is divided by two HWP/PBS combinations. Two fields serve as local oscillators for the eight-port homodyne detector and one
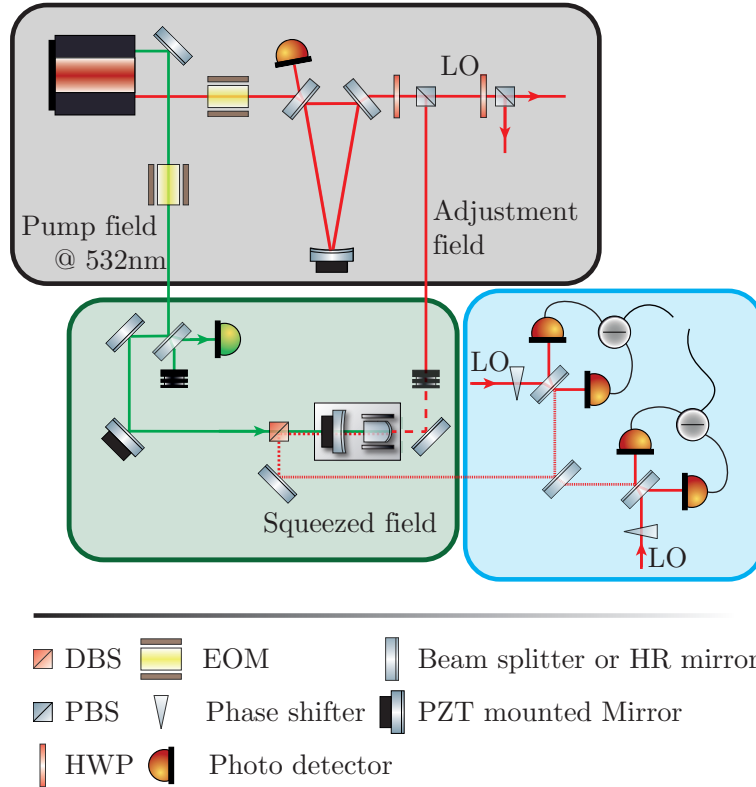
Figure 6.1: Setup for stabilized EHD without a bright light field. The setup includes the laser preparation (grey box), the squeezed light generation (green box) and the eight-port homodyne detector (blue box). Technical details and the stabilization schemes are given in the following sections.

beam serves as an adjustment field for the squeezed-light source. This field is not used for the measurements but practical to adjust the paths of the squeezed vacuum field.

6.2.2 The squeezed-light source

The squeezer design presented in Chapter 5 relies on a control field with a phase modulation to stabilize the length of the cavity. For this reason, a different type of squeezed-light source was used in comparison to the previous experiment.

The nonlinear medium is a *periodically poled potassium titanyl phosphate* (PP-KTP) crystal with the dimensions $2.5 \times 5 \times 6.5 \, \text{mm}^3$. The curved back side of the crystal with $r = 10 \, \text{mm}$ was HR coated for the fundamental and the pump field. The reflectivities for the coupling mirror where given by 89 % for the infrared and 97.5 % for the frequency doubled field. As the reflectivity for the pump field is

Figure 6.2: Setup of doubly resonant squeezed-light source. The green pump field is passing an EOM which imprints a phase modulation at $52\,\mathrm{MHz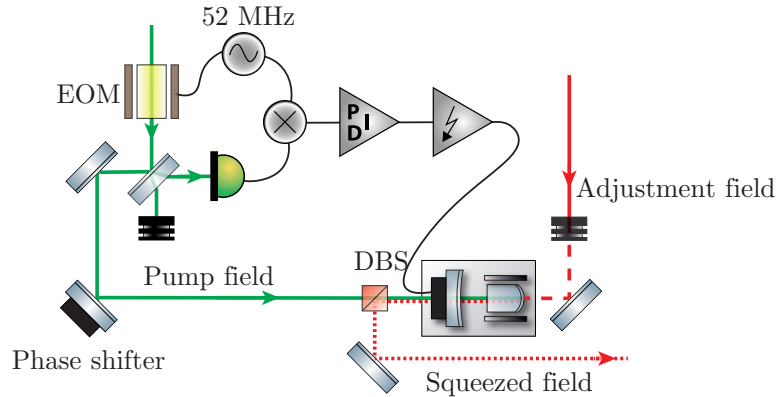}$ onto the light. A balanced beam splitter divides the field. While one output is directly dumped, the other part enters the squeezed-light resonator through the coupling mirror. As the squeezed-light resonator forms as well a cavity for the pump field, the reflected light, detected at the other output of the balanced beam splitter provides the error signal for a control loop. The signal is fed back to the PZT of the squeezing cavity to control its length. Careful temperature tuning ensures that the pump field and the infrared field are resonant and phase matched at the same time, enabling the squeezing process.

chosen significantly higher then for the resonator in Section 5.1.1, the hemilithic construction does not only form a cavity for the fundamental field but as well for the second harmonic field. The intracavity power of the pump field is therefore increased and the setup requires less incident pump power for strong squeezing generation. This so-called doubly resonant cavity design is already successfully implemented in several works, for instance in [83] where they provide a new squeezing record of $15\,\mathrm{dB}$ with this design.

6.2.3 Stabilization of the squeezed-light source with the pump field

The doubly resonant cavity has the additional advantage that no additional control field at $1064\,\mathrm{nm}$ is needed to stabilize the cavity length as this can be realized with the second harmonic field. A phase modulation is imprinted on the pump field with an EOM at $52\,\mathrm{MHz}$. The green light passes a balanced beam splitter, where the transmitted port is directed into a beam dump. The reflected part is sent to the squeezing resonator, transmits through a DBS and enters the cavity through the coupling mirror. The reflected light field of the cavity is divided as well on

the balanced beam splitter and the open port is used to implement a resonant photo detector. The length of the cavity is stabilized with the PDH scheme via the pump field as depicted in Fig. 6.2.

The temperature of the doubly resonant cavity needs to be chosen in such a way that the generated squeezed light field at 1064 nm and the pump field at 532 nm is resonant for the same cavity length. The optimal point which was closest to the "phase matching temperature" of the resonator (e.g. Section 3.1) was determined to be around 33 °C.

6.2.4 Characterization of the squeezed-light source

The squeezer is characterized with an additional path, guiding the squeezed light field directly onto one of the homodyne detectors. Via this short cut, a measurement of the squeezed light field for different pump powers is performed at a sideband frequency of 5 MHz using a resolution bandwidth (RBW) of 300 kHz and a video bandwidth (VBW) of 300 Hz. As the absorption of the pump field in the crystal changes its temperature significantly, the temperature needs to be optimized for every pump power to fulfill the double resonance and phase matching condition. The result is depicted in Fig. 6.3. The depicted variances are dark noise corrected and normalized to the vacuum variance. The dark noise clearance for this measurement was 14 dB.

The dark noise corrected values of the squeezed and anti-squeezed quadrature are used to estimate the total losses on the squeezing. The losses are consequently calculated to be about 7-8 % for this measurement. The losses are mainly dominated by the visibility between the signal field and the local oscillator in this path which is about 98 % and propagation losses. As some changes in the experimental setup were done between this measurement and following measurements presented in this section, the optical losses for the measurements are always given. The depicted data is fitted by the theoretical model that gives the expected squeezed and anti-squeezed variance in dependence of the optical losses and the pump power relative to the threshold, i.e. [84]. The calculated curves are as well shown in the figure as solid lines. The theoretical model was used to estimate the expected pump threshold of the squeezed-light source to be about $P_{\mathrm{th}} = 56 \, \mathrm{mW}$. It should however be mentioned that the mode matching of the pump beam to the squeezing resonator is only about 70 % due to a bad beam quality of the green pump. Therefore, all given pump powers need in principle to be corrected for the mode matching and multiplied by 0.7. This gives us the threshold value for the pump power in the correct mode to be about 39 mW. However, as these are just estimated values, the pump power values in Fig. 6.3 are the actual input powers.
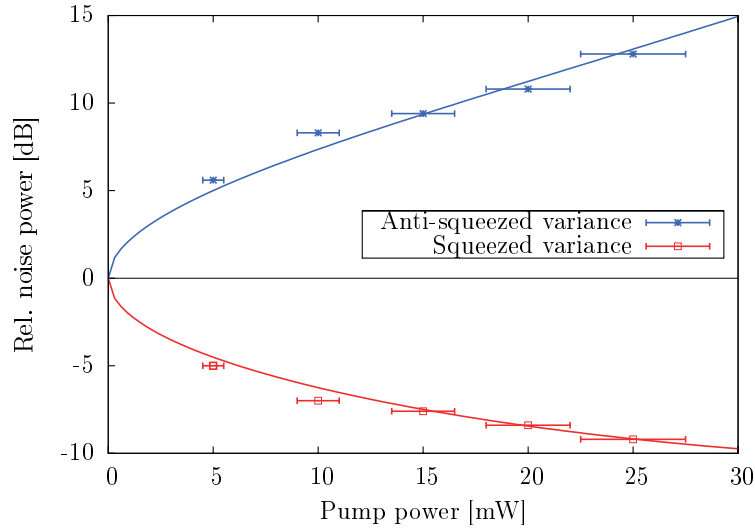
Figure 6.3: Dependence of squeezed and anti-squeezed variance in dB on the pump power in mW: For different pump powers the squeezed and anti-squeezed variance is detected directly on a balanced homodyne detector. The data is dark noise corrected and normalized to vacuum. The pump power is measured with a power meter whose accuracy is qualified by the error bars of 10 %. The measurement is performed at a sideband frequency of 5 MHz with a RBW of 300 kHz and a VBW of 300 Hz. The total losses on the squeezed light field are calculated to be about 7-8 %. The data shows a good agreement with the theoretical fit.

To determine the linewidth of the squeezer, a measurement of the squeezed and anti-squeezed variance over the frequency spectrum between 3 MHz and 200 MHz is performed. For this measurement 25 mW pump power entering the squeezing resonator is used and the local oscillator beam has a power of 15 mW before the BHD beam splitter. The dark noise corrected and vacuum normalized results are depicted in Fig. 6.4. The spectrum shows clearly the decrease of the squeezing and anti-squeezing towards higher frequencies. The spectrum is fitted as well with the model of the squeezed-light source, now in dependence of the sideband frequency. The fit gives an estimation for the linewidth of the squeezed-light source to 110 MHz(FWHM). The optical losses for this measurement are calculated to be 13.9 %. At a sideband frequency of 100 MHz a squeezing variance of 2 dB below vacuum variance is still visible. The measurement range up to 100 MHz seems reasonable for a squeezing or entanglement measurement.
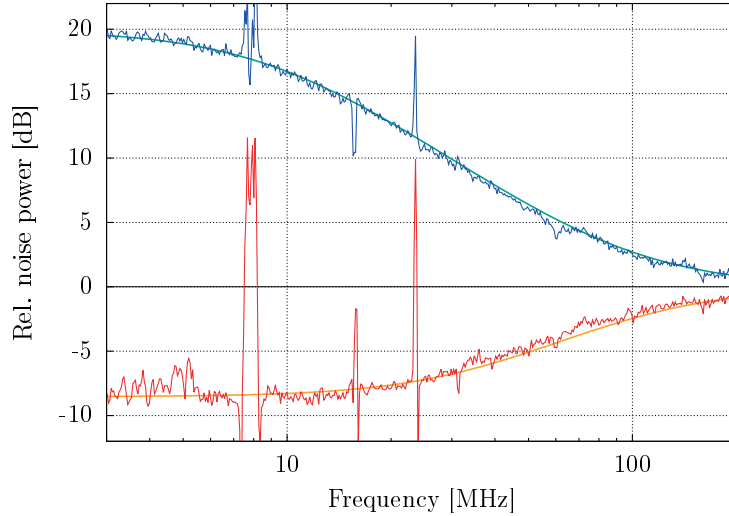
Figure 6.4: Vacuum normalized and dark noise corrected spectrum of the squeezed-light source. The measurement is performed with 25 mW pump power and 15 mW in the local oscillator path before the beam splitter. The measurement is performed over a spectrum from 3 MHz to 200 MHz with a RBW of 300 kHz and a VBW of 300 Hz. The spikes in the spectrum are external disturbance frequencies, that are picked up by the detector due to antenna effects. Improvements in the shielding of the cable and the BHD electronics can possibly avoid these pick-ups.The curves are fitted with a model of the squeezed-light source. The spectrum shows a good agreement with the theoretical model.

6.2.5 Characterization of the broadband homodyne detector

The experimental realization of distillation against phase noise, presented in the previous chapter, measures at a distinct sideband frequency of 6.4 MHz. In contrast, the detector for this setup, which shall be used for the distillation against optical losses, is not measuring frequency resolved but broadband over the whole measurement range. The homodyne detector thus needs to show a flat response and has to be sufficiently sensitive in this range. The concrete spectrum range will finally be defined by the filtering of the APD path. Note, that the filter cavities will just give an upper limit to the frequency range as the filter cavities only cut out an area around the center frequency. As determined from the linewidth of the squeezed-light source in the previous section, the frequency range for this experiment was set to 100 MHz. This ensures that enough squeezing is available over the whole range while it is still large enough to enable appropriate filter cavities for a future single photon path.

For the realization, a broadband homodyne detector design, originally designed
for gigahertz squeezing experiments, is used. The design was developed by Moritz
Mehmet and Stefan Ast, a detailed description can be found in [85,86]. To reduce
additional losses in the detection, the homodyne detectors use high efficiency
custom made InGaAs photo diodes with design quantum efficiencies of about
99 %. The photo diodes have 500 μm active area. This reduces the bandwidth
in comparison to the photo diodes of the original design, which have an active
area of 70 μm, but it is still fast enough for our desired measurement range. For
the eight-port homodyne detection both homodyne detectors are assumed to be
identical as they are used to reconstruct the quantum state. Differences in the
performance of the detectors would disturb this reconstruction, therefore the
response of both photo detectors should be identical over the whole measurement
spectrum as well.
To conclude, the detector for this experiment is an EHD with a flat spectrum that
is sensitive up to 100 MHz. The EHD consists of two BHD, that need to perform
identically over the whole frequency range to ensure a reliable reconstruction of
the state for all frequencies.

Fig. 6.5 shows the internal electronic noise (dark noise) and a vacuum measure-
ment for a local oscillator power of 15 mW for a spectrum from 3 MHz to 200 MHz.
Up to 100 MHz the spectrum has a dark noise clearance of 15 dB and is almost
flat over the whole range. Both detectors perform identically for the same LO
power of 15 mW. The decrease of the vacuum noise slightly before 100 MHz in-
dicates the limited bandwidth of the photo diodes. As the deviations are small,
this should still be sufficient in terms of flatness. The LO power of 15 mW before
the entanglement beam splitter was chosen for all measurements shown in this
chapter.

6.2.6 Phase stabilization of the measurement

First considerations

If we recall the previous setup of Chapter 5, we see that all points in the experi-
ment, where the relative phase of two beams to each other needs to be stabilized,
are depending on the control field that co-propagates with the squeezed vacuum.
Here, the experiment is not feasible with bright light fields which creates the need
to provide a different stabilization scheme.

There are three phases that need to be stabilized. First, there is the phase of
the pump field entering the cavity which defines the quadrature that is squeezed.
The other two phases that need to be controlled are the relative phases between
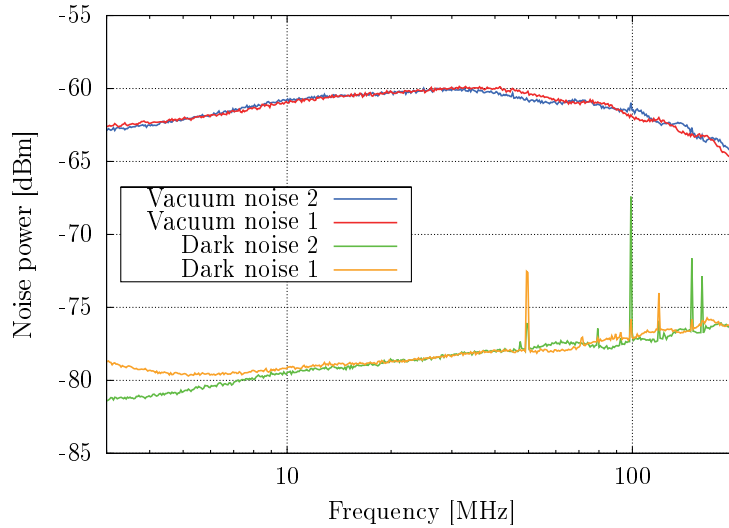
Figure 6.5: Comparison of the BHDs. Dark noise and vacuum noise of the two BHDs used for the EHD are shown in the frequency range from 3 MHz to 200 MHz. The curves are labeled with the number 1 and 2 corresponding to the respective BHD. Both detectors show almost the same dark noise and equal vacuum noises over the whole spectrum for 15 mW local oscillator power at each BHD. The peaks visible in the dark noise spectrums are electronic pick ups from PDH frequencies on the table. RBW: 300 kHz, VBW: 300 Hz, sweep time: 1.8 s, curves are averaged five times.

the LO and the signal fields on the homodyne detectors. These phases define the quadrature that is measured on the respective detector. Visually speaking, the pump phase causes a rotation of the ellipse in phase space while the local oscillator phase causes a rotation of the measurement axis relative to this phase. When a light field with an imprinted phase modulation is co-propagating with the squeezed vacuum, a phase reference is provided and these effects can be distinguished. If just a squeezed vacuum state is investigated the two phase shifts are indistinguishable. Note that drifts of the pump phase are seen on both BHD in the EHD scheme while changes in the local oscillator phase are just visible on the respective BHD.

As we need to stabilize the phases of both local oscillators independently of each other, the idea is to control only the local oscillator phases while the pump phase is drifting. As phase drifts are slow, the local oscillator phase can follow the phase of the pump as the two effects are indistinguishable.

To ensure the correct operation of the EHD it is important that both BHDs are stabilized orthogonally with respect to each other. This condition is satisfied if one BHD is stabilized to the squeezed quadrature with minimal variance while the other one is stabilized to the anti-squeezed quadrature with maximal variance,.
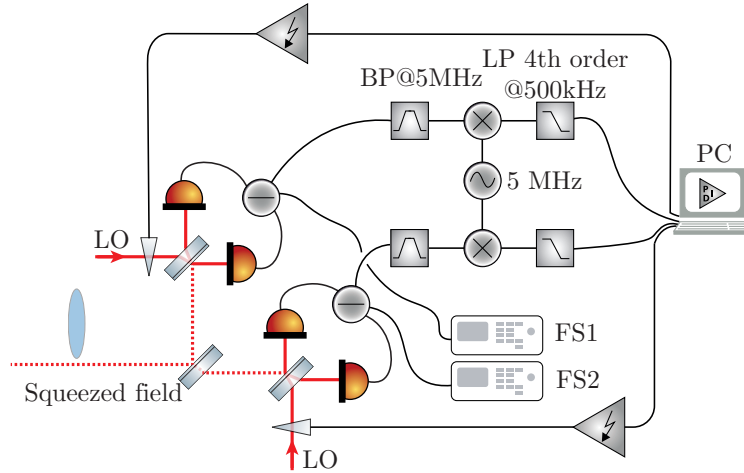
Figure 6.6: Stabilization scheme for the phases of the EHDs. The subtracted signals of the homodyne detectors are bandpass filtered at 5 MHz, mixed with an electronic LO at 5 MHz and lowpass filtered consequently with a 4th order lowpass at 500 kHz. The filtered signal is sent to a computer and converted to a digital signal with ADCs. A LabView program generates an error signal for both homodyne detectors to stabilize them orthogonally. The feedback signal is amplified by an HV amplifier and directed to phase shifters in the LO paths.

Even a rotating squeezing ellipse does not destroy the orthogonality, since the locks ensure that the readout axis will be rotated by the same amount, resulting in a constant 90° phase shift between the detectors.

In this section such a method to stabilize on the maximal or minimal variance is presented.

Stabilization with digital feedback

The method for the stabilization of the phases is based on a not yet published digital locking scheme from Axel Schönbeck and was developed in close cooperation with him. The aim of this lock is to stabilize the measurement axes of the homodyne detectors along the main axis of the squeezing ellipse.
Even though the EHD imposes 50 % loss on the squeezed state, some squeezing is still present at both detectors. An aligned squeezing ellipse means that one detector measures anti-squeezing and the other detector measures the squeezed quadrature. Thus, the readout phase of the LOs are stabilized to the maximal variance on one detector and to the minimal one on the other detector.

The experimental setup is depicted in Fig. 6.6. The AC signals of the BHDs

are directed to custom-made electronic circuits, that provide a duplicate af the input. This duplicates each are directed to a spectrum analyzer for monitoring of the state. As the impedance matching of these circuits is not perfect over the whole frequency range, the dark noise of the duplicated signals are slightly affected for high frequencies. The signal itself is bandpass filtered at 5 MHz. This frequency was chosen because we expect high squeezing levels in this range due to the previous direct measurements of the squeezed light. The signal is then mixed with an electronic LO at 5 MHz and lowpass filtered with a 4th order lowpass at 500 kHz to get a DC signal. This signal is in principle now a voltage stream from which the variance of the signal field can be calculated. The filtered signals are directed to an *analog digital converter* (ADC) and simultaneously measured by a data acquisition card *PCI 6259* from *National Instruments* with a sample rate of 500 kHz. The feedback signal is converted by the AD converter to an analog signal, amplified in a HV amplifier and feedback to the phase shifters in the local oscillator paths.

The program that creates and processes the error signal and provides the feedback signal is written in LabView and the single steps for the loop are shortly sketched in the following.

Preparation of the program The program takes chunks of k samples of the raw data from which the variance of the data set is determined. During all measurements presented, the chunk size was chosen to be $k = 3000$. To give an unbiased interface for the comparison of both detectors, the variances are normalized to vacuum. This is realized by a preliminary measurement of vacuum where the averaged variance is locally stored in the program. To determine the maximal and minimal variances for the setpoints of the control loop the phases of both homodyne detectors are shifted continuously. If all parameters are defined, the control loop can be started.

Obtain variances and PI controller For the actual control loop, the phases are no longer scanned. From the raw data set of length k the actual variance of the squeezed vacuum field on the detector is calculated and vacuum normalized. This denotes the actual value for our control loop. The actual value and the previous obtained setpoint are fed to a PI controller which is an implemented routine of Labview. The output signal cannot serve directly as an error signal. As the stabilization is performed on a maximum or minimum, the sign of the error signal needs to be determined in an additional step.

Obtain the sign for the feedback signal To determine if the voltage at the PZT has to be increased or decreased to reach the setpoint and correct for external disturbances, we compare the actual value of the variance of measurement

m with the previous measured variance of measurement $m - 1$. If the calculated variance of measurement m is further away from the setpoint than the variance of measurement $m - 1$, the sign of the feedback signal needs to be inverted as the voltage was corrected to the wrong direction. For the stabilization on the anti-squeezing, this means explicitly $\mathrm{Var}(m) < \mathrm{Var}(m - 1)$ and analog for the stabilization on the squeezed quadrature $\mathrm{Var}(m) > \mathrm{Var}(m - 1)$.

As one comparison would be to vulnerable to small fluctuations in the variance, the amount of comparisons is determined to 3. Only if the variance decreased (or increased) for the last three rounds of the control loop on the anti-squeezed (or squeezed) quadrature, the sign of the feedback signal is inverted.

Feedback to the phase shifters in the local oscillator paths The feedback signals are converted with digital analog converters and amplified by HV amplifiers. This signal is fed back to the phase shifters, controlling the phases of the LO fields.

Performance of the digital control loop

The digital control loop stabilizes the phases of the homodyne detectors. The digital loop frequency is about 120 Hz, which gives the maximum disturbance frequency that can be compensated for by the loop. The loop frequency is mainly limited by the speed of the data acquisition card which is 500 kHz per channel at maximum. As 3000 samples per loop are acquired, simply the data acquisition for the variance calculation limits the loop frequency to $500\,\mathrm{kHz}/3000 \simeq 166\,\mathrm{Hz}$. Additionally, disturbances that occur randomly are observed. The origin of these disturbances has not been identified yet. As the disturbances are as well present when the locking scheme is applied on a different experimental setup, the problem needs to be in the locking scheme itself and not e.g. in the electronics of the homodyne detector. Possible reasons can be problems with the conversion between analog and digital signals either at the input or at the output side. As the disturbances occur randomly, the measurements presented in this chapter could be acquired in the disturbance free breaks. The measurement results are thus not affected by this problem.

6.3 Measurement with the stabilized EHD

In this section the measurement results of a stabilized measurement of squeezed vacuum with the eight-port homodyne detector are presented. For this measurement, no control field is co-propagating with the squeezed vacuum and the phases of the homodyne detectors are controlled with the digital locking scheme. The shifts of the pump phase of the squeezed-light source are not controlled for this

measurement but compensated for by the control loops of the homodyne detectors which are following the slow drifts of the pump phase.

The measurement is performed in such a way that both detectors are monitored at the same time with two different spectrum analyzers. BHD1, which is stabilized to the squeezing quadrature is measured with spectrum analyzer 1 (FS1) while BHD2, which is measuring the anti-squeezed quadrature of the mode is readout with spectrum analyzer 2 (FS2), both devices from R&S. This procedure enables the simultaneous detection of both fields but causes different absolute values as the electronic noise of the spectrum analyzers is different. Thus, we indicate for all measurements that are presented which device has been used, given by the additional abbreviation "FS1" or "FS2" respectively.

6.3.1 Measurement at a sideband frequency of 5 MHz

Both balanced homodyne detectors measured simultaneously at a sideband frequency of 5 MHz. The RBW and VBW of both spectrum analyzers were set to 300 kHz and 300 Hz and the sweep time was set to 300 ms. To allow for an exact comparison, both measurements are normalized to vacuum. The squeezed quadrature shows a variance which is 2.2 dB below the vacuum variance while the anti-squeezed quadrature shows a variance of 14.2 dB above the vacuum variance. The dark noise of the corresponding detector was 17.2 dB below vacuum for the squeezing measurement and 17.7 dB below vacuum for the anti-squeezing measurement. If we correct for dark noise, the squeezed variance is increased to 2.3 dB noise suppression, the anti-squeezed variance does not change under dark noise correction due to the larger dark noise clearance. Both curves were measured with stabilized phases.

Additionally a measurement of the scanned phases was saved, shown by the violet graph, obtained by the detector 1 and monitored with the FS1 and the light-blue graph, measured with detector 2 and monitored with the FS2. This scanned measurements are as well normalized to vacuum. One can see that both scanned variances show the same maximal and minimal variance and that these variances are equal to the variances of the stabilized measurement. This tells us on one hand, that the detectors were indeed stabilized to the maximal and minimal quadratures. Moreover it indicates that the measured state is identical at both detectors which is one of the restrictions we needed to fulfill for the reconstruction.

6.3.2 Reconstruction of the state

The measurement presented in Fig. 6.7 shows the measurement of the state with the eight-port homodyne detector. This measurement is affected by the vacuum
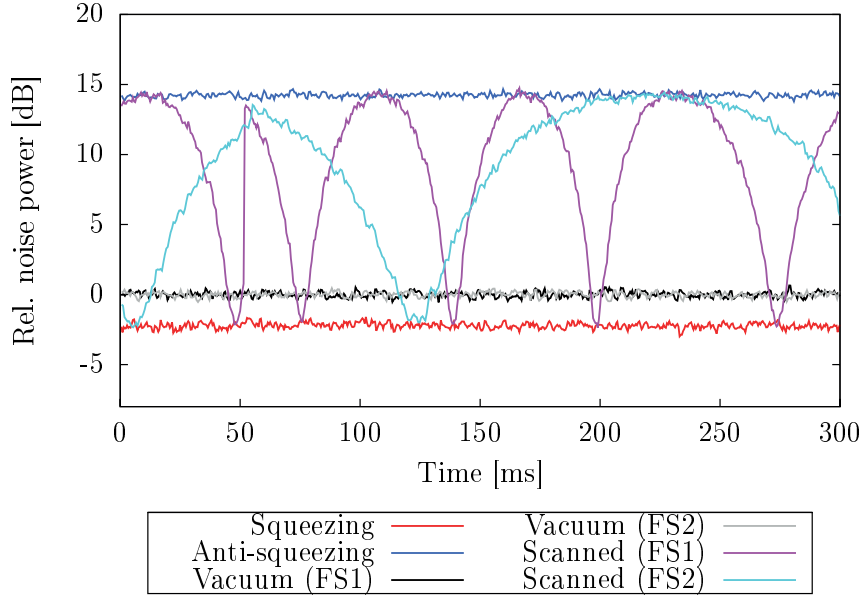
Figure 6.7: Simultaneous measurement of the squeezed vacuum state with the eight-port homodyne detector. The measurement is performed at a sideband frequency of 5 MHz with a RBW of 300 kHz, a VBW of 300 Hz and a sweep time of 300 ms. The squeezed variance (red) is measured with FS1 while the anti-squeezed variance (blue) is measured with FS2. Both curves are normalized to the vacuum variance of the detectors (black and grey). The squeezed variance is 2.2 dB below the vacuum variance, the anti-squeezed variance is 14.2 dB above the vacuum level. The dark noise clearance was 17.2 dB for the FS1 measurement and 17.7 dB for the FS2 measurement. The violet and light-blue graphs show the measured variances at the detectors with continuously shifted LO phases.

port of the EHD, which introduces 50 % loss to each measured state. As described in Section 3.2.3 the state in front of the beam splitter can be reconstructed by Eq. (3.3). In this measurement we can not access the whole covariance matrix as the spectrum analyzers directly determine the variances. For a reconstruction of the covariance matrix the raw data is needed to calculate the cross correlations. However the reconstruction of the individual quadrature variances works just equally well and the variance before the beam splitter can be calculated by

$$\mathrm{Var}(X(\vartheta)\,)_\mathrm{sig} = 2\mathrm{Var}(X(\vartheta)\,)_\mathrm{EHD} - 1 \ . \tag{6.1}$$

This procedure can be seen in such a way that it gives the squeezing before the 50 % losses occur. The losses of the directly measured state can be calculated to be 59.6 % using Eq. (2.50), which corresponds to an initial lossless squeezing value
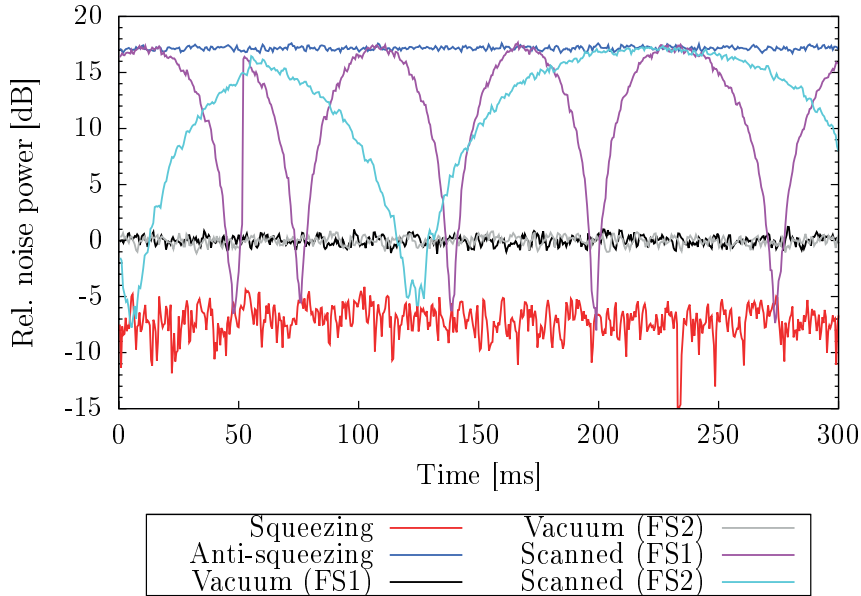
Figure 6.8: Reconstruction of the squeezed vacuum state in front of the EHD beam splitter. This figure presents the original entanglement in front of the beam splitter and is calculated from the results of the reconstruction of the data presented in Fig. 6.7 using Eq. (6.1). The color coding is identical to the previous figure. With the reconstruction, a squeezed variance of 7.0 dB below vacuum and an anti-squeezed variance of 17.2 dB was obtained.

of 18 dB. If we exclude the losses of the beam splitter we would expect

$$\epsilon_{\text{withoutBS}} = 1 - \left(\frac{\eta_{\text{EHD}}}{\eta_{\text{BS}}} \right) = 0.1924 \ ,$$

which is an estimate for the remaining losses on the state without the 50 % loss of the EHD beam splitter.

Please note that this calculation is just a rough estimation for low squeezing parameters as the changes in the variances of squeezed and anti-squeezed quadrature for different losses are smaller for small squeezing values then for strong squeezing values. Using Eq. (6.1), the variances in front of the beam splitter are calculated. The result is presented in Fig. 6.8. The squeezed variance of the signal field was calculated to be 7.0 dB below the vacuum reference and the anti-squeezed variance to be 17.2 dB above vacuum. Compared to Fig. 6.7, the curves for squeezing and vacuum become more noisy while the noise in the anti-squeezed quadrature remains nearly the same. This is related to the fact that smaller variances are more sensible to the reconstruction than larger variances. A measurement with
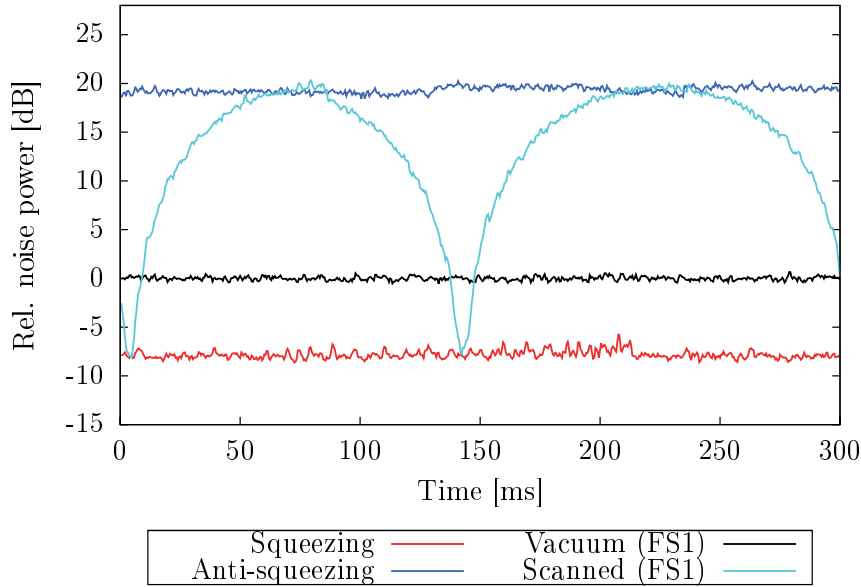
Figure 6.9: Squeezing measurement at BHD1 via shortcut. To compare the quality of the reconstructed variances, the squeezed state is directly measured on detector 1. The squeezed variance is 7.8 dB below vacuum, 8.3 dB if the value is dark noise corrected. The anti-squeezed variance is 19.3 dB above vacuum, 19.4 dB if dark noise corrected. The light-blue data showed the variance for a scanned local oscillator phase. Sideband frequency: 5 MHz, RBW: 300 kHz, VBW: 300 Hz, sweep time: 300 ms, dark noise clearance: 17.2 dB. The measurement is vacuum normalized.

the EHD with higher VBW would provide a higher averaging factor which would make the graphs more smooth.

To have a benchmark for the quality of this reconstruction, a measurement of the squeezed vacuum via the shortcut is taken where the squeezed and anti-squeezed variance is measured one after the other on BHD1 and monitored on the FS1. The measurements are as well stabilized with the control loop. The result is shown in Fig. 6.9. With the direct measurement of both variances on detector 1 without the EHD beam splitter, the squeezed variance is 7.8 dB below vacuum and the anti-squeezed variance is 19.3 dB above vacuum. From this values, the total loss on this squeezing measurement is calculated to be 13.9 % with an initial squeezing of 20 dB. The different loss compared to the before presented EHD measurement is explained by the different propagation paths of the signal in the shortcut compared to the signal path in the EHD measurement. As well the mode overlap of the signal beam with the local oscillator on the BHD was slightly different for this measurement. The higher initial squeezing can be explained by
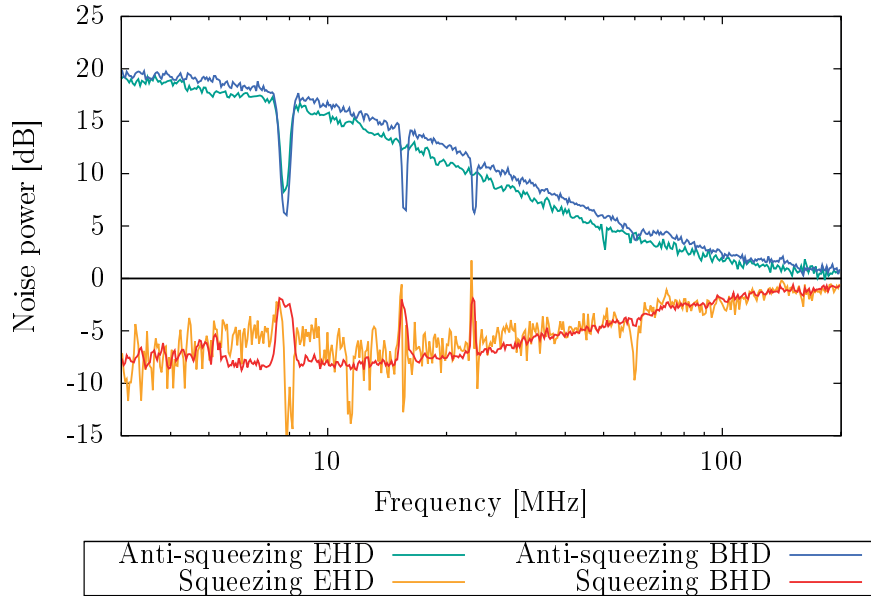
Figure 6.10: Comparison of the directly measured spectrum with the reconstructed spectrum. The blue and red traces give the result for the direct measurement of the squeezed state on BHD 1 via the shortcut. The green and orange traces show the reconstructed spectrum from the EHD measurement, corrected for the 50 % loss. Frequency range: $3 - 200\,\mathrm{MHz}$, RBW: $300\,\mathrm{kHz}$, VBW: $300\,\mathrm{Hz}$, sweep time: $1.8\,\mathrm{s}$, LO power per BHD: $15\,\mathrm{mW}$. The measurement is vacuum normalized but not dark noise corrected.

the fact that the measurement via the shortcut and the EHD measurement were taken one after the other. Between this two measurement runs the squeezed light resonator needed to be restabilized which resulted in the different initial squeezing values. Within this differences the reconstructed variances are quite close to the directly measured variances. This indicates, that the reconstruction of the state is working for the sideband frequency of $5\,\mathrm{MHz}$. With identical losses and initial squeezing, the reconstruction can in principle be perfect. If the losses would be reduced to be below $10\,\%$, e.g. by optimizing the mode overlap at the BHDs, more then $10\,\mathrm{dB}$ squeezing are to be expected in the directly measured squeezed variance and in the reconstructed squeezed variance.

To verify if the locking and reconstruction scheme is also working with different frequencies and not only at the lock frequency, the spectrum between $3\,\mathrm{MHz}$ and $200\,\mathrm{MHz}$ was measured. The homodyne detectors are stabilized to the same quadratures as before and as well monitored with the same spectrum analyzers. Additionally, a direct measurement of the spectrum of the squeezed state is obtained with BHD1 to have a benchmark for the performance.

113

In Fig. 6.10, the comparison between the directly measured spectrum and the spectrum of the reconstructed variances in front of the EHD is shown. The directly measured squeezing and anti-squeezing spectrum is shown in red and blue while the reconstructed spectrum is shown in green for the anti-squeezing and orange for the squeezing. As this measurements are taken simultaneously to the measurements at 5 MHz, the losses and initial squeezing values are identical to the values of the previous shown measurement. Thus, the directly measured anti-squeezing is higher than the reconstructed anti-squeezing due to the higher initial squeezing value. This effect is less visible in the squeezing spectrum due to the smaller dark noise clearance. Equivalent to the 5 MHz measurement, the reconstructed squeezing is more noisy in comparison to the directly measured squeezing. The good agreement of both measurements is however visible over the whole spectrum. This result confirms, that a reconstruction of the squeezed state is working for the whole frequency range. This was the last step that needed to be proven to make the setup suitable for the emulated distillation against optical loss. To conclude, sufficient squeezing strength are available in the complete spectrum range, the BHDs are flat and sensitive in this range and the reconstruction of the state with the EHD works over the whole spectrum range. The whole setup is stabilized without bright light field co-propagating with the squeezed vacuum field. All this are necessary prerequisites for the emulated distillation where the setup includes a non-Gaussian operation in form of single photon subtraction realized with an APD.

6.4 Conclusion and Outlook

In this chapter the stabilized measurement of a squeezed state with an eight-port homodyne detector is presented without the need of a bright light field that co-propagates with the squeezed vacuum. We motivated why such a stabilization scheme is necessary for a distillation protocol which is capable to distill against optical loss. As the distillation against optical loss requires the implementation of single photon detectors, any bright light fields in the squeezing path have to be avoided. We highlighted as well the need for a careful frequency range choice and demonstrated the properties and suitability of the squeezing source and homodyne detector used in this setup.

A stabilization scheme for the phases is presented which relies on the stabilization to maximal or minimal variance of the measured state. Using this stabilization scheme, a measurement at 5 MHz and a spectrum measurement is performed with the eight-port homodyne detector. The performance of this measurement is compared with a direct measurement of the squeezed state on one homodyne
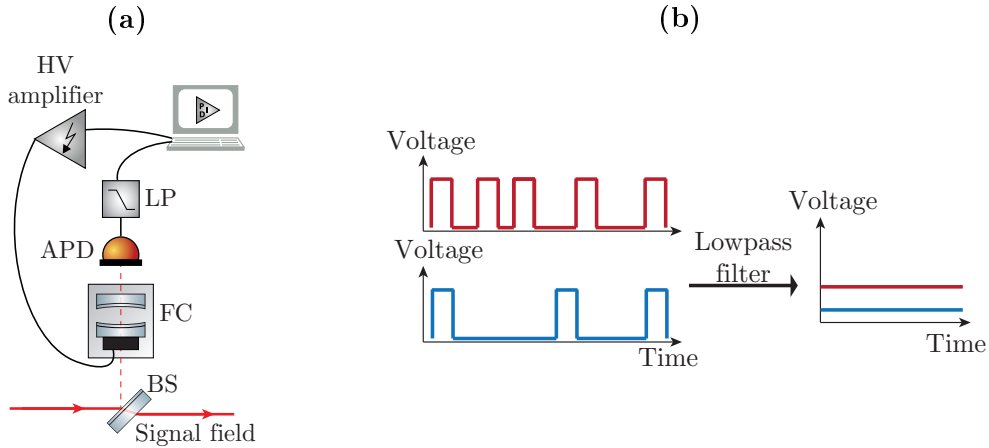
(a)

(b)

Figure 6.11: (a) Schematic setup for digital locking of a filter cavity on maximum APD event rate. The filter cavity serves to reduce the detection range of the APD to the desired measurement range of the experiment. The lowpass filtered event rate of the APD, approximately given by a DC signal can be used as an input signal for the digital locking scheme, analogous to the digital locking on maximal or minimal variance. (b) Schematic how the control signal can be obtained from the event rate. Each event gives a rectangular voltage peak of defined height and width. Lowpass filtering of the data stream will result in a DC level proportional to the event rate.

detector. The measurement results show that the eight-port homodyne detector can reconstruct the original squeezed state over the whole measurement range and is therefore suitable for a future distillation experiment.

The stabilization scheme presented in this chapter can directly be applied to *v-class entangled states* [59]. This special class of entangled states, which is prepared by the overlap of a squeezed state with vacuum shows asymmetric variances. The stabilization on maximal and minimal variance is thus possible and the control loop can be easily extended to a second EHD.

The digital locking scheme can be applied as well for other stabilizations where no bright light field is involved but a variable has to be stabilized to an extremal point. This can e.g. be used in the potential single photon path. To realize the conditioning on single photon subtraction, a beam splitter with very low reflectivity would need to be implemented in the signal path. As mentioned in Section 6.1.1, the path for the single photon detector needs additional filtering to match the measurement range of the setting. This can be realized by a filter cavity with suitable linewidth and free spectral range. As no bright light field is present in

this path, the PDH stabilization schemes can not be used to control the length of this cavity. However, the cavity is on resonance if the event rate of the APD is maximized. This can be used as the starting point for a modified version of the digital locking scheme, depicted in Fig. 6.11, which works as explained in the following.

For every event detected by the APD, the output will be a constant voltage peak of distinct width. Roughly spoken, the output can be seen as an rectangular function with a irregular frequency correlated to the event rate. Appropriate lowpass filtering of this output signal will thus give a DC voltage level which is proportional to the event rate of the detector. Analogous to the variance stabilization, the maximal level can be determined by scanning the length of the filter cavity. This level will define the set point and the lowpass filtered APD signal will serve as the input of the control loop. This will provide a convenient way to stabilize the length of the filter cavities. In previous experiments, the filter cavities are e.g. not stabilized but hold on resonance by hand [87] or the stabilization is performed with an optical chopper [88]. The optical chopper works such that the filter cavities are stabilized with a bright light field, co-propagating with the signal field in only parts of the time. This stabilization periods are alternating with measurement periods in between without stabilized filter cavity. Compared to these methods, the proposed digital locking provides a promising stabilization scheme that is convenient to implement and long time stable.

CHAPTER 7

Conclusion and Outlook

Entanglement is an important resource for present quantum information protocols and finds usage in e.g. quantum key distribution protocols. For this, entanglement has to be distributed between distant parties. During transmission, e.g. over fibers, entangled states are unavoidably exposed to optical loss and phase noise which reduce the entanglement or even completely demolish it. Iterative entanglement distillation protocols provide a promising tool to overcome these issues. However, iterative protocols are usually inefficient due to small success rates and are experimentally not realizable for larger numbers of iterations. Quantum memories have been proposed to make these protocols feasible again but appropriate quantum memories are not realized to date.

The proposal for emulated distillation by Jaromír Fiurášek and Nicolas Cerf provides a different solution to the problem that works without the need of quantum memories. The idea of this proposal is to replace the actual physical implementation of the iterative distillation process by a suitable postprocessing of measurement data. This allows the copies to be successively measured in contrast to standard iterative distillation protocols where all copies must be simultaneously available. Emulated distillation therefore facilitates a more compact setup and at the same time increases the success probability in comparison to a direct experimental realization without quantum memories.

The no-go theorem constitutes, that it is not possible to distill Gaussian states with only Gaussian methods. Based on this theorem, the content of this thesis can be separated in two parts. The first one covered the experimental demonstration of emulated entanglement distillation on phase diffused states. As phase noise

degaussifies the states, the no-go theorem admits the distillation against phase noise with Gaussian methods only. In the second part, we examined the necessary changes in the experimental techniques for distillation of Gaussian states since the implementation of a non-Gaussian operation is there required in the distillation process.

In detail, we presented the general scheme of an iterative distillation protocol and the proposal of Jaromír Fiurášek and Nicolas Cerf to perform such a protocol in the postprocessing. We investigated the performance of the protocol in the asymptotic limit and considered two different distillation conditions that lead both to a distillation, purification and Gaussification of the data.

Utilizing this theoretical approach, the full iterative protocol was experimentally realized with a compact setup, consisting of a two-mode-squeezed vacuum source and two eight-port homodyne detectors. The entangled states were intentionally degaussified by introducing phase noise to mimic the transmission e.g. through a noisy fiber. We presented the experimental realization of the emulated distillation protocol on several sets of 10^7 data points where the states were exposed to different phase noise strengths. Moreover we performed the iterative distillation protocol for up to three iterations on a data set consisting of $5 \cdot 10^8$ data points. The improvement of the entanglement on the basis of the PPT value μ was shown, indicating clearly the successful distillation. Furthermore we presented the improvement of the Gaussian purity and Gaussianity of the distilled data. We underlined the improvement through higher iterations of the distillation protocol in terms of success probability and compared the two different distillation conditions that can be applied to the data.

To enable distillation as well on Gaussian states, e.g. to counteract the decrease of entanglement due to optical loss, a non-Gaussian operation needs to be introduced into the experimental setup. Single photon detectors like APDs can perform these non-Gaussian operations e.g. by single photon subtraction. However, APDs require the capability to measure over a broad frequency range and pose the need to avoid all bright light fields as they are damageable by already small light powers.

In the second experiment, a test setup was demonstrated that addresses these problems. In detail we presented the characterization of a suited squeezed-light source and appropriate BHDs. The squeezed-light source showed a linewidth of 110 MHz which allows squeezing of at least 2 dB up to a sideband frequency of 100 MHz. The EHD provided an almost flat vacuum noise in this range and the two individual BHD performed identically. The stabilizations of the squeezed-light source and the phases at the EHD were realized without the need of a bright light

field co-propagating with the squeezed vacuum field. Adressing the problem of the bright light fields, the whole setup was realized without the need of a bright light field co-propagating with the signal field.

With this setup, a stabilized measurement of a squeezed vacuum state was presented. We showed the successful reconstruction of the state with the EHD and compared it with a direct measurement of the squeezed vacuum state on a BHD. The reconstruction was in good agreement with the directly measured state in the complete frequency range between 3 MHz and 200 MHz. As an outlook towards the implementation of single photon detectors we provided as well a scheme to stabilize the necessary filter resonators in the single photon path with the digital locking scheme.

Regarding the goal towards entanglement distillation against optical loss, the presented setup and techniques can be easily extended to v-class entangled states. On the data set, obtained by such a setup, the emulated distillation protocol as presented in the other experiment can be performed which would provide the measurement result of a distilled and highly Gaussian state.

Both experiments complement each other and explore the possibilities to implement efficient iterative distillation without the need of quantum memories. Emulated distillation paves the way for efficient future quantum communication protocols.

APPENDIX A

Theoretical supplement

A.1 Symmetric covariance matrix under phase noise

The covariance matrix of a perfect entangled two-mode-squeezed state with squeezing parameter r is given by

$$\gamma = \begin{pmatrix} \cosh(2r) & 0 & \sinh(2r) & 0 \\ 0 & \cosh(2r) & 0 & -\sinh(2r) \\ \sinh(2r) & 0 & \cosh(2r) & 0 \\ 0 & -\sinh(2r) & 0 & \cosh(2r) \end{pmatrix} = \begin{pmatrix} a & 0 & b & 0 \\ 0 & a & 0 & -b \\ b & 0 & a & 0 \\ 0 & -b & 0 & a \end{pmatrix}.$$

Let us assume that mode one and mode two are rotated by the angles θ_1 and θ_2 respectively, given by the transformation

$$S_{\mathrm{rot}}(\theta) = \begin{pmatrix} \cos(\theta_1) & \sin(\theta_1) & 0 & 0 \\ -\sin(\theta_1) & \cos(\theta_1) & 0 & 0 \\ 0 & 0 & \cos(\theta_2) & \sin(\theta_2) \\ 0 & 0 & -\sin(\theta_2) & \cos(\theta_2) \end{pmatrix} = \begin{pmatrix} c_1 & s_1 & 0 & 0 \\ -s_1 & c_1 & 0 & 0 \\ 0 & 0 & c_2 & s_2 \\ 0 & 0 & -s_2 & c_2 \end{pmatrix}.$$

To ease reading (and writing) of the equations, we implement here the abbreviated form $\cos(\theta_1) = c_1$, $\cos(\theta_2) = c_2$ and so on. The rotated covariance matrix γ' is

given by

$$\gamma' = S\gamma S^T$$

$$= S \begin{pmatrix} c_1 a & -s_1 a & c_2 b & -s_2 b \\ s_1 a & c_1 a & -s_2 b & -c_2 b \\ c_1 b & -s_1 b & c_2 a & -s_2 a \\ -s_1 b & -c_1 b & s_2 a & c_2 a \end{pmatrix}$$

$$= \begin{pmatrix} c_1^2 a + s_1^2 a & -s_1 c_1 a + c_1 s_1 a & c_1 c_2 b - s_1 s_2 b & -c_1 s_2 b - s_1 c_2 b \\ -s_1 c_1 a + s_1 c_1 a & s_1^2 a + c_1^2 a & -s_1 c_2 b - c_1 s_2 b & s_1 s_2 b - c_1 c_2 b \\ c_1 c_2 b - s_1 s_2 b & -s_1 c_2 b - c_1 s_2 b & c_2^2 a + s_2^2 a & -s_2 c_2 a + c_2 s_2 a \\ -c_1 s_2 b - s_1 c_2 b & s_1 s_2 b - c_1 c_2 b & -s_2 c_2 a + s_2 c_2 a & s_2^2 a + c_2^2 a \end{pmatrix}$$

$$= \begin{pmatrix} a & 0 & c_1 c_2 b - s_1 s_2 b & -(c_1 s_2 b + s_1 c_2 b) \\ 0 & a & -(s_1 c_2 b + c_1 s_2 b) & s_1 s_2 b - c_1 c_2 b \\ c_1 c_2 b - s_1 s_2 b & -(s_1 c_2 b + c_1 s_2 b) & a & 0 \\ -(c_1 s_2 b + s_1 c_2 b) & s_1 s_2 b - c_1 c_2 b & 0 & a \end{pmatrix} .$$

$$\text{(A.1)}$$

From this it is clear to see that each mode by itself is invariant to rotation as it is in a thermal state. The parameter a is not affected by phase noise. However the off-diagonal elements show significant reactions. Assuming symmetric phase noise, $\langle \sin \phi_A \rangle_\Phi = \langle \sin \phi_B \rangle_\Phi = 0$ is given. If we assume in addition that the phase noise is uncorrelated, also $\langle \sin \phi_A \sin \phi_B \rangle_\Phi = 0$ holds. Using this, the statistical averaging over random phase diffusions of Eq. (A.1) simplifies to

$$\gamma_{PN} = \begin{pmatrix} a & 0 & \langle c_1 c_2 \rangle_\Phi b & 0 \\ 0 & a & 0 & -\langle c_1 c_2 \rangle_\Phi b \\ \langle c_1 c_2 \rangle_\Phi b & 0 & a & 0 \\ 0 & -\langle c_1 c_2 \rangle_\Phi b & 0 & a \end{pmatrix} = \begin{pmatrix} a & 0 & qb & 0 \\ 0 & a & 0 & -qb \\ qb & 0 & a & 0 \\ 0 & -qb & 0 & a \end{pmatrix}$$

where $q = \langle \cos(\theta_1) \cos(\theta_2) \rangle_\Phi$. This is exactly the formula provided in Section 2.4.2.

A.2 Estimation of the dephasing parameter from the covariance matrix

Let us start with the covariance matrix of the two-mode state without coherent displacement given by

$$\gamma = \begin{pmatrix} \langle \hat{X}_1^2 \rangle & 1/2(\langle \hat{X}_1 \hat{P}_1 \rangle + \langle \hat{P}_1 \hat{X}_1 \rangle) & \langle \hat{X}_1 \hat{X}_2 \rangle & \langle \hat{X}_1 \hat{P}_2 \rangle \\ & \langle \hat{P}_1^2 \rangle & \langle \hat{P}_1 \hat{X}_2 \rangle & \langle \hat{P}_1 \hat{P}_2 \rangle \\ & & \langle \hat{X}_2^2 \rangle & 1/2(\langle \hat{X}_2 \hat{P}_2 \rangle + \langle \hat{P}_2 \hat{X}_2 \rangle) \\ & & & \langle \hat{P}_2^2 \rangle \end{pmatrix} .$$

Due to symmetry of the covariance matrix, we display again only on the upper half of the matrix. If we apply the phase rotation to this more general covariance matrix we obtain rather lengthy equations. We name the elements of the rotated and diffused covariance matrix the following:

$$\gamma'_{\mathrm{PN}} = \langle S\gamma S^T\rangle_\Phi$$
$$= \begin{pmatrix} \langle \hat{X}_1^2\rangle_\Phi & 1/2\langle\langle \hat{X}_1\hat{P}_1\rangle + \langle \hat{P}_1\hat{X}_1\rangle\rangle_\Phi & \langle \hat{X}_1\hat{X}_2\rangle_\Phi & \langle \hat{X}_1\hat{P}_2\rangle_\Phi \\ & \langle \hat{P}_1^2\rangle_\Phi & \langle \hat{P}_1\hat{X}_2\rangle_\Phi & \langle \hat{P}_1\hat{P}_2\rangle_\Phi \\ & & \langle \hat{X}_2^2\rangle_\Phi & 1/2\langle\langle \hat{X}_2\hat{P}_2\rangle + \langle \hat{P}_2\hat{X}_2\rangle\rangle_\Phi \\ & & & \langle \hat{P}_2^2\rangle_\Phi \end{pmatrix}.$$

The entries of the covariance matrix are then given for the diffused state by:

$$\langle \hat{X}_1^2\rangle_\Phi = \langle \hat{X}_1^2\rangle\langle c_1^2\rangle_\Phi + \langle(\hat{X}_1\hat{P}_1 + \hat{P}_1\hat{X}_1)\rangle\langle c_1 s_1\rangle_\Phi + \langle \hat{P}_1^2\rangle\langle s_1^2\rangle_\Phi$$

$$\langle \hat{P}_1^2\rangle_\Phi = \langle \hat{X}_1^2\rangle\langle s_1^2\rangle_\Phi - \langle(\hat{X}_1\hat{P}_1 + \hat{P}_1\hat{X}_1)\rangle\langle c_1 s_1\rangle_\Phi + \langle \hat{P}_1^2\rangle\langle c_1^2\rangle_\Phi$$

$$\langle \hat{X}_2^2\rangle_\Phi = \langle \hat{X}_2^2\rangle\langle c_2^2\rangle_\Phi + \langle(\hat{X}_2\hat{P}_2 + \hat{P}_2\hat{X}_2)\rangle\langle c_2 s_2\rangle_\Phi + \langle \hat{P}_2^2\rangle\langle s_2^2\rangle_\Phi$$

$$\langle \hat{P}_2^2\rangle_\Phi = \langle \hat{X}_2^2\rangle\langle s_2^2\rangle_\Phi - \langle(\hat{X}_2\hat{P}_2 + \hat{P}_2\hat{X}_2)\rangle\langle c_2 s_2\rangle_\Phi + \langle \hat{P}_2^2\rangle\langle c_2^2\rangle_\Phi$$

$$1/2\langle\langle \hat{X}_1\hat{P}_1\rangle + \langle \hat{P}_1\hat{X}_1\rangle\rangle_\Phi = \langle(\hat{P}_1\hat{X}_1 + \hat{X}_1\hat{P}_1)\rangle\langle c_1^2\rangle_\Phi - 1/2\langle(\hat{P}_1\hat{X}_1 + \hat{X}_1\hat{P}_1)\rangle$$
$$- \langle \hat{X}_1^2\rangle\langle c_1 s_1\rangle_\Phi + \langle \hat{P}_1^2\rangle\langle c_1 s_1\rangle_\Phi$$

$$\langle \hat{X}_1\hat{X}_2\rangle_\Phi = \langle \hat{X}_1\hat{X}_2\rangle\langle c_1 c_2\rangle_\Phi + \langle \hat{P}_1\hat{X}_2\rangle\langle s_1 c_2\rangle_\Phi + \langle \hat{X}_1\hat{P}_2\rangle\langle c_1 s_2\rangle_\Phi$$
$$+ \langle \hat{P}_1\hat{P}_2\rangle\langle s_1 s_2\rangle_\Phi$$

$$\langle \hat{X}_1\hat{P}_2\rangle_\Phi = \langle \hat{X}_1\hat{P}_2\rangle\langle c_1 c_2\rangle_\Phi + \langle \hat{P}_1\hat{P}_2\rangle\langle s_1 c_2\rangle_\Phi - \langle \hat{X}_1\hat{X}_2\rangle\langle c_1 s_2\rangle_\Phi$$
$$- \langle \hat{P}_1\hat{X}_2\rangle\langle s_1 s_2\rangle_\Phi$$

$$\langle \hat{P}_1\hat{X}_2\rangle_\Phi = \langle \hat{P}_1\hat{X}_2\rangle\langle c_1 c_2\rangle_\Phi - \langle \hat{X}_1\hat{X}_2\rangle\langle s_1 c_2\rangle_\Phi + \langle \hat{P}_1\hat{P}_2\rangle\langle c_1 s_2\rangle_\Phi$$
$$- \langle \hat{X}_1\hat{P}_2\rangle\langle s_1 s_2\rangle_\Phi$$

$$\langle \hat{P}_1\hat{P}_2\rangle_\Phi = \langle \hat{P}_1\hat{P}_2\rangle\langle c_1 c_2\rangle_\Phi - \langle \hat{X}_1\hat{P}_2\rangle\langle s_1 c_2\rangle_\Phi - \langle \hat{P}_1\hat{X}_2\rangle\langle c_1 s_2\rangle_\Phi$$
$$+ \langle \hat{X}_1\hat{X}_2\rangle\langle s_1 s_2\rangle_\Phi$$

$$1/2\langle\langle \hat{X}_2\hat{P}_2\rangle + \langle \hat{P}_2\hat{X}_2\rangle\rangle_\Phi = \langle(\hat{P}_2\hat{X}_2 + \hat{X}_2\hat{P}_2)\rangle\langle c_2^2\rangle_\Phi - 1/2\langle(\hat{P}_2\hat{X}_2 + \hat{X}_2\hat{P}_2)\rangle$$
$$+ \hat{P}_2^2\langle c_2 s_2\rangle_\Phi - \langle \hat{X}_2^2\rangle\langle c_2 s_2\rangle_\Phi$$

These ten equations are depending on the eight dephasing parameters and the entries of the initial covariance matrix without dephasing.

APPENDIX B

Experimental supplement

B.1 Phase noise values

Tabular for the calculated phase noise parameters. In Chapter 5, the state is only classified by the parameter $q = \langle \cos \theta_A \cos \theta_B \rangle_\Phi$. This would be sufficient if the phase noise would have been truly symmetric and uncorrelated. However, due to experimental imperfections, the other parameters are not exactly zero or redundant and thus here listed for completeness. The values are experimentally obtained by the method described in Section 2.4.2. The values are given in dependence of the amplification stage of the noise before it is applied to the piezo driven transducer and are given for three fractional digits. The eight dephasing parameter are

$\textcircled{1}$ $\langle \cos^2 \theta_A \rangle_\Phi$ $\qquad$ $\textcircled{2}$ $\langle \cos \theta_A \sin \theta_A \rangle_\Phi$ $\quad$ $\textcircled{3}$ $\langle \cos^2 \theta_B \rangle_\Phi$

$\textcircled{4}$ $\langle \cos \theta_B \sin \theta_B \rangle_\Phi$ $\quad$ $\textcircled{5}$ $\langle \cos \theta_A \cos \theta_B \rangle_\Phi$ $\quad$ $\textcircled{6}$ $\langle \cos \theta_A \sin \theta_B \rangle_\Phi$

$\textcircled{7}$ $\langle \sin \theta_A \cos \theta_B \rangle_\Phi$ $\quad$ $\textcircled{8}$ $\langle \sin \theta_A \sin \theta_B \rangle_\Phi$

	①	②	③	④	⑤	⑥	⑦	⑧
0.3	1.003	0.006	1.007	0.000	1.005	0.001	0.006	0.006
0.6	1.010	0.001	1.006	-0.008	1.007	-0.005	0.005	0.011
1.0	0.994	0.011	0.990	-0.003	0.990	-0.008	0.008	0.001
1.3	1.003	-0.004	1.002	-0.006	1.000	-0.003	-0.001	0.018
1.6	0.996	-0.008	0.973	-0.010	0.982	-0.009	-0.003	0.011
2.0	0.973	0.000	0.952	-0.006	0.956	-0.008	0.003	0.002
2.3	0.971	-0.006	0.949	-0.006	0.952	-0.006	-0.002	0.012
2.6	0.952	-0.012	0.931	-0.009	0.930	-0.007	-0.006	0.008
3.0	0.943	0.006	0.906	-0.001	0.908	-0.015	0.004	0.010
3.3	0.928	-0.003	0.899	-0.007	0.888	-0.014	-0.000	0.012
3.6	0.920	-0.004	0.870	0.000	0.868	-0.015	-0.003	0.014
4.0	0.896	-0.020	0.839	-0.012	0.833	-0.012	-0.008	0.012
4.3	0.887	-0.021	0.827	-0.013	0.816	-0.011	-0.005	0.021
4.6	0.875	-0.005	0.808	0.002	0.791	-0.018	-0.001	0.023
5.0	0.848	-0.018	0.777	-0.005	0.751	-0.014	-0.005	0.021
5.3	0.841	-0.036	0.761	-0.019	0.730	-0.011	-0.008	0.030
5.6	0.818	-0.030	0.737	-0.012	0.693	-0.013	-0.007	0.023
6.0	0.803	-0.003	0.714	0.020	0.656	-0.014	-0.002	0.025
6.3	0.790	-0.032	0.696	-0.008	0.630	-0.012	-0.005	0.031
6.6	0.768	-0.021	0.677	0.008	0.592	-0.013	-0.006	0.022
7.0	0.749	-0.013	0.656	0.011	0.549	-0.014	-0.004	0.021
8.0	0.714	-0.016	0.613	0.003	0.452	-0.012	-0.003	0.027
9.0	0.678	-0.006	0.580	-0.009	0.354	-0.015	0.001	0.021
10.0	0.655	-0.063	0.548	-0.080	0.270	-0.009	-0.001	0.020
5.5	0.858	0.126	0.935	0.147	0.789	-0.002	0.006	0.009

Table B.1: Dephasing parameters for dephased states. The values are given for the setting of the linear amplifier, which amplifies the noise signal given by the computer soundfile. Parameter ⑤ corresponds to the dephasing parameter q, given in the section. The large block in the top corresponds to the measurements with 10^7 data points. The last line corresponds to the measurement on the large data set with $5 \cdot 10^8$ data points.

	η_A	η_B
0.3	0.994	0.998
0.6	0.999	0.992
1.0	0.992	0.994
1.3	0.985	0.984
1.6	0.984	0.980
2.0	0.994	0.994
2.3	0.988	0.988
2.6	0.989	0.994
3.0	0.984	0.986
3.3	0.987	0.989
3.6	0.983	0.983
4.0	0.981	0.988
4.3	0.972	0.984
4.6	0.974	0.980
5.0	0.977	0.986
5.3	0.965	0.978
5.6	0.968	0.982
6.0	0.963	0.971
6.3	0.961	0.975
6.6	0.969	0.978
7.0	0.967	0.977
8.0	0.956	0.973
9.0	0.952	0.965
10.0	0.952	0.964

Table B.2: Efficiencies of the lossy channel that occurred during the phase noise implementation

B.2 Bootstrapping

For the results, a covariance matrix is reconstructed from the whole data set and the properties of gaussian purity P_G, entanglement witness μ and squeezing V_{sq} are calculated. To obtain information about the statistical errors of this properties, the *bootstrap* method can be applied. From the original data set of length N, here consisting of the N quadrature value quadruples (X_A, P_A, X_B, P_B), m new data sets are obtained by random sampling with replacement from the original data set. For each of this m bootstrapping data sets, the entanglement value, etc. is calculated, giving a distribution of m values around the value calculated from the original data set. The standard deviation σ of this distribution is used to give the 2σ confidence interval for the distillation results of the measurement with $5 \cdot 10^8$ data points.
For all figures with error bars, this method was applied with $m = 100$.

APPENDIX C

Material

In addition to the programs that are already mentioned in the main text, the following programs were used:

Mode matchings for the optical setup were calculated with the program *JamMT* from Nico Lastzka.

All plots are generated with *Gnuplot*. Schematic setups and all other figures are created with *Illustrator CS5-CC*. The pictograms for these figures are taken from the *Component library*, originally designed by Alexander Franzen and here presented in an updated version provided by Jan Gniesmer.

The emulated distillation protocol was performed using a MatLab script, written together with Jaromír Fiurášek.

The data for the probability distribution of the phase-diffused squeezed state in Fig. 2.5 was simulated with a Python 2.7 script from Christoph Baune.

This thesis is written with LaTeX using the MiKTeX distribution and the editor *TeXstudio*.

Bibliography

[1] A. Einstein, B. Podolsky, and N. Rosen. Can quantum-mechanical description of physical reality be considered complete? *Physical Review*, 47(10):777–780, 1935.

[2] E. Schrödinger. Discussion of Probability Relations between Separated Systems. *Mathematical Proceedings of the Cambridge Philosophical Society*, 31(04):555–563, 1935.

[3] J. S. Bell. On the Einstein Podolsky Rosen paradox. *Physics*, 1(3), 1964.

[4] A. Aspect, P. Grangier, and G. Roger. Experimental Tests of Realistic Local Theories via Bell's Theorem. *Physical Review Letters*, 47(7):460–463, 1981.

[5] S. Steinlechner, J. Bauchrowitz, M. Meinders, H. Müller-Ebhardt, K. Danzmann, and R. Schnabel. Quantum-dense metrology. *Nature Photonics*, 7(8):626–630, 2013.

[6] H J Kimble. The quantum internet. *Nature*, 453(7198):1023–1030, 2008.

[7] C. Weedbrook, S. Pirandola, R. García-Patrón, N. J. Cerf, T. C. Ralph, J. H. Shapiro, and S. Lloyd. Gaussian quantum information. *Reviews of Modern Physics*, 84:621–669, 2012.

[8] A. K. Ekert. Quantum cryptography based on Bell's theorem. *Physical Review Letters*, 67:661–663, 1991.

[9] V. Scarani, H. Bechmann-Pasquinucci, N. J. Cerf, M. Dušek, N. Lütkenhaus, and M. Peev. The security of practical quantum key distribution. *Reviews of Modern Physics*, 81(3):1301–1350, 2009.

[10] D. Bouwmeester, J. M. Pan, K. Mattle, M. Eibl, H. Weinfurter, and A. Zeilinger. Experimental quantum teleportation. *Nature*, 390:575–579, 1997.

[11] A. Furusawa, J. L. Sørensen, S. L. Braunstein, C. A. Fuchs, H. J. Kimble, and E. S. Polzik. Unconditional quantum teleportation. 282:706–709, 1998.

[12] W. P. Bowen, R. Schnabel, P. K. Lam, and T. C. Ralph. Experimental Investigation of Criteria for Continuous Variable Entanglement. *Physical Review Letters*, 90(4):043601, 2003.

[13] C. H. Bennett and G. Brassard. Quantum cryptography: Public key distribution and coin tossing. *Proceedings of IEEE International Conference on Computers*, 175:7–11, 1984.

[14] F. Grosshans and P. Grangier. Continuous Variable Quantum Cryptography Using Coherent States. *Physical Review Letters*, 88(5):57902, 2002.

[15] R. Ursin, F. Tiefenbacher, T. Schmitt-Manderbach, H. Weier, T. Scheidl, M. Lindenthal, B. Blauensteiner, T. Jennewein, J. Perdigues, P. Trojek, B. Omer, M. Furst, M. Meyenburg, J. Rarity, Z. Sodnik, C. Barbieri, H. Weinfurter, and A. Zeilinger. Entanglement-based quantum communication over 144 km. *Nature Physics*, 3(7):481–486, 2007.

[16] G. He, J. Zhu, and G. Zeng. Quantum secure communication using continuous variable Einstein-Podolsky-Rosen correlations. *Physical Review A*, 73(1):12314, 2006.

[17] C. Rodó, O. Romero-Isart, K. Eckert, and A. Sanpera. Efficiency in Quantum Key Distribution Protocols with Entangled Gaussian States. *Open Systems & Information Dynamics*, 14(01):69–80, 2007.

[18] X. Su, W. Wang, Y. Wang, X. Jia, C. Xie, and K. Peng. Continuous variable quantum key distribution based on optical entangled states without signal modulation. *Europhysics Letters*, 87(2):20005, 2009.

[19] M. Aspelmeyer, H. R. Böhm, T. Gyatso, T. Jennewein, R. Kaltenbaek, M. Lindenthal, G. Molina-Terriza, A. Poppe, K. Resch, M. Taraba, R. Ursin, P. Walther, and A. Zeilinger. Long-Distance Free-Space Distribution of Quantum Entanglement. *Science*, 301(5633):621–623, 2003.

[20] J. Yin, Y. Cao, Y. Li, S. Liao, L. Zhang, J. Ren, W. Cai, W. Liu, B. Li, H. Dai, G. Li, Q. Lu, Y. Gong, Y. Xu, S. Li, F. Li, Y. Yin, Z. Jiang, M. Li, J. Jia, G. Ren, D. He, Y. Zhou, X. Zhang, N. Wang, X. Chang, Z. Zhu, N. Liu, Y. Chen, C. Lu, R. Shu, C. Peng, J. Wang, and J. Pan. Satellite-based entanglement distribution over 1200 kilometers. *Science*, 356(6343):1140–1144, 2017.

[21] T. Inagaki, N. Matsuda, O. Tadanaga, M. Asobe, and H. Takesue. Entanglement distribution over 300 km of fiber. *Optics Express*, 21(20):23241–23249, 2013.

[22] D. Aktas, B. Fedrici, F. Kaiser, T. Lunghi, L. Labonté, and S. Tanzilli. Entanglement distribution over 150 km in wavelength division multiplexed channels for quantum cryptography. *Laser & Photonics Reviews*, 10(3):451–457, 2016.

[23] C. H. Bennett, G. Brassard, S. Popescu, B. Schumacher, J. A. Smolin, and W. K. Wootters. Purification of noisy entanglement and faithful teleportation via noisy channels. *Physical Review Letters*, 76:722–725, 1996.

[24] D. Deutsch, A. Ekert, R. Jozsa, C. Macchiavello, S. Popescu, and A. Sanpera. Quantum privacy amplification and the security of quantum cryptography over noisy channels. *Physical Review Letters*, 77:2818–2821, 1996.

[25] C. H. Bennett, D. P. DiVincenzo, J. A. Smolin, and W. K. Wootters. Mixed-state entanglement and quantum error correction. *Physical Review A*, 54(1):1–82, 1996.

[26] P. G. Kwiat, S. Barraza-Lopez, A. Stefanov, and N. Gisin. Experimental entanglement distillation and 'hidden' non-locality. *Nature*, 409(6823):1014–1017, 2001.

[27] J. Pan, S. Gasparoni, R. Ursin, G. Weihs, and A. Zeilinger. Experimental entanglement purification of arbitrary unknown states. *Nature*, 423(6938):417–422, 2003.

[28] B. Hage, A. Samblowski, J. DiGuglielmo, A. Franzen, J. Fiurášek, and R. Schnabel. Preparation of distilled and purified continuous-variable entangled states. *Nature Physics*, 4(12):915–918, 2008.

[29] R. Dong, M. Lassen, J. Heersink, C. Marquardt, R. Filip, G. Leuchs, and U. L. Andersen. Experimental entanglement distillation of mesoscopic quantum states. *Nature Physics*, 4(12):919–923, 2008.

[30] H. Takahashi, J. S. Neergaard-Nielsen, M. Takeuchi, M. Takeoka, K. Hayasaka, A. Furusawa, and M. Sasaki. Entanglement distillation from Gaussian input states. *Nature Photonics*, 4(3):178–181, 2010.

[31] Y. Kurochkin, A. S. Prasad, and A. I. Lvovsky. Distillation of The Two-Mode Squeezed State. *Physical Review Letters*, 112(7):70402, 2014.

[32] D. E. Browne, J. Eisert, S. Scheel, and M. B. Plenio. Driving non-gaussian to gaussian states with linear optics. *Physical Review A*, 67:062320, 2003.

[33] B. Hage, A. Samblowski, J. Diguglielmo, J. Fiurášek, and R. Schnabel. Iterative entanglement distillation: Approaching the elimination of decoherence. *Physical Review Letters*, 105:1–4, 2010.

[34] C. Simon, M. Afzelius, J. Appel, A. Boyer De La Giroday, S. J. Dewhurst, N. Gisin, C. Y. Hu, F. Jelezko, S. Kröll, J. H. Müller, J. Nunn, E. S. Polzik, J. G. Rarity, H. De Riedmatten, W. Rosenfeld, A. J. Shields, N. Sköld, R. M. Stevenson, R. Thew, I. A. Walmsley, M. C. Weber, H. Weinfurter, J. Wrachtrup, and R. J. Young. Quantum memories. *European Physical Journal D*, 58(1):1–22, 2010.

[35] E. T. Campbell, M. G. Genoni, and J. Eisert. Continuous-variable entanglement distillation and noncommutative central limit theorems. *Physical Review A*, 87(4):42330, 2013.

[36] A. Datta, L. Zhang, J. Nunn, N. K. Langford, A. Feito, M. B. Plenio, and I. A. Walmsley. Compact continuous-variable entanglement distillation. *Physical Review Letters*, 108, 2012.

[37] J. Fiurášek and N. J. Cerf. Gaussian post-selection and virtual noiseless amplification in continuous-variable quantum key distribution. *Physical Review A*, 86:1–5, 2012.

[38] N. Walk, T. C. Ralph, T. Symul, and P. K. Lam. Security of continuous-variable quantum cryptography with Gaussian postselection. *Physical Review A*, 87(2):20303, 2013.

[39] T. C. Ralph and A. P. Lund. Nondeterministic Noiseless Linear Amplification of Quantum Systems. *AIP Conference Proceedings*, 1110(1):155–160, 2009.

[40] P. Marek and R. Filip. Coherent-state phase concentration by quantum probabilistic amplification. *Physical Review A*, 81(2):22302, 2010.

[41] J. Fiurášek. Engineering quantum operations on traveling light beams by multiple photon addition and subtraction. *Physical Review A*, 80(5):53822, 2009.

[42] H. M. Chrzanowski, N. Walk, S. M. Assad, J. Janousek, S. Hosseini, T. C. Ralph, T. Symul, and P. K. Lam. Measurement-based noiseless linear amplification for quantum communication. *Nature Photonics*, 8:333–338, 2014.

[43] G. Giedke and J. I. Cirac. Characterization of gaussian operations and distillation of gaussian states. *Physical Review A*, 66, 2002.

[44] J. Fiurášek. Gaussian transformations and distillation of entangled Gaussian states. *Physical Review Letters*, 89(1):137904, 2002.

[45] J. Eisert, S. Scheel, and M. B. Plenio. Distilling Gaussian States with Gaussian Operations is Impossible. *Physical Review Letters*, 1:2–5, 2002.

[46] D. Abdelkhalek, M. Syllwasschy, N. J. Cerf, J. Fiurášek, and R. Schnabel. Efficient entanglement distillation without quantum memory. *Nature Communications*, 7, 2016.

[47] J. Eisert, D. E. Browne, S. Scheel, and M. B. Plenio. Distillation of continuous-variable entanglement with optical means. *Annals of Physics*, 311:431–458, 2004.

[48] G. Y. Xiang, T. C. Ralph, a. P. Lund, N. Walk, and G. J. Pryde. Heralded noiseless linear amplification and distillation of entanglement. *Nature Photonics*, 4(5):316–319, 2010.

[49] M.A. Nielsen and I.L. Chuang. *Quantum Computation and Quantum Information*. Cambridge University Press, Cambridge, 2010.

[50] W. Heisenberg. Über den anschaulichen Inhalt der quantentheoretischen Kinematik und Mechanik. *Zeitschrift für Physik*, 43:172–198, 1927.

[51] H. P. Robertson. The uncertainty principle. *Physical Review*, 34:163–164, 1929.

[52] C. C. Gerry and P. L. Knight. *Introductory Quantum Optics*. Cambridge University Press, 2005.

[53] S. L. Braunstein and P. Van Loock. Quantum information with continuous variables. *Reviews of Modern Physics*, 77(513), 2005.

[54] U. Leonhardt. *Measuring the Quantum State of Light*. Cambridge University Press, 2005.

[55] S. M. Barnett and P. M. Radmore. *Methods in Theoretical Quantum Optics*. Oxford Series in Optical and Imaging Sciences. Clarendon Press, 2002.

[56] R. J. Glauber. Coherent and incoherent states of the radiation field. *Physical Review*, 1963.

[57] J. Williamson. On the Algebraic Problem Concerning the Normal Forms of Linear Dynamical Systems. *American Journal of Mathematics*, 58(1):141–163, 1936.

[58] R. F. Werner. Quantum states with Einstein-Podolsky-Rosen correlations admitting a hidden-variable model. *Physical Review A*, 40(8):4277–4281, 1989.

[59] J. DiGuglielmo, B. Hage, A. Franzen, J. Fiurášek, and R. Schnabel. Experimental characterization of gaussian quantum-communication channels. *Physical Review A*, 76:012323, 2007.

[60] R. Schnabel. Squeezed states of light and their applications in laser interferometers. *Physics Reports*, 684:1 – 51, 2017.

[61] R. Simon. Peres-Horodecki Separability Criterion for Continuous Variable Systems. *Physical Review Letters*, 84:2726, 2000.

[62] A. Peres. Separability Criterion for Density Matrices. *Physical Review Letters*, 77(8):1413–1415, 1996.

[63] P. Horodecki. Separability criterion and inseparable mixed states with positive partial transposition. *Physics Letters A*, 232(5):333 – 339, 1997.

[64] J. Fiurášek. Private communication.

[65] A. Franzen, B. Hage, J. Diguglielmo, J. Fiurásek, and R. Schnabel. Experimental demonstration of continuous variable purification of squeezed states. *Physical Review Letters*, 97, 2006.

[66] B. Hage. *Purification and Distillation of Continuous Variable Entanglement*. Ph.d. thesis, Leibniz Universität Hannover, 2010.

[67] A Franzen. *Präparation von destillierten und purifizierten gequetschten Zuständen*. Ph.d. thesis, Leibniz Universität Hannover, 2008.

[68] S. Steinlechner. *Quantum metrology with squeezed and entangled light for the detection of gravitational waves*. PhD thesis, Leibniz Universität Hannover, 2013.

[69] C. K. Hong and L. Mandel. Experimental realization of a localized one-photon state. *Physical Review Letters*, 56(1):58–60, 1986.

[70] A. I. Lvovsky, H. Hansen, T. Aichele, O. Benson, J. Mlynek, and S. Schiller. Quantum State Reconstruction of the Single-Photon Fock State. *Physical Review Letters*, 87(5), 2001.

[71] J. Fiurášek, P. Marek, R. Filip, and R. Schnabel. Experimentally feasible purification of continuous-variable entanglement. *Physical Review A*, 75(5), 2007.

[72] A. E. Ulanov, I. A. Fedorov, A. Pushkina, Y. V. Kurochkin, T. C. Ralph, and A. I. Lvovsky. Undoing the effect of loss on quantum entanglement. *Nature Photonics*, 9(11):764–768, 2015.

[73] J. Eisert, M. B. Plenio, D. E. Browne, S. Scheel, and A. Feito. On the experimental feasibility of continuous-variable optical entanglement distillation. *Optics and Spectroscopy*, 103(2):173–177, 2007.

[74] J. Fiurášek. Distillation and purification of symmetric entangled Gaussian states. *Physical Review A*, 82, 2010.

[75] P. Marek, J. Fiurášek, B. Hage, A. Franzen, J. Digugliemo, and R. Schnabel. Multiple-copy distillation and purification of phase-diffused squeezed states. *Physical Review A*, 76, 2007.

[76] E. T. Campbell and J. Eisert. Gaussification and entanglement distillation of continuous-variable systems: A unifying picture. *Physical Review Letters*, 108, 2012.

[77] E. D. Black. An introduction to Pound-Drever-Hall laser frequency stabilization. *American Journal of Physics*, 69(1):79, 2001.

[78] A. Samblowski. *State Preparation for Quantum Information Science and Metrology*. Ph.d. thesis, Leibniz Universität Hannover, 2012.

[79] Y. Zhang, Z. Li, S. Yu, W. Gu, X. Peng, and H. Guo. Continuous-variable measurement-device-independent quantum key distribution using squeezed states. *Physical Review A*, 90(5), 2014.

[80] S. Pirandola, C. Ottaviani, G. Spedalieri, C. Weedbrook, S. L. Braunstein, S. Lloyd, T. Gehring, C. S. Jacobsen, and U. L. Andersen. High-rate measurement-device-independent quantum cryptography. *Nature Photonics*, 9(6):397–402, 2015.

[81] C. Weedbrook, A. M. Lance, W. P. Bowen, T. Symul, T. C. Ralph, and P. K. Lam. Quantum Cryptography Without Switching. *Physical Review Letters*, 93(17), 2004.

[82] C. Baune, A. Schönbeck, A. Samblowski, J. Fiurášek, and R. Schnabel. Quantum non-Gaussianity of frequency up-converted single photons. *Optics Express*, 22(19):22808–22816, 2014.

[83] H. Vahlbruch, M. Mehmet, K. Danzmann, and R. Schnabel. Detection of 15 dB Squeezed States of Light and their Application for the Absolute Calibration of Photoelectric Quantum Efficiency. *Physical Review Letters*, 110801:1–5, 2016.

[84] Y. Takeno, M. Yukawa, H. Yonezawa, and A. Furusawa. Observation of -9 dB quadrature squeezing with improvement of phase stability in homodyne measurement. *Optics Express*, 15(7):4321–7, 2007.

[85] S. Ast, M. Ast, M. Mehmet, and R. Schnabel. Gaussian entanglement distribution with gigahertz bandwidth. *Optics Letters*, 41(21):5094–5097, 2016.

[86] Stefan Ast. *New approaches in squeezed light generation*. Phd. thesis, Leibniz Universität Hannover, 2015.

[87] Christoph Baune. *Frequency up-conversion of nonclassical states of light*. Ph.d. thesis, Leibniz Universität Hannover, 2016.

[88] K. Wakui, H. Takahashi, A. Furusawa, and M. Sasaki. Photon subtracted squeezed states generated with periodically poled KTiOPO_4. *Optics Express*, 15(6), 2007.

List of publications

[1] C. E. Vollmer, D. Schulze, T. Eberle, V. Händchen, J. Fiurášek, and R. Schnabel, "Experimental Entanglement Distribution by Separable States", Physical Review Letters, Vol. 111, 2013.

[2] D. Abdelkhalek, M. Syllwasschy, N. J. Cerf, J. Fiurášek, and R. Schnabel, "Efficient entanglement distillation without quantum memory", Nature Communications, Vol. 7, 2016.

Acknowledgements

I would like to thank all the people, that helped me in one or the other way to finish this thesis.

To start with, I want to thank my supervisor Roman Schnabel. Thank you for the possibility to be part of this working group for quite some time now. I could always rely on your help and support, especially when experiments are not working the way they should.

Many thanks to Prof. Karsten Danzmann for the admittance to finish my PhD in the AEI in Hannover, although our working group already moved to Hamburg a year ago. The AEI was an inspiring place to work at and I still feel as a part of it.

I owe large gratitude to Prof. Jaromír Fiurášek whose theoretical support facilitated my projects in the first place. I am very grateful for his never-ending patience to my various questions and his capability to explain the theoretical concepts in a language that an experimentalist can understand easily.

I like to thank all the people that joined me on my way to the results of this thesis. Namely Mareike Syllwasschy, who worked with me on the distillation of non-Gaussian states during her master thesis. Lorena Rebón, who joined me in the beginning of the second experiment and who helped with the move of the experiment to Hamburg, and Julian Göttsch with whom I performed the measurements for the second experiment within his master thesis.

I want to thank all people of my working group. It is a good feeling to know that one can always ask the colleagues in the neighboring laboratory or office if one struggles with a problem or just needs a break in nice company. Many of you became friends to me and I loved not only the lunch breaks but also the nice evenings apart from work. Special thanks to Jan Gniesmer for being the best office mate I could possibly ever have.

Let me also thank all people who supported me while I wrote this thesis. Thanks for proof-reading to Kais Abdelkhalek, Jan Gniesmer, Carolin Höld, Amrit Pal Singh, Paolo Piergentili, Axel Schönbeck, Sebastian Steinlechner and Jascha Zander.

Vielen Dank an meine Familie dafür, dass ihr für mich da ward oder mir meine Ruhe gegeben habt, je nachdem was ich gerade brauchte. Und Danke, Kais, mein wundervoller Mann, dafür, dass du so bist wie du bist und ich mich einfach immer auf dich verlassen kann!

Curriculum Vitae

Personal information

Full Name:	Daniela Abdelkhalek, née Schulze
Date of Birth:	10.07.1988
Place of Birth:	31275 Lehrte
Citizenship:	German

Education

2013–2017	Doctoral studies in Physics, Leibniz Universität Hannover
2012	Master thesis at the Institute for Gravitational Physics
	Supervisor: Prof. Dr. Roman Schnabel
	Title: Verteilung von Verschränkung mit separablen Zuständen
2010–2012	Master studies in Physics, Leibniz Universität Hannover
2010	Bachelor thesis at the Institute for Gravitational Physics
	Supervisor: Prof. Dr. Roman Schnabel
	Title: Bestimmung der Quanteneffizienz von Photodioden mit gequetschtem Licht
2007–2010	Bachelor studies in Physics, Leibniz Universität Hannover
2000–2007	Abitur at Gymnasium Lehrte